2018

MORPHOLOGY AND MIXING STATE OF SOOT AND TAR BALLS: IMPLICATIONS FOR OPTICAL PROPERTIES AND CLIMATE

Janarjan Bhandari
Michigan Technological University, jbhandar@mtu.edu

MORPHOLOGY AND MIXING STATE OF SOOT AND TAR BALLS: IMPLICATIONS FOR OPTICAL PROPERTIES AND CLIMATE

By

Janarjan Bhandari

A DISSERTATION

Submitted in partial fulfillment of the requirements for the degree of

DOCTOR OF PHILOSOPHY

In Atmospheric Sciences

MICHIGAN TECHNOLOGICAL UNIVERSITY

2018

This dissertation has been approved in partial fulfillment of the requirements for the Degree of DOCTOR OF PHILOSOPHY in Atmospheric Sciences.

Department of Physics

Dissertation Advisor:	*Dr. Claudio Mazzoleni*
Committee Member:	*Dr. Jacek Borysow*
Committee Member:	*Dr. Will Cantrell*
Committee Member:	*Dr. Paul Doskey*
Department Chair:	*Dr. Ravindra Pandey*

Table of Contents

Preface

Chapter 2 presented in this dissertation is unpublished work in progress and the manuscript for chapter 4 was submitted to a journal and the reviewers have recommended for the publication of the manuscript after a minor revision.

Chapter 2 is based on a study of cloud-processed soot samples collected during field and laboratory experiments. I conducted the laboratory experiments in collaboration with my co-authors at Michigan Technological University. I carried out SEM/TEM analyses of samples collected during these studies. I wrote the manuscript with the help of my advisor Dr. Claudio Mazzoleni with contributions and edits from all co-authors. The manuscript is expected to be submitted in the '*Journal of Geophysical Research: Atmospheres*' by fall of 2018.

Chapter 3 was published in the journal '*Atmosphere*' (Bhandari et al., 2017) and is republished entirety as a chapter in this dissertation. I performed the SEM analysis with the help of Dr. Swarup China. I, Dr. Claudio Mazzoleni and Dr. Swarup China wrote most of the paper with significant contributions and edits from all the coauthors.

Chapter 4 is related to the study of the optical properties of tar ball aggregates. I carried out numerical simulations and wrote the manuscript with significant inputs from my advisor, Dr. Claudio Mazzoleni and the other co-authors. After a peer-review by the anonymous reviewers, the manuscript has been recommended for publication in the '*Journal of Quantitative Spectroscopy and Radiative Transfer*' with a minor revision.

Chapter 2 will be further revised based on suggestions and comments from the co-authors and chapter 4 will be revised based on the comments from the reviewers.

Acknowledgements

First and foremost, I would like to express my sincere gratitude to my advisor Dr. Claudio Mazzoleni for his guidance, patience, and intellectual support throughout my Ph.D. research. I feel very fortunate to get a chance to work with him who offered invaluable research advices and always provided me opportunities to participate in collaborative research projects and conferences that allowed me to grow academically and intellectually.

I would like to thank Dr. Jacek Borysow, Dr. Will Cantrell and Dr. Paul Doskey for serving on my Ph.D. dissertation committee and for their valuable inputs toward my research. I am very thankful to the Atmospheric Sciences Program for the Outstanding Scholarship Award and equally thankful to the Physics Department for all the support during my Ph.D. I also thank the Elizabeth and Richard Henes Center for Quantum Phenomena for providing support to the conferences and I am grateful to the Graduate School for the Doctoral Finishing Fellowship that supported me while I worked on my dissertation and defense.

I am grateful to my senior colleagues Dr. Swarup China and Dr. Noopur Sharma for their motivation and co-operation in the early days of my research. I thank Kyle Gorkowski and Tyler Capek for their constructive feedback and valuable advices when needed. I am thankful to all the present and past members of our group; Kendra Wright, Sumit Kumar, Nicole Niedermeier, Denis van der Voort, Kaelan Anderson, Giulia Girotto, Renato Pinto Reveggino, Novia Berriel, Keegan Downham and Illiya Chibirev for the useful group discussion. I am thankful to my officemate Kamal Kant Chandrakar and Subin Thomas for the useful discussion and insightful comments, which helped me to gather knowledge outside my area of expertise.

I am thankful to the collaborators at Boston College, Dr. Paul Davidovits, Dr. Tim Onasch and Dr. Leonid Nichman for allowing me to participate earlier in the BC5 campaign. Thank you for the insightful discussion and all the care that I got during the campaign. I am thankful to the collaborators at the Las Alamos National Laboratory Dr. Manvendra Dubey and Dr. Allison Aiken for the valuable discussion on my research.

I am forever grateful to my mother, Ms. Bhagawati Bhandri and my brother, Rameshwor Bhandari and all the extended family members and relatives for their support during my Ph.D. Last but not the least, I am thankful to my dear wife, Subheksha Baral, for her endurance, strong support and encouragement at all times.

List of abbreviations

AMS aerosol mass spectrometer

AR aspect ratio

A_p projected area of image

b backscatter fraction

BC2 Boston College Experiment 2

BC4 Boston College Experiment 4

BCCA ballistic cluster-cluster aggregation

BrC brown carbon

CCN cloud condensation nuclei

CDNC cloud droplet number concentration

CPMA centrifugal particle mass analyzer

D_{Aeq} area equivalent diameter

DDA dipole-dipole approximation

DMA differential mobility analyzer

DRF direct radiative forcing

D_F fractal dimension

D_{3F} 3-D fractal dimension

d_m mobility diameter

EC elemental carbon

EDS energy dispersive X-ray spectroscopy

E_{abs} absorption enhancement

E_{sca} scattering enhancement

FE-SEM field emission scanning electron microscopy

g	asymmetry parameter
IN	ice nuclei
IS	interstitial soot
JaSTA	Java Superposition T-Matrix App
LWC	liquid water content
L_{max}	maximum length of projected image
LWC_f	final liquid water content
LWC_i	initial liquid water content
MAE	mass absorption efficiency
MSE	mass scattering efficiency
OC	organic carbon
OCEC	organic carbon and elemental carbon
PAM	potential aerosol mass
PCVI	pumped counterflow virtual impactor
PM	particulate matter
PM1	particulate matter with diameter less than 1 μm
PM2.5	particulate matter with diameter less than 2.5 μm
PM10	particulate matter with diameter less than 10 μm
RDG	Rayleigh-Debye-Gans
RH	relative humidity
RS	residual soot
SEM	scanning electron microscopy
SFE	simple forcing efficiency
SMPS	scanning mobility particle sizer

SOA	secondary organic aerosol
SPC	San Pietro Capofiume
SSA	single scattering albedo
S_0	extraterrestrial solar constant
TB	tar ball
TD	thermodenuder
TEM	transmission electron microscopy
TOA	top of the atmosphere
UFP	ultra-fine particle
UV	ultra violet
VER	volume equivalent radius
W	width of projected image
β	hemispherical upscatter fraction
τ	aerosol optical depth
ΔF	change in direct radiative forcing

Abstract

Soot particles form during incomplete combustion of carbonaceous materials. These particles strongly absorb light and directly affect Earth's climate by warming our atmosphere. When freshly emitted, soot particles have a fractal-like morphology consisting of aggregates of carbon spherules. During atmospheric processing, soot aggregates interact with other materials present in our atmosphere (i.e., other aerosol or condensable vapors) and these interactions can result in the formation of coated, mixed or compacted soot particles with different morphologies. Any process that alters the morphology (shape, size and internal structure) and mixing state of soot also affects its optical properties, which in turn affect the soot radiative forcing in the atmosphere. The complex morphology and internal mixing state of soot makes it difficult to estimate the soot's radiative properties. A detailed investigation of soot at the single particle level using electron microscopy, thus, becomes essential to provide accurate information for climate models, which generally assumes simple spherical morphologies.

Tar balls are another type of carbonaceous aerosol, in the brown carbon family, commonly formed during smoldering combustion of biomass materials. Like soot, tar balls can also form aggregates. Tar balls aggregates have different optical properties from those of individual tar balls.

During my doctorate studies, I made extensive use of electron microscopy and image analysis tools to investigate the morphology and mixing state of soot and tar balls collected during different laboratory and field studies. In one of my research projects, I explored the morphology of cloud processed soot. For this, I investigated the morphology of soot particles collected from the Po Valley in Italy where fog often forms, especially in winter. Our investigation showed that soot particles became compacted after fog processing. The compaction of soot was further corroborated by a laboratory study, in which cloud processing was carried out within the Michigan Technological University cloud chamber.

In another research project, I studied the effects of thermodenuding on the morphology of soot. I investigated the morphology of five sets of soot samples of different sizes before

and after themodenuding. Our investigation showed no significant change in the morphology of soot by thermodenuding, a result that is important for those who attempt to measure the optical properties of internally mixed coated particles.

In a third study, I used T-Matrix and Lorenz-Mie models to calculate the optical properties and then estimate the radiative forcing of tar ball aggregates and individual tar balls. In fact, in a recent publication, we reported a significant fraction of tar ball aggregates from different locations on Earth. My numerical calculations showed that the optical properties of tar ball aggregates are different from those of individual tar balls and are not always well approximated by Lorentz-Mie calculations. These findings highlight the necessity to account for the aggregation of tar balls in global models.

My doctorate research provides detailed information on the morphology and mixing state of soot and tar ball aggregates. This information can be used to improve global climate models and reduce uncertainties in the radiative forcing of these aerosol particles.

1 Chapter 1: Introduction

Aerosol are solid or liquid particles suspended in the atmosphere with sizes ranging from a few nanometers to several microns. These aerosol are produced from natural and anthropogenic sources and their emissions in the atmosphere affect air quality, visibility, atmospheric radiation (by absorbing and scattering solar and terrestrial radiation), heterogeneous chemical reactions, and cloud properties, like the cloud formation, cloud lifetime, precipitation and cloud radiative properties (Haywood and Boucher, 2000;Hallquist et al., 2009;Reid and Sayer, 2003;Ackerman et al., 2000). Some aerosol dominantly scatter sunlight and cool our atmosphere, while a few of them absorb sunlight warming our atmosphere. Absorbing carbonaceous aerosol (black carbon and brown carbon) are abundant in Earth's atmosphere. Black carbon (also referred to as, soot) shows strong absorption in the visible region of the solar spectrum (Bond and Bergstrom, 2006), while the absorption by brown carbon is weak at long wavelengths but becomes important at short wavelengths (UV-blue region) (Saleh et al., 2015;Andreae and Gelencsér, 2006). The morphology, mixing state and elemental composition of individual carbonaceous particles affect their optical properties (e.g., light absorption and scattering), which in turn affect their radiative forcing. The use of electron microscopy and energy dispersive X-ray spectroscopy (EDS) provides an opportunity to study the morphology and the elemental composition of aerosol at a single particle level. In this dissertation, I present a comprehensive electron microscopy analysis of many individual carbonaceous atmospheric particles collected from laboratory and field campaigns to investigate their morphology and its implications on optical properties and radiative forcing.

1.1 Background and Motivation

Different kinds of particulate matter (PM), for example, carbonaceous aerosol, mineral dust, biological materials, metals, sulfates, nitrates etc. are released in the atmosphere from natural and anthropogenic sources. In addition to the directly emitted aerosol, volatile organic compounds emitted from plants and other sources can undergo gas-

particle phase conversion and form secondary organic aerosol (Hallquist et al., 2009). These aerosol from primary and secondary sources are of different morphology (shape, size and structure). The morphology of aerosol has a large degree of variability, such as spherical (e.g., tar balls), chainlike structure (e.g., soot), regular geometric shape (e.g., salt crystals), fiber-like (e.g., carbon nanotube), and irregular (mineral dust). Aerosol remain in atmosphere for only a few days, in contrast to some of the human-made greenhouse gases, such as CO2; so, the impact of aerosol pollution mitigation can achieve better air quality and human health benefits and reduce climatic impacts on a shorter time-scale than reducing greenhouse gases emissions (Jacobson, 2001; Ramanathan and Carmichael, 2008). However, there is a large uncertainty in estimating the global loading and optical properties of aerosol (Bond et al., 2013). The complexity of the morphology and mixing state of aerosol, like soot, is one of the prime causes of these uncertainties, which in turn, introduces uncertainties in the estimation of the aerosol radiative forcing. To reduce the uncertainties, it is necessary to characterize the morphology and mixing state of aerosol particles at a single particle level, for which electron microscopy is critical.

In this dissertation, I will mainly focus on the morphology and mixing state of soot and tar balls (TBs). The terms ‘soot’ and ‘black carbon’ have been used interchangeably in the atmospheric science community; in this dissertation, we will use the term ‘soot’ hereafter to represent a fractal-like aggregate (consisting of nano-sphere carbon or soot monomers) that is formed due to incomplete combustion of carbonaceous materials (Buseck et al., 2014). I will discuss our preference for the term ‘soot’ in the ‘carbonaceous aerosol’ section 1.2. TBs are brown carbon spheres, typically found in biomass burning smoke, from smoldering combustion and they are a component of brown carbon (Reid et al., 2004; Pósfai et al., 2004). I will discuss more about the properties of soot and TBs in the ‘carbonaceous aerosol’ section 1.2. Before this, I will briefly discuss about the impact of aerosol on human health, atmospheric visibility and climate.

1.1.1 Effect on human health

Soot and ultra-fine particles (UFPs) (size <100 nm in diameter) can penetrate deep inside the lungs having adverse respiratory effects (Nemmar et al., 2002; Mauderly et al., 1988). The lacy morphology of soot aggregates provides higher surface area for a given mass than spherical particles (Kiriya et al., 2017) and studies show that the surface area of particle plays a vital role in determining the toxicity in lungs (Schmid and Stoeger, 2016). A recent study by Shi et al. (2015) showed that lacy soot are the most adhesive particles in the atmosphere, easily aggregating with other materials and further increasing the chemical toxicity (Mauderly et al., 1988). The deposition of UFPs and soot aerosol in the respiratory tract and lungs is affected by the particle morphology and concentration (Peters et al., 1997; Donaldson et al., 2001).

1.1.2 Effect on visibility

Aerosol morphology and mixing state, along with concentration and size, also affect visibility (Langridge et al., 2012; Bäumer et al., 2008; Zhang et al., 2008). For example, Zhang et al. (2008) suggested that the irregular structure of aerosol, like soot aggregates, provides sites for water and other species, such as sulfuric acid, to condense on, increasing the aerosol optical depth and reducing visibility. A visibility study in the megacity of Delhi showed that ~90% of the degraded visibility observed in non-foggy conditions, is contributed by aerosol mostly comprising of soot and water-soluble compounds (Singh and Dey, 2012).

1.1.3 Effect on climate

Aerosol directly and indirectly affect the climate. Their direct effect is due to sunlight absorption and scattering. The nature of aerosol, whether it is mostly absorbing, or scattering is quantified using a parameter called single scattering albedo (SSA). SSA is the ratio of the scattering to the extinction (sum of scattering and absorption) cross sections. A purely scattering particle has an SSA of unity, whereas a strongly absorbing particle has an SSA close to zero. Aerosol emitted from most sources, such as sea-salt

spray, biogenic emissions, and some anthropogenic emissions (e.g., nitrates and sulfates), dominantly scatter light and cause cooling. Carbonaceous aerosol like soot dominantly absorb light and contribute to the warming of the atmosphere (Bond and Bergstrom, 2006), while the effect of brown carbon is highly variable, depending on its optical properties. The absorption or scattering of light by aerosol depends on the particle morphology and elemental composition (Sasano and Browell, 1989; Curtis et al., 2008; Radney et al., 2014).

The indirect aerosol effect involves interactions with clouds (Rosenfeld et al., 2014). Aerosol particles can act as nuclei for cloud droplets and ice crystals formation and, therefore, indirectly affect climate. The ability of aerosol particles to serve as cloud condensation nuclei (CCN) and ice nuclei (IN) depends on various factors; for example, the particle size, the number concentration, the relative humidity and the hygroscopicity (Koehler et al., 2009; Mikhailov et al., 2006; Kumar et al., 2009). A schematic representation of the aerosol direct and indirect effects on climate is shown in Fig. 1-1.

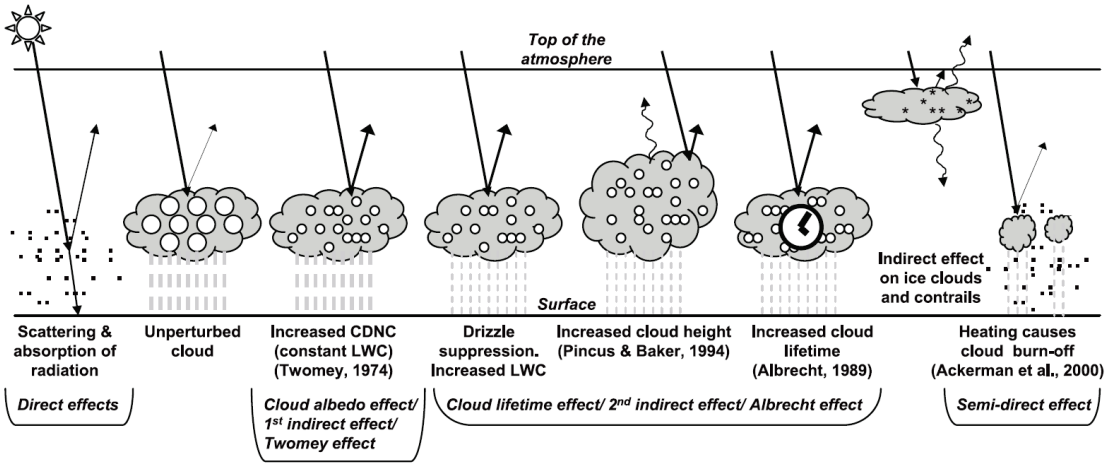

Figure 1-1. Aerosol direct and indirect effects on climate (Fig. 2.10 from Forster, P., V. Ramaswamy, P. Artaxo, T. Berntsen, R. Betts, D.W. Fahey, J. Haywood, J. Lean, D.C. Lowe, G. Myhre, J. Nganga, R. Prinn, G. Raga, M. Schulz and R. Van Dorland, 2007: Changes in Atmospheric Constituents and in Radiative Forcing. In: *Climate Change 2007: The Physical Science Basis. Contribution of Working Group I to the Fourth Assessment Report of the Intergovernmental Panel on Climate Change* [Solomon, S., D. Qin, M. Manning, Z.

Chen, M. Marquis, K.B. Averyt, M.Tignor and H.L. Miller (eds.)]. Cambridge University Press, Cambridge, United Kingdom and New York, NY, USA).

In polluted regions, in a cloud with fixed liquid water content (LWC), the cloud droplet number concentration (CDNC) increases, and the size of each droplet decreases, with increasing aerosol loading. This is known as the first indirect effect (Twomey et al., 1984; Lohmann and Feichter, 2005; Ramaswamy et al., 2001). Since these clouds reflect more light and appear brighter, this leads to a cooling of the atmosphere and the effect is also called cloud-albedo effect. The increased CDNC for a given LWC results also, in a longer lifetime of the clouds, inhibiting precipitation by drizzle suppression (Lohmann and Feichter, 2005; Ramaswamy et al., 2001; Albrecht, 1989). This last effect is known as the second indirect effect or the cloud-lifetime effect. In addition, absorbing aerosol present in a cloud can enhance cloud evaporation reducing cloud cover and resulting in a warming of the atmosphere (Ackerman et al., 2000; Johnson et al., 2004), which is known as the semi-direct effect.

In this dissertation, my prime focus is on a detailed investigation of the morphology and mixing state of aerosol. The goal is to contribute to knowledge that can reduce the uncertainties in the direct effect of aerosol. The indirect and semi-direct effects will not be directly emphasized hereafter.

The direct effect of aerosol in the atmosphere (i.e. atmospheric warming or cooling through direct interaction with the solar radiation) is often quantified in terms of the direct radiative forcing (DRF) at the top of the atmosphere (TOA). DRF at the TOA is the net (down minus up) irradiance at the tropopause (Forster et al., 2007). Tropopause is the boundary between the troposphere and the stratosphere at a height of ~8 km in polar regions and ~16 km equatorial regions, above the mean sea level. A positive TOA-DRF implies warming, while a negative TOA-DRF implies cooling. For an optically thin layer of aerosol, an equation given by Moosmüller and Ogren (2017) can be used to calculate the TOA-DRF. This equation is substantially equivalent to the formulations given by

Haywood and Shine (1995), Charlson et al. (1992), Chylek and Wong (1995) and Lenoble et al. (1982):

$$\Delta F = -\frac{S_0}{2} T^2 (1 - C)\tau[(1 - a_s)^2 \beta(\lambda)\, SSA - 2a_s(1 - SSA)] \quad (1)$$

where S_0 is extraterrestrial solar constant (1370 Wm^{-2}), T is the atmospheric transmission (assumed to be 0.79 (Penner et al., 1992)), τ is the aerosol optical depth, which is a measure of the light attenuation by the aerosol in the atmosphere column, C is the cloud fraction (0.6), a_s is the surface albedo (0.8 for bright surface and 0.06 for ocean) (Haywood and Shine, 1995), SSA is the aerosol single scattering albedo, and β is the hemispherical upscatter fraction. β is a measure of the average fraction of light scattered in the upward hemisphere. Optical parameters like SSA and β depend on the morphology of the aerosol particle. For example, the morphology of a particle affects the light scattering directionality, and therefore, the upscatter fraction (Moosmüller and Ogren, 2017).

The optical properties of aerosol are affected by the mixing state of aerosol as well. During atmospheric processing, aerosol particles often form internal mixtures due to the coagulation with other aerosol or condensation of condensable vapors (Kroll and Seinfeld, 2008), which can change their morphology and optical properties. For example, Bambha et al. (2013) found that the fractal-like soot particle deformed to a compact morphology due to the coating of oleic acid vapors.

In global models, the optical properties of aerosol of different morphology and mixing state are calculated using Lorenz-Mie simulations, by assuming a volume equivalent or a mass equivalent spherical particle. However, Lorenz-Mie simulations can overestimate or underestimate the values of the optical properties of aerosol with complex morphology (such as soot aggregates and irregularly shaped mineral dust). To account for the complex morphology of atmospheric particles, more realistic models been devised, such as the Rayleigh-Debye-Gans (RDG) approximation, the Dipole-Dipole Approximation (DDA) and the T-Matrix method. The RDG approximation is useful to calculate the light

absorption and scattering by fractal aggregates, like soot (Farias et al., 1995; Chakrabarty et al., 2007). In the RDG approximation, monomer-monomer interactions are neglected so that the absorption by an aggregate is simply the product of the absorption by theindividual monomers and the number of monomers present in that aggregate (Sorensen, 2001). Other optical models like DDA and T-Matrix are more computer intensive and advanced, accounting also for the interactions between the monomers. DDA is a commonly used method to calculate the scattering and absorption of electromagnetic radiation by any arbitrarily shaped particle (Draine, 1988; Draine and Flatau, 1994; Purcell and Pennypacker, 1973). In DDA, a particle of any geometry is replaced by an array of dipoles to calculate light absorption and scattering differential cross sections (Scarnato et al., 2013; Wu et al., 2015; Shen et al., 2008). The superposition T-Matrix method can be used to calculate orientation averaged light scattering by an aggregate (Mishchenko et al., 2013; Mackowski and Mishchenko, 1996). In this technique, the total field scattered by an aggregate is represented by the superposition of fields scattered by each monomer in the aggregate. T-Matrix simulations for soot aggregates show that the optical properties of aggregates are significantly affected by the aggregate morphology (Liu and Mishchenko, 2005).

One of the ways to reduce uncertainties in the DRF calculations is to input accurate optical parameters in Equation (1), which can be achieved by using advanced optical methods like DDA and T-Matrix. However, all these methods require detailed information on the particle morphology and mixing state. My dissertation is dedicated to the investigation of the morphology and mixing state of carbonaceous aerosol at the single particle level, using scanning electron microscopy (SEM) and transmission electron microscopy (TEM), along with energy dispersive X-ray spectroscopy (EDS).

1.2 Carbonaceous aerosol

Carbonaceous aerosol are ubiquitous in the atmosphere and are emitted during the combustion of fossil fuels, biofuels, and biomass burning, such as the burning of firewood, grasses and agricultural residues (Horvath, 1993; Einfeld et al., 1991).

Carbonaceous aerosol include soot (black carbon) and organic carbon. In the literature on carbonaceous aerosol, the term ‘soot’ and ‘black carbon’ have been used interchangeably, depending on the measurement techniques employed to measure the particle properties. The community prefers to use the term ‘black carbon’ when the optical properties are measured (Lavanchy et al., 1999; Andreae and Gelencsér, 2006; Cappa et al., 2012) and the term ‘soot’ when one investigates the particle morphology (Köylü et al., 1995; Khalizov et al., 2009; Adachi et al., 2010). The ambiguity in the terms have been discussed elsewhere (Buseck et al., 2014; Petzold et al., 2013). Buseck et al. (2014) suggested using the term ‘ns-soot’ to describe the refractory and light-absorbing component of carbonaceous material where “ns” refers to the monomers or “nano-spheres”. The nano-spheres are clustered together to form a fractal-like or lacy structure and each nano-sphere consists of concentrically wrapped graphene-like layers. Since we have used electron microscopy techniques to study the morphology of individual particles, hereafter we will use the term ‘soot’. Soot and organic carbon (OC) are generally co-emitted. In general, soot forms in high temperature (flaming) combustions (Xi and Zhong, 2006), whereas OC is dominant in low temperature (smoldering) combustions (Chakrabarty et al., 2006; Martins et al., 1998).

OC are often weakly or not absorbing aerosol; however, there are some light absorbing OC aerosol, which show strong absorption in the ultra violet-blue wavelength range and appear brown, hence the term “brown carbon” (BrC). It is to be noted that OC contributes 20-90% of the total aerosol mass in the troposphere (Kanakidou et al., 2005) and the emission sources of OC are multiple, such as from soil (Veghte et al., 2017), from plants as VOCs and from combustion and biomass burning activities. The OC formed during the smoldering combustion of biomass also includes BrC spheres called ‘tar balls’ and these light-absorbing OCs are the particles of interest in chapter four of my dissertation.

1.2.1 Mixing state and morphology of soot and effects on optical properties

1.2.1.1 Mixing state

The mixing state and morphology of soot affect its optical properties. As mentioned above, freshly generated soot has a fractal-like morphology and is usually externally mixed with other particles. The term 'external mixture' here is used to indicate that individual soot aggregates in an ensemble of different particles are not in direct contact, as shown in Fig. 1-2a. 'Internal mixture' refers to the mixing of two or more different types of aerosol materials within the same particle (Fig. 1-2b).

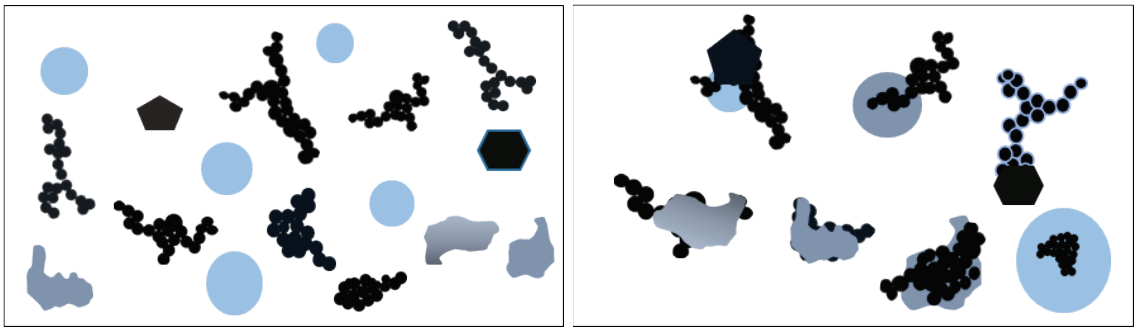

(a) External mixture (b) Internal mixture

Figure 1-2. Schematic representation of **a**) external mixture, **b**) internal mixture of soot with other particles. Lacy black particles represent soot.

During atmospheric processing, soot aggregates interact with other inorganic and organic materials, including water, through condensation and/or coagulation processes and form internal mixtures. In an internal mixture, a soot particle can be fully or partially coated by the condensing materials, or it might be attached to the surface of other particles that coagulated with, or some portion of the soot particle might penetrate inside the host material (Figs. 1-2b and 1-3b). Internal mixing of soot with other material, including that

involving water such as during fog processing or cloud processing, can cause soot compaction and modify the soot optical properties.

As mention earlier, for pragmatic computational reasons, in climate models, internally mixed soot particles are represented using a volume or mass equivalent core-shell configuration and the Lorenz-Mie theory is employed to calculate their optical properties. Core-shell models assume that the soot core lies at the centre and the outer coating material acts as a "lens" refracting the light inward (Fig. 1-3a). For soot with complex morphology like the off-center configuration of soot in Fig. 1-3b, the optical properties are not well estimated by the core-shell model, and advanced models like the DDA and T-Matrix mentioned earlier, would perform much better (Kahnert et al., 2013;Kahnert et al., 2012;Scarnato et al., 2013).

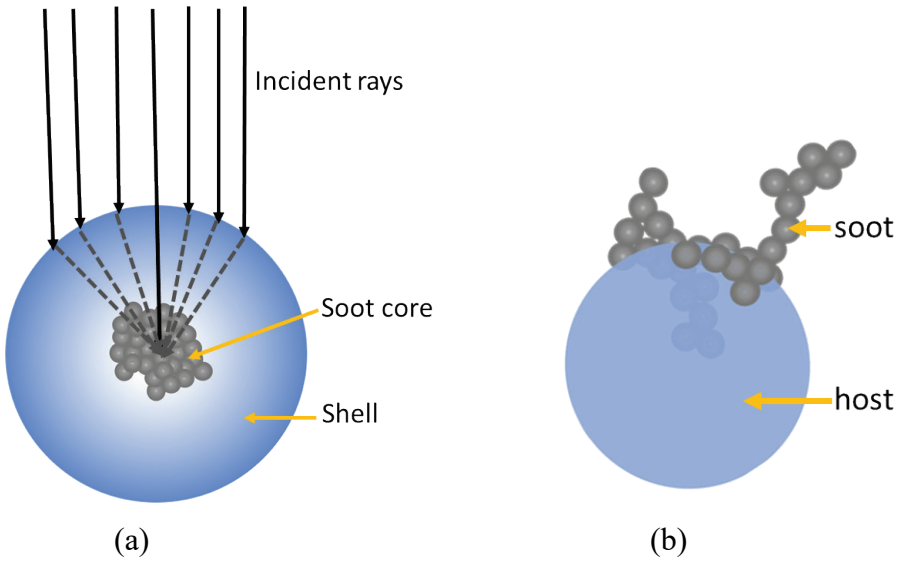

Figure 1-3. Schematic representation of **a**) Core-shell model for a thickly coated soot and **b**) surface-attached soot

Lack and Cappa (2010) showed that the "lensing" effect enhances the absorption by the soot core. Plentiful of studies have shown that coating increases absorption by soot (Lack and Cappa, 2010;Cappa et al., 2012;Khalizov et al., 2009;Ghazi and Olfert, 2013;Slowik et al., 2007;Liu et al., 2015), even when the coating material is completely non-absorbing.

The effect is generally quantified in terms of the absorption enhancement (E_{abs}), which is simply the ratio of absorption by the coated soot to that by the soot core alone, when all the coating material is removed. To calculate the (E_{abs}), firstly the absorption by coated soot is measured. Then, the coating material is removed and finally, the absorption is measured again.

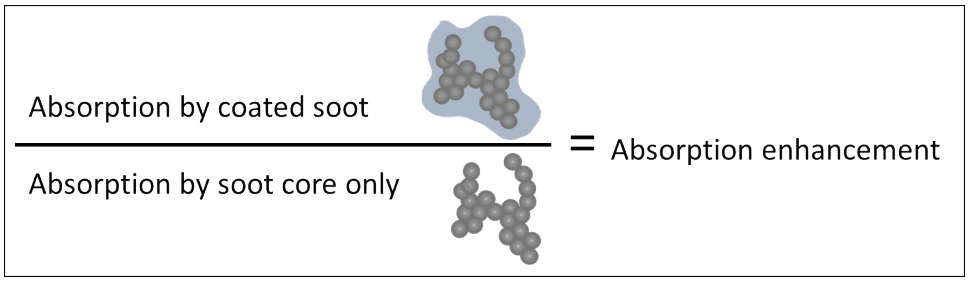

Figure 1-4. Schematic describing how the absorption enhancement for coated soot is calculated.

Studies show a large discrepancy in E_{abs} between laboratory and ambient soot samples up to an order of two (Cappa et al., 2012), suggesting incomplete understanding of the optical properties of mixed soot. Different researchers (Sedlacek et al., 2012; Moteki et al., 2014; Adachi and Buseck, 2013; Adachi et al., 2010) have suggested that the variability in E_{abs} of ambient soot might be due to the internal mixing state of soot. Thermodenuding is commonly used to remove the coating from ambient soot. However, the thermodenuding process if it were changing the core's soot structure would introduce a bias in the estimated E_{abs}. We discuss the effect of thermodenuding on the morphology of fresh soot aggregates in chapter 3.

1.2.1.2 Cloud processing and soot morphology

Atmospheric processing can restructure a fractal-like (lacy) soot (Fig. 1-5a) to a compact morphology (Fig. 1-5b). Freshly emitted soot particles are generally hydrophobic in nature and externally mixed with other particles. Atmospheric processing like soot oxidation, coagulation and coating with other organic and inorganic materials makes

them hydrophilic (Zuberi et al., 2005; Zhang et al., 2008). The fractal-like morphology of soot may provide active sites for adsorption and deposition of water and other chemical species in soot (Popovicheva et al., 2008; Mikhailov et al., 2006). Lacy soot particles collapse to a compact morphology when it is wetted due to surface tension either during evaporation (Ma et al., 2013; Ebert et al., 2002) or condensation (Tritscher et al., 2011; Schnitzler et al., 2017). Fractal-like soot aggregates coated with glutaric acid collapsed to a compact morphology when exposed to high relative humidity due to water processing (Mikhailov et al., 2006). In cold cloud processing experiments conducted at the Pacific Northwest National laboratory, China et al. (2015a) found that diesel soot aggregates restructure to a compact morphology after cloud processing. They found that the SSA of cloud processed soot is enhanced by a factor of up to 1.4, decreasing the DRF by ~63%. In another study of soot samples collected from the free troposphe, China et al. (2015b) found a significant number fraction of compact soot. Interestingly, the compact soot particles were only thinly coated, and they speculated that multiple cloud cycles might have been responsible for the compact morphology. In another study, Huang et al. (1994) speculated that the observation of compact soot aggregates in the Grand Canyon region may be due to the cloud processing of the lacy aggregates, as well. We discuss a systematic study of cloud processed soot particles from laboratory and ambient samples in chapter 2 of this dissertation.

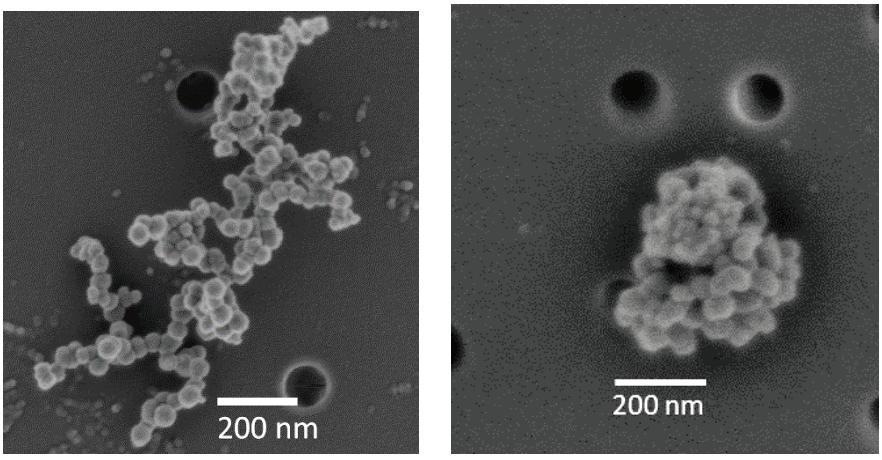

(a) Fresh soot (b) compact soot

Figure 1-5. Scanning Electron Microscope micrographs of **a**) fresh soot from biomass combustion collected in the laboratory at Carnegie Melon University (Saliba et al., 2016), and **b**) compact atmospheric soot collected in the Po Valley, Italy. The dark circles are holes on the substrate.

Studies on the morphology of soot have shown that compact soot has different optical properties than lacy soot (China et al., 2015b;China et al., 2015a;Radney et al., 2014). Based on laboratory experiments, Radney et al. (2014) measured higher absorption (~5%) and scattering (~50%) when lacy soot restructures to a compact morphology. Based on numerical simulations, Liu and Mishchenko (2005) found that the absorption of soot increases by >25% after compaction. Their simulations showed that the SSA increased by >10-fold when lacy soot undergoes compaction. Other studies such as the RDG simulations by Sorensen (2001), DDA simulations by China et al. (2015a), and T-Matrix simulations by Liu et al. (2008) highlight the importance of morphology in determining the soot optical properties and radiative effects.

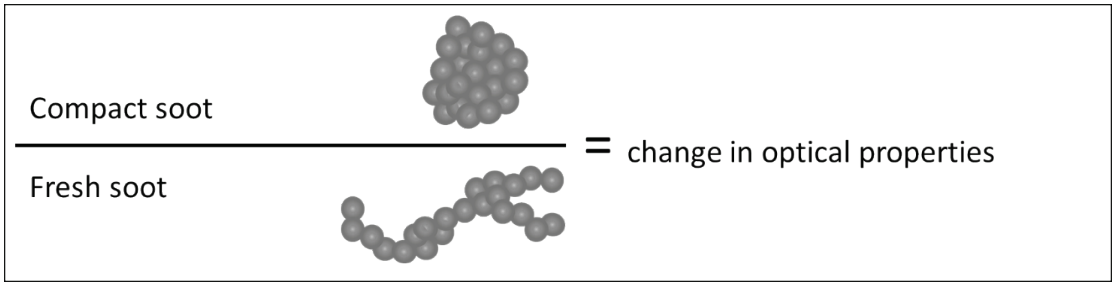

Figure 1-6. Schematic indicating how changes in soot optical properties upon compaction are calculated.

We quantify the morphology of fresh soot aggregates in terms of three morphological parameters; fractal dimension, roundness and convexity (China et al., 2015a). Fractal dimension is used to depict the morphology of an aggregate in term of mass-length relations. For a given mass, if the lacy aggregate restructures to a collapsed morphology, the fractal dimension increases. Fresh soot aggregates exhibit scale invariant properties with a typical 3-D fractal dimension (D_{3F}) of 1.8 (Sorensen et al., 1992), which increases

when the aggregate collapses to a compact morphology, approaching 3 on complete collapse (Fig. 1-7).

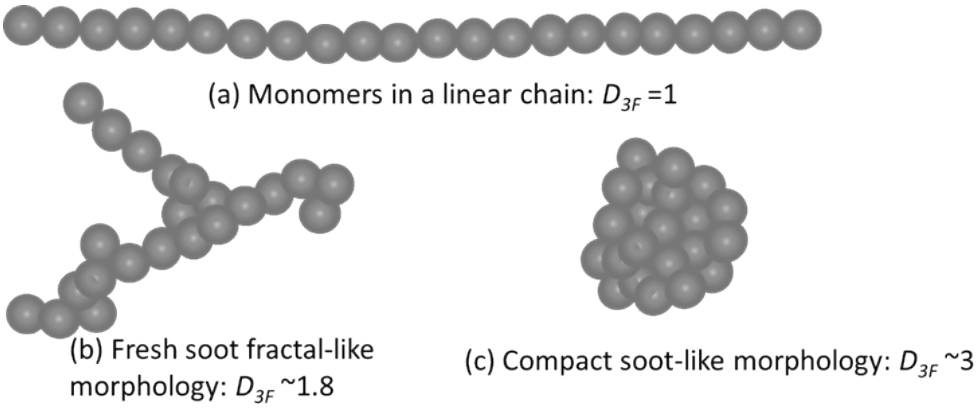

Figure 1-7. Schematic representation of fractal dimension for the arrangement of 22 monomers under different configurations.

Roundness is the ratio of the projected area of a soot aggregate to that of the circle whose diameter corresponds to the maximum length of the aggregate. Convexity is the ratio of the projected area of the aggregate to that of a convex polygon fully inscribing it.

Figure 1-8a) SEM micrograph of a kerosene flame generated soot aggregate during the cloud expansion experiment in the MTU cloud chamber (π-chamber). The shaded portion

in **b**) and **c**) enclosing the binary image of the aggregate shown in the micrograph in (a) represent the convexity and roundness, respectively.

Lacy soot has a lower value of roundness and convexity compared to a compact particle (China et al., 2015b). Roundness, convexity and other morphological parameters are discussed more in chapter 3.

1.2.2 Morphology and optical properties of tar ball aggregates

Tar balls are brown carbon spheres released in the atmosphere during biomass burning (Chakrabarty et al., 2010;Adachi and Buseck, 2011;China et al., 2013;Girotto et al., 2018). In most studies, tar balls (TBs) properties are reported for individual spheres (Hoffer et al., 2016;Liu et al., 2016). However, in a recent study, we found evidences that they can also form aggregates as shown in Fig. 1-9 (Girotto et al. 2018).

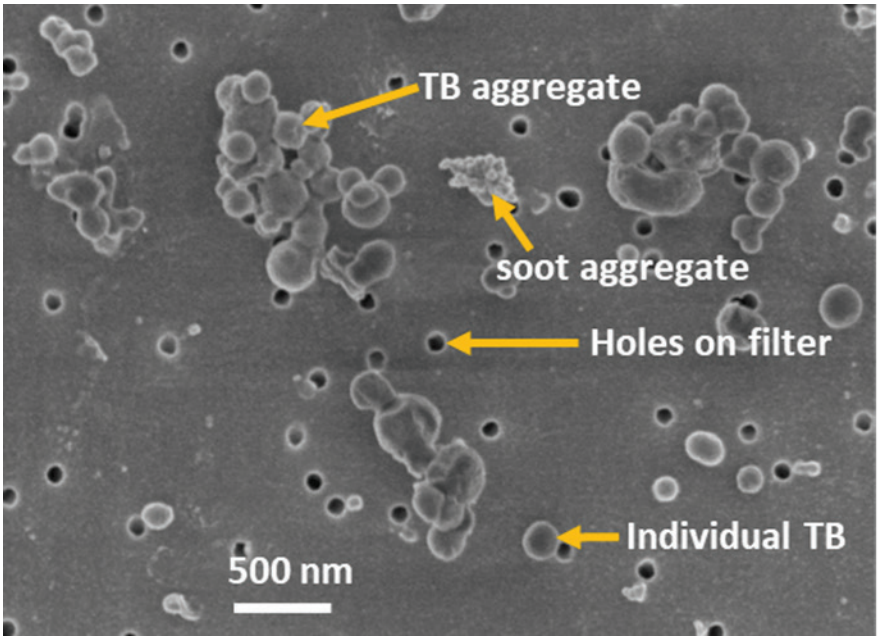

Figure 1-9. SEM micrograph showing the aggregated and individual TBs collected during the Whitewater-Baldy complex Fire, New Mexico, 2012 (Girotto et al., 2018). A soot aggregate is also indicated to highlight the differences in monomer size that allows to clearly distinguishing soot from TB aggregates.

TB aggregates are composed of tens of TBs. Unlike soot aggregates that are composed of monomers of diameter of 10-50 nm (Köylü et al., 1995), TBs are much larger (100-300 nm) (Pósfai et al., 2003) and are therefore easily distinguishable.

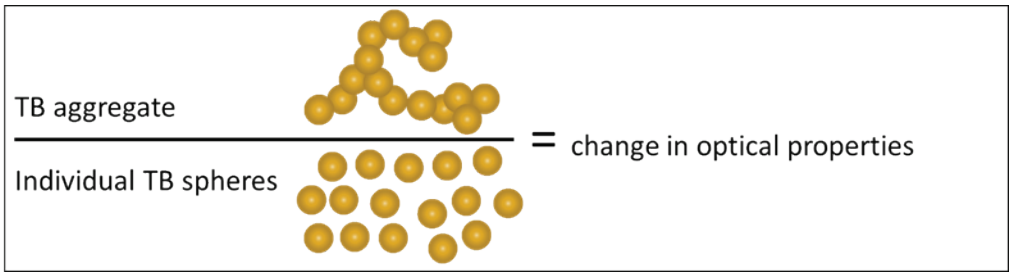

Fig.1-10. Schematic showing how the changes in optical properties of aggregated TBs and independent TBs can be calculated.

The aggregation of TBs can also have a significant effect on the optical properties, which has not been investigated before. Therefore, it becomes necessary to study the optical properties of TB aggregates and their radiative effects that I discuss in chapter 4 of this dissertation.

1.3 Organization of the dissertation

The dissertation is divided into 5 chapters including this introduction (chapter 1) and the conclusions (chapter 5). Because each chapter is based on published journal articles (chapter 3 is published and chapter 4 is currently under review for publication) or is the base for a future publication (chapters, 2), each starts with a brief introduction, followed by a method, a result and discussion, and a conclusion sections. All my research is based on the electron microscopy study of carbonaceous aerosol which is shown in Fig. 1-11. In chapter 4, based on electron microscopy finding, I simulated the optical properties for TB aggregates. A brief description of each chapter is provided next:

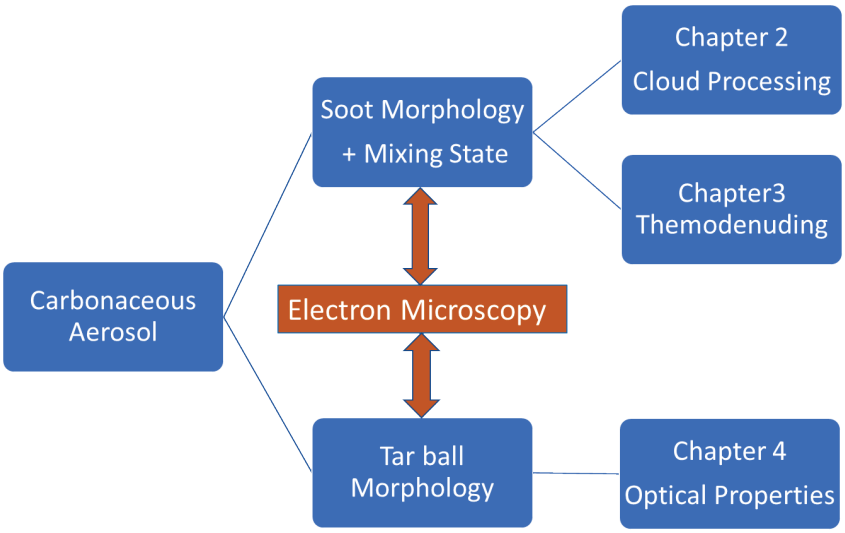

Figure 1-11. Schematic showing electron microscopy as a basis for the study of soot and tar ball.

Chapter 2 discusses cloud processing of soot particles. In particular, we investigate how the morphology of soot changes after water condenses and evaporates onto the particles, in laboratory and ambient samples. We find that the particles undergo compaction after cloud processing. The work presented in this chapter constitute the main body of a manuscript in preparation, expected to be submitted in the '*Journal of Geophysical Research: Atmospheres*' by early fall of 2018.

Chapter 3 deals with the investigation of the morphology of fresh soot particles upon thermodenuding. As mentioned earlier, thermodenuding is a common technique employed for the removal of volatile coating materials from soot. Our concern in this study was to find out whether thermodenuding alone changes the structural integrity of soot particles. Our findings show that thermodenuding does not cause appreciable morphological changes. This work is published in the open access journal *Atmosphere* (Bhandari et al., 2017).

Chapter 4 presents an extensive numerical simulations study of the optical properties and radiative forcing of TB aggregates and compare them with those of individual TBs.

We show that aggregation does affect the radiative properties of TBs and that Mie simulations are often not appropriate. The work presented in chapter 4 has been submitted to the '*Journal of Quantitative Spectroscopy and Radiative Transfer*' for publication and is currently under review.

Chapter 5 is a summary of my research and includes a critical discussion of my research and its broader implications.

1.4 References

1. Ackerman, A. S., Toon, O., Stevens, D., Heymsfield, A., Ramanathan, V., and Welton, E.: Reduction of tropical cloudiness by soot, Science, 288, 1042-1047, 2000.
2. Adachi, K., Chung, S. H., and Buseck, P. R.: Shapes of soot aerosol particles and implications for their effects on climate, Journal of Geophysical Research: Atmospheres (1984–2012), 115, 2010.
3. Adachi, K., and Buseck, P. R.: Atmospheric tar balls from biomass burning in Mexico, Journal of Geophysical Research: Atmospheres, 116, 2011.
4. Adachi, K., and Buseck, P. R.: Changes of ns-soot mixing states and shapes in an urban area during CalNex, Journal of Geophysical Research: Atmospheres, 118, 3723-3730, 2013.
5. Albrecht, B. A.: Aerosols, cloud microphysics, and fractional cloudiness, Science, 245, 1227-1230, 1989.
6. Andreae, M., and Gelencsér, A.: Black carbon or brown carbon? The nature of light-absorbing carbonaceous aerosols, Atmospheric Chemistry and Physics, 6, 3131-3148, 2006.
7. Bambha, R. P., Dansson, M. A., Schrader, P. E., and Michelsen, H. A.: Effects of volatile coatings and coating removal mechanisms on the morphology of graphitic soot, Carbon, 61, 80-96, 2013.
8. Bäumer, D., Vogel, B., Versick, S., Rinke, R., Möhler, O., and Schnaiter, M.: Relationship of visibility, aerosol optical thickness and aerosol size distribution in an ageing air mass over South-West Germany, Atmospheric Environment, 42, 989-998, 2008.
9. Bhandari, J., China, S., Onasch, T., Wolff, L., Lambe, A., Davidovits, P., Cross, E., Ahern, A., Olfert, J., Dubey, M., and Mazzoleni, C.: Effect of Thermodenuding on the Structure of Nascent Flame Soot Aggregates, Atmosphere, 8, 166, 2017.
10. Bond, T. C., and Bergstrom, R. W.: Light absorption by carbonaceous particles: An investigative review, Aerosol science and technology, 40, 27-67, 2006.
11. Bond, T. C., Doherty, S. J., Fahey, D., Forster, P., Berntsen, T., DeAngelo, B., Flanner, M., Ghan, S., Kärcher, B., and Koch, D.: Bounding the role of black carbon in the climate system: A scientific assessment, Journal of Geophysical Research: Atmospheres, 118, 5380-5552, 2013.

12. Buseck, P. R., Adachi, K., Gelencsér, A., Tompa, É., and Pósfai, M.: Ns-Soot: A Material-Based Term for Strongly Light-Absorbing Carbonaceous Particles, Aerosol Science and Technology, 48, 2014.

13. Cappa, C. D., Onasch, T. B., Massoli, P., Worsnop, D. R., Bates, T. S., Cross, E. S., Davidovits, P., Hakala, J., Hayden, K. L., and Jobson, B. T.: Radiative absorption enhancements due to the mixing state of atmospheric black carbon, Science, 337, 1078-1081, 2012.

14. Chakrabarty, R., Moosmüller, H., Chen, L.-W., Lewis, K., Arnott, W., Mazzoleni, C., Dubey, M., Wold, C., Hao, W., and Kreidenweis, S.: Brown carbon in tar balls from smoldering biomass combustion, Atmospheric Chemistry and Physics, 10, 6363-6370, 2010.

15. Chakrabarty, R. K., Moosmüller, H., Garro, M. A., Arnott, W. P., Walker, J., Susott, R. A., Babbitt, R. E., Wold, C. E., Lincoln, E. N., and Hao, W. M.: Emissions from the laboratory combustion of wildland fuels: Particle morphology and size, Journal of Geophysical Research: Atmospheres, 111, 2006.

16. Chakrabarty, R. K., Moosmüller, H., Arnott, W. P., Garro, M. A., Slowik, J. G., Cross, E. S., Han, J.-H., Davidovits, P., Onasch, T. B., and Worsnop, D. R.: Light scattering and absorption by fractal-like carbonaceous chain aggregates: Comparison of theories and experiment, Applied optics, 46, 6990-7006, 2007.

17. Charlson, R. J., Schwartz, S., Hales, J., Cess, R. D., Coakley, J. J., Hansen, J., and Hofmann, D.: Climate forcing by anthropogenic aerosols, Science, 255, 423-430, 1992.

18. China, S., Mazzoleni, C., Gorkowski, K., Aiken, A. C., and Dubey, M. K.: Morphology and mixing state of individual freshly emitted wildfire carbonaceous particles, Nature communications, 4, 2013.

19. China, S., Kulkarni, G., Scarnato, B. V., Sharma, N., Pekour, M., Shilling, J. E., Wilson, J., Zelenyuk, A., Chand, D., and Liu, S.: Morphology of diesel soot residuals from supercooled water droplets and ice crystals: implications for optical properties, Environmental Research Letters, 10, 114010, 2015a.

20. China, S., Scarnato, B., Owen, R. C., Zhang, B., Ampadu, M. T., Kumar, S., Dzepina, K., Dziobak, M. P., Fialho, P., and Perlinger, J. A.: Morphology and Mixing State of Aged Soot Particles at a Remote Marine Free Troposphere Site: Implications for Optical Properties, Geophysical Research Letters, 2015b.

21. Chylek, P., and Wong, J.: Effect of absorbing aerosols on global radiation budget, Geophysical research letters, 22, 929-931, 1995.

22. Curtis, D. B., Meland, B., Aycibin, M., Arnold, N. P., Grassian, V. H., Young, M. A., and Kleiber, P. D.: A laboratory investigation of light scattering from

representative components of mineral dust aerosol at a wavelength of 550 nm, Journal of Geophysical Research: Atmospheres, 113, 2008.

23. Donaldson, K., Stone, V., Clouter, A., Renwick, L., and MacNee, W.: Ultrafine particles, Occupational and environmental medicine, 58, 211-216, 2001.

24. Draine, B. T.: The discrete-dipole approximation and its application to interstellar graphite grains, The Astrophysical Journal, 333, 848-872, 1988.

25. Draine, B. T., and Flatau, P. J.: Discrete-dipole approximation for scattering calculations, JOSA A, 11, 1491-1499, 1994.

26. Ebert, M., Inerle-Hof, M., and Weinbruch, S.: Environmental scanning electron microscopy as a new technique to determine the hygroscopic behaviour of individual aerosol particles, Atmospheric Environment, 36, 5909-5916, 2002.

27. Einfeld, W., Ward, D. E., and Hardy, C.: Effects of fire behavior on prescribed fire smoke characteristics: A case study, in: Global biomass burning. Atmospheric, climatic, and biospheric implications, 1991.

28. Farias, T. L., Carvalho, M. d. G., Köylü, U. O., and Faeth, G.: Computational evaluation of approximate Rayleigh–Debye–Gans/fractal-aggregate theory for the absorption and scattering properties of soot, Journal of Heat Transfer, 117, 152-159, 1995.

29. Forster, P., Ramaswamy, V., Artaxo, P., Berntsen, T., Betts, R., Fahey, D. W., Haywood, J., Lean, J., Lowe, D. C., and Myhre, G.: Changes in atmospheric constituents and in radiative forcing. Chapter 2, in: Climate Change 2007. The Physical Science Basis, 2007.

30. Ghazi, R., and Olfert, J.: Coating mass dependence of soot aggregate restructuring due to coatings of oleic acid and dioctyl sebacate, Aerosol Science and Technology, 47, 192-200, 2013.

31. Girotto, G., China, S., Bhandari, J., Gorkowski, K., Scarnato, B. V., Capek, T., Marinoni, A., Veghte, D. P., Kulkarni, G., Aiken, A. C., Dubey, M., and Mazzoleni, C.: Fractal-like Tar Ball Aggregates from Wildfire Smoke, Environmental Science & Technology Letters, 10.1021/acs.estlett.8b00229, 2018.

32. Hallquist, M., Wenger, J., Baltensperger, U., Rudich, Y., Simpson, D., Claeys, M., Dommen, J., Donahue, N., George, C., and Goldstein, A.: The formation, properties and impact of secondary organic aerosol: current and emerging issues, Atmospheric chemistry and physics, 9, 5155-5236, 2009.

33. Haywood, J., and Shine, K.: The effect of anthropogenic sulfate and soot aerosol on the clear sky planetary radiation budget, Geophysical Research Letters, 22, 603-606, 1995.

34. Haywood, J., and Boucher, O.: Estimates of the direct and indirect radiative forcing due to tropospheric aerosols: A review, Reviews of geophysics, 38, 513-543, 2000.

35. Hoffer, A., Tóth, A., Nyirő-Kósa, I., Pósfai, M., and Gelencsér, A.: Light absorption properties of laboratory-generated tar ball particles, Atmospheric Chemistry and Physics, 16, 239-246, 2016.

36. Horvath, H.: Atmospheric light absorption—A review, Atmospheric Environment. Part A. General Topics, 27, 293-317, 1993.

37. Huang, P.-F., Turpin, B. J., Pipho, M. J., Kittelson, D. B., and McMurry, P. H.: Effects of water condensation and evaporation on diesel chain-agglomerate morphology, Journal of Aerosol Science, 25, 447-459, 1994.

38. Johnson, B., Shine, K., and Forster, P.: The semi-direct aerosol effect: Impact of absorbing aerosols on marine stratocumulus, Quarterly Journal of the Royal Meteorological Society, 130, 1407-1422, 2004.

39. Kahnert, M., Nousiainen, T., Lindqvist, H., and Ebert, M.: Optical properties of light absorbing carbon aggregates mixed with sulfate: assessment of different model geometries for climate forcing calculations, Optics Express, 20, 10042-10058, 2012.

40. Kahnert, M., Nousiainen, T., and Lindqvist, H.: Models for integrated and differential scattering optical properties of encapsulated light absorbing carbon aggregates, Optics express, 21, 7974-7993, 2013.

41. Kanakidou, M., Seinfeld, J., Pandis, S., Barnes, I., Dentener, F., Facchini, M., Dingenen, R. V., Ervens, B., Nenes, A., and Nielsen, C.: Organic aerosol and global climate modelling: a review, Atmospheric Chemistry and Physics, 5, 1053-1123, 2005.

42. Khalizov, A. F., Xue, H., Wang, L., Zheng, J., and Zhang, R.: Enhanced light absorption and scattering by carbon soot aerosol internally mixed with sulfuric acid, The Journal of Physical Chemistry A, 113, 1066-1074, 2009.

43. Kiriya, M., Okuda, T., Yamazaki, H., Hatoya, K., Kaneyasu, N., Uno, I., Nishita, C., Hara, K., Hayashi, M., and Funato, K.: Monthly and diurnal variation of the Concentrations of Aerosol Surface Area in Fukuoka, Japan, measured by diffusion charging method, Atmosphere, 8, 114, 2017.

44. Koehler, K. A., DeMott, P. J., Kreidenweis, S. M., Popovicheva, O. B., Petters, M. D., Carrico, C. M., Kireeva, E. D., Khokhlova, T. D., and Shonija, N. K.: Cloud condensation nuclei and ice nucleation activity of hydrophobic and hydrophilic soot particles, Physical Chemistry Chemical Physics, 11, 7906-7920, 2009.

45. Köylü, Ü. Ö., Faeth, G., Farias, T. L., and Carvalho, M. d. G.: Fractal and projected structure properties of soot aggregates, Combustion and Flame, 100, 621-633, 1995.

46. Kroll, J. H., and Seinfeld, J. H.: Chemistry of secondary organic aerosol: Formation and evolution of low-volatility organics in the atmosphere, Atmospheric Environment, 42, 3593-3624, 2008.

47. Kumar, P., Nenes, A., and Sokolik, I. N.: Importance of adsorption for CCN activity and hygroscopic properties of mineral dust aerosol, Geophysical Research Letters, 36, 2009.

48. Lack, D., and Cappa, C.: Impact of brown and clear carbon on light absorption enhancement, single scatter albedo and absorption wavelength dependence of black carbon, Atmospheric Chemistry and Physics, 10, 4207-4220, 2010.

49. Langridge, J. M., Lack, D., Brock, C. A., Bahreini, R., Middlebrook, A. M., Neuman, J. A., Nowak, J. B., Perring, A. E., Schwarz, J. P., and Spackman, J. R.: Evolution of aerosol properties impacting visibility and direct climate forcing in an ammonia-rich urban environment, Journal of Geophysical Research: Atmospheres, 117, 2012.

50. Lavanchy, V., Gäggeler, H., Nyeki, S., and Baltensperger, U.: Elemental carbon (EC) and black carbon (BC) measurements with a thermal method and an aethalometer at the high-alpine research station Jungfraujoch, Atmospheric Environment, 33, 2759-2769, 1999.

51. Lenoble, J., Tanre, D., Deschamps, P., and Herman, M.: A simple method to compute the change in earth-atmosphere radiative balance due to a stratospheric aerosol layer, Journal of the Atmospheric Sciences, 39, 2565-2576, 1982.

52. Liu, C., Chung, C. E., Zhang, F., and Yin, Y.: The colors of biomass burning aerosols in the atmosphere, Scientific reports, 6, 28267, 2016.

53. Liu, L., and Mishchenko, M. I.: Effects of aggregation on scattering and radiative properties of soot aerosols, Journal of Geophysical Research: Atmospheres, 110, 2005.

54. Liu, L., Mishchenko, M. I., and Arnott, W. P.: A study of radiative properties of fractal soot aggregates using the superposition T-matrix method, Journal of Quantitative Spectroscopy and Radiative Transfer, 109, 2656-2663, 2008.

55. Liu, S., Aiken, A. C., Gorkowski, K., Dubey, M. K., Cappa, C. D., Williams, L. R., Herndon, S. C., Massoli, P., Fortner, E. C., and Chhabra, P. S.: Enhanced light absorption by mixed source black and brown carbon particles in UK winter, Nature communications, 6, 2015.

56. Lohmann, U., and Feichter, J.: Global indirect aerosol effects: a review, Atmospheric Chemistry and Physics, 5, 715-737, 2005.

57. Ma, X., Zangmeister, C. D., Gigault, J., Mulholland, G. W., and Zachariah, M. R.: Soot aggregate restructuring during water processing, Journal of Aerosol Science, 66, 209-219, 2013.

58. Mackowski, D. W., and Mishchenko, M. I.: Calculation of the T matrix and the scattering matrix for ensembles of spheres, JOSA A, 13, 2266-2278, 1996.

59. Martins, J. V., Hobbs, P. V., Weiss, R. E., and Artaxo, P.: Sphericity and morphology of smoke particles from biomass burning in Brazil, Journal of Geophysical Research: Atmospheres, 103, 32051-32057, 1998.

60. Mauderly, J. L., Gillett, N. A., Henderson, R. F., Jones, R. K., and McClellan, R. O.: Relationships of lung structural and functional changes to accumulation of diesel exhaust particles, in: Inhaled Particles VI, Elsevier, 659-669, 1988.

61. Mikhailov, E., Vlasenko, S., Podgorny, I., Ramanathan, V., and Corrigan, C.: Optical properties of soot–water drop agglomerates: An experimental study, Journal of Geophysical Research: Atmospheres, 111, 2006.

62. Mishchenko, M. I., Liu, L., and Mackowski, D. W.: T-matrix modeling of linear depolarization by morphologically complex soot and soot-containing aerosols, Journal of Quantitative Spectroscopy and Radiative Transfer, 123, 135-144, 2013.

63. Moosmüller, H., and Ogren, J. A.: Parameterization of the Aerosol Upscatter Fraction as Function of the Backscatter Fraction and Their Relationships to the Asymmetry Parameter for Radiative Transfer Calculations, Atmosphere, 8, 133, 2017.

64. Moteki, N., Kondo, Y., and Adachi, K.: Identification by single-particle soot photometer of black carbon particles attached to other particles: Laboratory experiments and ground observations in Tokyo, Journal of Geophysical Research: Atmospheres, 119, 1031-1043, 2014.

65. Nemmar, A., Hoet, P. M., Vanquickenborne, B., Dinsdale, D., Thomeer, M., Hoylaerts, M., Vanbilloen, H., Mortelmans, L., and Nemery, B.: Passage of inhaled particles into the blood circulation in humans, Circulation, 105, 411-414, 2002.

66. Penner, J. E., Dickinson, R. E., and O'Neill, C. A.: Effects of aerosol from biomass burning on the global radiation budget, Science, 256, 1432-1435, 1992.

67. Peters, A., Wichmann, H. E., Tuch, T., Heinrich, J., and Heyder, J.: Respiratory effects are associated with the number of ultrafine particles, American journal of respiratory and critical care medicine, 155, 1376-1383, 1997.

68. Petzold, A., Ogren, J. A., Fiebig, M., Laj, P., Li, S.-M., Baltensperger, U., Holzer-Popp, T., Kinne, S., Pappalardo, G., and Sugimoto, N.: Recommendations for

reporting" black carbon" measurements, Atmospheric Chemistry and Physics, 13, 8365-8379, 2013.

69. Popovicheva, O., Persiantseva, N. M., Shonija, N. K., DeMott, P., Koehler, K., Petters, M., Kreidenweis, S., Tishkova, V., Demirdjian, B., and Suzanne, J.: Water interaction with hydrophobic and hydrophilic soot particles, Physical Chemistry Chemical Physics, 10, 2332-2344, 2008.

70. Pósfai, M., Simonics, R., Li, J., Hobbs, P. V., and Buseck, P. R.: Individual aerosol particles from biomass burning in southern Africa: 1. Compositions and size distributions of carbonaceous particles, Journal of Geophysical Research: Atmospheres, 108, 2003.

71. Pósfai, M., Gelencsér, A., Simonics, R., Arató, K., Li, J., Hobbs, P. V., and Buseck, P. R.: Atmospheric tar balls: Particles from biomass and biofuel burning, Journal of Geophysical Research: Atmospheres, 109, 2004.

72. Purcell, E. M., and Pennypacker, C. R.: Scattering and absorption of light by nonspherical dielectric grains, The Astrophysical Journal, 186, 705-714, 1973.

73. Radney, J. G., You, R., Ma, X., Conny, J. M., Zachariah, M. R., Hodges, J. T., and Zangmeister, C. D.: Dependence of soot optical properties on particle morphology: measurements and model comparisons, Environmental science & technology, 48, 3169-3176, 2014.

74. Ramaswamy, V., Boucher, O., Haigh, J., Hauglustine, D., Haywood, J., Myhre, G., Nakajima, T., Shi, G., and Solomon, S.: Radiative forcing of climate, Climate change, 349, 2001.

75. Reid, J. P., and Sayer, R. M.: Heterogeneous atmospheric aerosol chemistry: laboratory studies of chemistry on water droplets, Chemical Society Reviews, 32, 70-79, 2003.

76. Reid, J. S., Koppmann, R., Eck, T. F., and Eleuterio, D. P.: A review of biomass burning emissions, part II: Intensive physical properties of biomass burning particles, Atmospheric Chemistry and Physics Discussions, 4, 5135-5200, 2004.

77. Rosenfeld, D., Sherwood, S., Wood, R., and Donner, L.: Climate effects of aerosol-cloud interactions, Science, 343, 379-380, 2014.

78. Saleh, R., Marks, M., Heo, J., Adams, P. J., Donahue, N. M., and Robinson, A. L.: Contribution of brown carbon and lensing to the direct radiative effect of carbonaceous aerosols from biomass and biofuel burning emissions, Journal of Geophysical Research: Atmospheres, 120, 2015.

79. Sasano, Y., and Browell, E. V.: Light scattering characteristics of various aerosol types derived from multiple wavelength lidar observations, Applied Optics, 28, 1670-1679, 1989.

80. Scarnato, B., Vahidinia, S., Richard, D., and Kirchstetter, T.: Effects of internal mixing and aggregate morphology on optical properties of black carbon using a discrete dipole approximation model, Atmospheric Chemistry and Physics, 13, 5089-5101, 2013.

81. Schmid, O., and Stoeger, T.: Surface area is the biologically most effective dose metric for acute nanoparticle toxicity in the lung, Journal of Aerosol Science, 99, 133-143, 2016.

82. Schnitzler, E. G., Gac, J. M., and Jäger, W.: Coating surface tension dependence of soot aggregate restructuring, Journal of Aerosol Science, 106, 43-55, 2017.

83. Sedlacek, A. J., Lewis, E. R., Kleinman, L., Xu, J., and Zhang, Q.: Determination of and evidence for non-core-shell structure of particles containing black carbon using the Single-Particle Soot Photometer (SP2), Geophysical Research Letters, 39, 2012.

84. Shen, Y., Draine, B., and Johnson, E. T.: Modeling porous dust grains with ballistic aggregates. I. Geometry and optical properties, The Astrophysical Journal, 689, 260, 2008.

85. Shi, Y., Ji, Y., Sun, H., Hui, F., Hu, J., Wu, Y., Fang, J., Lin, H., Wang, J., and Duan, H.: Nanoscale characterization of PM 2.5 airborne pollutants reveals high adhesiveness and aggregation capability of soot particles, Scientific reports, 5, 11232, 2015.

86. Singh, A., and Dey, S.: Influence of aerosol composition on visibility in megacity Delhi, Atmospheric environment, 62, 367-373, 2012.

87. Slowik, J. G., Cross, E. S., Han, J.-H., Davidovits, P., Onasch, T. B., Jayne, J. T., Williams, L. R., Canagaratna, M. R., Worsnop, D. R., and Chakrabarty, R. K.: An inter-comparison of instruments measuring black carbon content of soot particles, Aerosol Science and Technology, 41, 295-314, 2007.

88. Sorensen, C., Cai, J., and Lu, N.: Light-scattering measurements of monomer size, monomers per aggregate, and fractal dimension for soot aggregates in flames, Applied Optics, 31, 6547-6557, 1992.

89. Sorensen, C.: Light scattering by fractal aggregates: a review, Aerosol Science & Technology, 35, 648-687, 2001.

90. Tritscher, T., Jurányi, Z., Martin, M., Chirico, R., Gysel, M., Heringa, M. F., DeCarlo, P. F., Sierau, B., Prévôt, A. S., and Weingartner, E.: Changes of hygroscopicity and morphology during ageing of diesel soot, Environmental Research Letters, 6, 034026, 2011.

91. Twomey, S. A., Piepgrass, M., and Wolfe, T.: An assessment of the impact of pollution on global cloud albedo, Tellus B, 36, 356-366, 1984.

92. Veghte, D. P., China, S., Weis, J., Kovarik, L., Gilles, M. K., and Laskin, A.: Optical Properties of Airborne Soil Organic Particles, ACS Earth and Space Chemistry, 1, 511-521, 2017.

93. Wu, Y., Cheng, T., Zheng, L., Chen, H., and Xu, H.: Single scattering properties of semi-embedded soot morphologies with intersecting and non-intersecting surfaces of absorbing spheres and non-absorbing host, Journal of Quantitative Spectroscopy and Radiative Transfer, 157, 1-13, 2015.

94. Xi, J., and Zhong, B. J.: Soot in diesel combustion systems, Chemical engineering & technology, 29, 665-673, 2006.

95. Zhang, R., Khalizov, A. F., Pagels, J., Zhang, D., Xue, H., and McMurry, P. H.: Variability in morphology, hygroscopicity, and optical properties of soot aerosols during atmospheric processing, Proceedings of the National Academy of Sciences, 105, 10291-10296, 2008.

96. Zuberi, B., Johnson, K. S., Aleks, G. K., Molina, L. T., Molina, M. J., and Laskin, A.: Hydrophilic properties of aged soot, Geophysical research letters, 32, 2005.

2 Chapter 2: Soot compaction during cloud processing: observation from laboratory and field studies[1]

2.1 Abstract

Soot particles form during combustion of carbonaceous materials. When freshly emitted they are typically fractal-like aggregates consisting of several nanometer-sized monomers and are hydrophobic. However, soot particles become hydrophilic after atmospheric aging and can act as cloud condensation nuclei. Water condensation and evaporation processes can restructure the soot aggregates to a more compact morphology, affecting their optical, aerodynamic, and surface properties. We use electron microscopy to investigate morphological changes in single soot particles from laboratory and ambient samples. We collected ambient samples in the Po Valley in Northern Italy, location affected by high pollution levels and frequent fog events. We found that during periods of fog, a fraction of the soot particles restructured to a more compact morphology. We then performed laboratory experiments to simulate atmospheric cloud processing of soot under controlled conditions. For these laboratory experiments, we generated soot through kerosene combustion and used the Michigan Technological University cloud chamber to generate a cloud. We found that soot sampled after evaporating the cloud water droplets (residuals) were much more compact than freshly emitted soot, suggesting that indeed, cloud processing results in soot compaction. To put our results in a broader context, we conclude our discussion by surveying the morphological characteristics of soot particles from several ambient samples collected at various locations, under different environmental and aging conditions.

[1] Based on the manuscript in preparation for the '*Journal of Geophysical Research: Atmospheres*' (to be submitted in fall of 2018).

2.2 Introduction

Soot particles are ubiquitous in the atmosphere (Penner et al., 1993;Pósfai et al., 1999;Bond et al., 2013;Katrinak et al., 1993). They are emitted during incomplete combustion of carbonaceous materials like fossil fuels or biomass (Tivanski et al., 2007;Pósfai et al., 2003;Slowik et al., 2004). They strongly absorb solar radiation; therefore, affect the Earth's radiative balance through aerosol-radiation interactions, as well as, by affecting clouds, surface albedo and atmospheric stability (Horvath, 1993;Haywood and Boucher, 2000;Ramaswamy et al., 2001). Because of their unique optical properties, soot particles represent one of the strongest positive anthropogenic radiative forcers, possibly second only to CO_2 (Ramanathan and Carmichael, 2008;Jacobson, 2001). Concentrations and optical properties of soot particles depend on their evolution in the atmosphere. In particular, freshly emitted soot particles are fractal-like lacy aggregates, composed of nanometer-sized soot monomers (also called spherules or nano-spheres) (DeCarlo et al., 2004;Adachi and Buseck, 2008;Sorensen et al., 1992). However, aged soot particles often have more compact morphologies, and this transformation affects the particles' optical, aerodynamic, and surface properties. Therefore, understanding these transformations is key to correctly representing the properties of soot in climate models.

Fresh soot is typically hydrophobic and externally mixed with other aerosol components (Saleh et al., 2014;Slowik et al., 2007;Zuberi et al., 2005;Weingartner et al., 1997;Van Poppel et al., 2005). Soot becomes hydrophilic over time due to aging processes such as condensation of organic or inorganic compounds on its surface, and coagulation with other particles (Saleh et al., 2014;Martins et al., 1998;Reid et al., 2005;Kotzick and Niessner, 1999;Russell et al., 2002). In addition, atmospheric oxidizing agents such as ozone, hydroxyl radicals, and NO_x promote the formation of oxygen-containing polar functional groups (e.g., carboxylates) on the soot surface, also making it more hydrophilic (Smith and Chughtai, 1997;Smith et al., 1989;Decesari et al., 2002;Lary et al., 1999;Kotzick et al., 1997;Fenimore and Jones, 1967). Hydrophilic soot particles can act as cloud condensation nuclei (CCN) at atmospherically relevant supersaturation conditions (Zuberi et al., 2005);

whereas, hydrophobic soot, such as graphitized thermal soot, requires much higher supersaturation to activate (Koehler et al., 2009).

Coating material on the surface of soot, including cloud water condensing upon activation, can exert capillary forces between the monomers and cause the aggregate to restructure to a compact morphology (Shingler et al., 2016;Khalizov et al., 2013;Kütz and Schmidt-Ott, 1992;Cross et al., 2010). A detailed discussion on the water uptake by soot aggregates, based on surface polarity, from different fuel sources, is reported by Popovicheva et al. (2008). A schematic representation of a lacy soot aggregate and a compact soot particle is shown in Figs. 2-1a and b), respectively. Some researchers proposed that soot compaction occurs during the condensation of water, due to surface tension (Tritscher et al., 2011;Schnitzler et al., 2017;Hallett et al., 1989), while others argued that the compaction occurs during evaporation (Ma et al., 2013;Ebert et al., 2002;Zuberi et al., 2005;Mikhailov et al., 2006). For example, Mikhailov et al. (2006) proposed that at saturation, i.e., at a relative humidity (RH) of 100%, active sites on hydrophilic soot particles stimulate the nucleation and growth of water droplets that exert surface tension on the soot branches during the evaporation, collapsing the soot structure.

(a) Lacy soot aggregate (b) Compact soot

Figure 2-1. Soot particles: **a**) lacy aggregate and, **b**) compact aggregate, containing 21 monomers each.

Therefore, cloud processing can be an important route to soot compaction. For example, China et al. (2015c) found that soot particles collected in the North Atlantic free troposphere were in significant fraction very compact, even when no significant coating material was detected on the particles. They hypothesized that the compaction was due to

cloud processing during long-range atmospheric transport. In another laboratory study, Zuberi et al. (2005) found that chemically aged soot aggregates collapsed to a compact morphology when water condensed and evaporated. The dehydrated soot particles, after cloud processing, exhibited less porous structures and reduced particle sizes. In another experiment with diesel soot, Huang et al. (1994) conducted up to three cycles of water condensation-evaporation on soot particles and observed restructuring. They suggested that their findings represent only the lower limit of soot compaction for atmospheric cloud processing. They also hypothesized that their previous observations of compact soot aggregates in the Grand Canyon may be due to cloud processing. In another study of ambient samples collected during smoke periods (ship and biomass burning emissions), Shingler et al. (2016) reported compaction of soot particles upon humidification. They found that compaction was higher at 95% compared to 85% RH, implying additional shrinkage at higher relative humidity. From laboratory experiments, Mikhailov et al. (2006) found drastic restructuring of hydrophilic soot aggregates from lacy to a globular-like morphology when the aggregates were exposed to saturated air (RH of 100%). A more recent cold cloud processing laboratory experiment also showed that lacy soot aggregates become compact after super-cooled water condensation, and even more, after ice nucleation (China et al., 2015a). The authors also found that compaction significantly affects the soot optical properties. In fact, light absorption and scattering change significantly when the soot particle undergoes a morphological transformation, ultimately affecting the soot radiative forcing (Radney et al., 2014;Liu et al., 2008;China et al., 2015a;China et al., 2015c;Zhang et al., 2017).

In our study, we analyze the morphology of soot from ambient samples processed in the atmosphere, as well as, laboratory samples collected from a cloud chamber. The purpose is to further test the hypothesis that cloud processing can indeed result in soot compaction, even without added coating material, besides water, and to quantify the effect. To generalize these results, we conclude our work by assessing the level of compaction for single soot particles collected at different locations and under different environmental conditions.

2.3 Methods

2.3.1 Ambient samples from San Pietro Capofiume

We collected 13 ambient samples at a rural supersite in San Pietro Capofiume (SPC), in the Po Valley of Italy, in November-December of 2015. The low temperature and high relative humidity typical of the fall season, result in stable atmospheric conditions favoring fog formation that interacts with anthropogenic pollutants present in high concentrations in the region (Fuzzi et al., 1992;Gilardoni et al., 2014;Bigi and Ghermandi, 2016). We drew ambient particles onto 13 mm diameter polycarbonate filter membranes (pore size of 0.1 μm, Whatman Inc., Chicago, Illinois, USA) and 3 mm diameter lacy formvar copper grids (300 mesh copper, Ted Pella, Inc., Redding, California, USA) by using an aspiration technique that is described elsewhere (China et al., 2014;China et al., 2015a). During sampling, ambient air was drawn through a $PM_{2.5}$ inlet using a diaphragm vacuum pump (Hargraves Technology Corporation, New Hampshire, USA). The flow rate varied between 0.12 and 0.26 lpm; however, it was nearly constant during each sampling period. Out of the 13 samples, we used five sample sets collected during different atmospheric conditions. Four sample sets were collected during fog conditions (we will refer to them as "foggy events"). Foggy events were individuated as periods of low solar irradiance (< 300 Wm^{-2}) and high liquid water content (LWC>0.08 gm^{-3}). The LWC was measured with a Particulate Volume Monitor PVM-100 (Gerber, 1991). As a reference, another sample set was collected during a sunny period ("sunny event"), as indicated by high solar irradiance (~ 400 Wm^{-2}, closer to the peak solar irradiance (~456 Wm^{-2}) during the campaign period of one month, see SI) and low LWC (0.01 gm^{-3}). Among the four foggy samples, we chose a sample during a dense foggy period in the morning that we refer to as "foggy morning event", with an LWC ~ 0.12 gm^{-3}. We compared the morphology of soot from this last sample with the soot collected during the "sunny event". Soot particles from the "foggy morning event" were expected to be processed by the fog, while the soot particles from the "sunny event" were expected to contain a larger fraction of soot not yet processed. Table 2-1 provides details on sampling times and conditions.

Table 2-1: Sampling conditions at the San Pietro Capofiume site in the Po Valley, Italy. The last two samples in the table were used for the detailed morphological analysis of soot.

S. No.	Event	Collection date and time	Sampling flow rate (lpm)	Initial liquid water content gm^{-3} (LWC_i)	Final liquid water content gm^{-3} (LWC_f)
1.	Dense fog	12/02/2015 9:40- 10:10	0.17	0.15	0.10
2.	Dissipating fog	12/02/2015 11:50-12:20	0.17	0.04	0.01
3.	Forming fog	12/02/2015 18:43-19:00	0.26	0.05	0.28
4.	Dense morning fog (Foggy morning)	12/04/2015 9:15-9:45	0.17	0.12	0.11
5.	Sunny	11/30/2015 10:40-10:55	0.13	0.01	0.01

We used all five samples to study the soot mixing state (see section 2.3.3.1). Out of these sample sets, two samples ("sunny event" and "foggy morning event") were used to study the soot compaction. The sulfur/carbon atomic ratio for coated soot in those two samples was determined by using the energy-dispersive x-ray spectroscopy (EDS). Only lacy TEM

grids were used for the EDS to avoid the background carbon signal from the membrane. A total of 204 and 426 internally mixed soot particles were analyzed with EDS for the sunny event and foggy morning event samples, respectively.

In addition, two instruments were used to measure the mass concentration of aerosol. A High Resolution Time of Flight Aerosol Mass Spectrometer (HR-ToF-AMS, Aerodyne Research Inc.) was used to measure the mass concentration of non-refractory components in the ambient samples (in μgm^{-3}). The mass concentration of soot in the ambient samples was measured with a 7-wavelength Aethalometer (Magee, AE31). A sampling interval of 5 minutes was set for both instruments.

2.3.2 Laboratory sample collection from the π-chamber

We We performed experiments in the laboratory (on January 30th, 2017) to study the soot compaction process under controlled conditions. To subject the soot particles to cloud processing, we utilized the turbulent cloud chamber at Michigan Technological University (USA), referred to hereafter as the π-chamber. A detailed discussion of the π-chamber is provided by Chang et al. (2016). In the π-chamber, clouds are formed by expansion or by mixing. In the mixing mode, a long-lasting cloud is formed by imposing a temperature gradient between the top and bottom surfaces (radiant plates), while maintaining the two surfaces saturated with respect to water. For the experiments discussed here, we generated clouds in the mixing mode, using a temperature gradient of 19 K between the warmer bottom plate and the colder top plate to drive convection and form a mixing cloud, a process that is described in detail elsewhere (Chandrakar et al., 2016). Soot particles were drawn from a kerosene flame using an eductor pump (AIR-VAC, model: AVR093M) and compressed clean air, and injected into the π-Chamber. We then formed a mixing cloud by using the soot particles as cloud condensation nuclei. The LWC of the cloud chamber during the experiment was ~0.085 gm^{-3} (measured using a phase doppler interferometer, Dantec dynamics). We used a pumped counterflow virtual impactor (PCVI-8100, Brechtel Mfg.) to collect only the residual soot particles. In the PCVI, air pumped in the direction

opposite (counterflow) to that of the input flow drives smaller interstitial aerosols away, allowing only larger particles (mainly droplets) to pass through the inlet, due to their inertia (Boulter et al., 2006;Kulkarni et al., 2011). In other words, only particles with enough mass can overcome the counterflow, and pass through the sampling orifice. Because dry air is used in the counterflow, the droplets evaporate, leaving behind the residual soot particles (RS). The PCVI was run to achieve a size cut of ~4.5 μm with an efficiency of < 30%. We used a separate outlet (a quarter inch conductive tube ~1 m long) from the chamber to collect mostly interstitial soot particles (IS) at a flow rate of 0.5 lpm. The conducting tube was connected to a quarter inch horizontal stainless-steel tube of ~1.5 m inside the chamber. Using the phase doppler interferometer (Dantec Dynamics) we measured a mean droplet diameter of 20 μm; at this size droplets travel <20 cm through the horizontal steel tube before impacting on the walls ensuring that we collected only interstitial soot particles. Before sampling the particles, both the RS and IS were passed through a diffusion dryer to further remove moisture. A schematic showing the collection of both IS and RS samples is shown in Fig. 2-2.

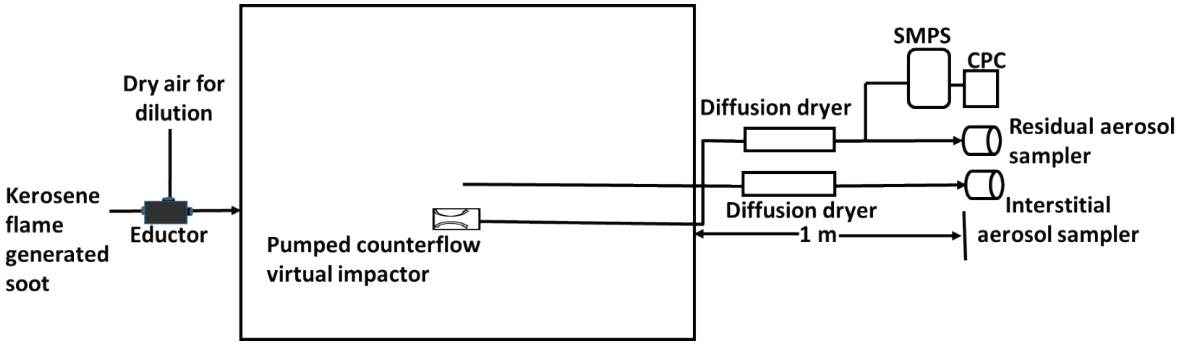

Figure 2-2. Soot aerosol sampling set-up in the π-chamber.

Comparing the RS and IS samples allowed us to investigate and quantify the difference between the morphology of soot that took part in cloud processing vs. those that did not. We measured the mobility size distribution of soot particles using a Scanning Mobility Particle Sizer (SMPS- TSI-3772). Both IS as well as RS were collected on 13 mm diameter nuclepore polycarbonate membranes, having a pore size of 0.1 μm (Whatman Inc.,

Chicago, Illinois, USA) with a flow rate of 0.4 lpm (Hargraves Technology Corporation, New Hampshire, USA).

2.3.3 Single particle analysis

The membranes were coated with 1.5 nm (±10%) thick layer of Au/Pd alloy in a sputter coater (Cressington 208HR) to reduce charging effects. We then imaged individual particles with a Hitachi S-4700 field emission scanning electron microscope (FE-SEM) at a magnification of 60-100 kX, an accelerating voltage of 1 kV, and a working distance of 4 mm for single particle analysis and particle classification. We also took transmission electron microscopy (TEM) images on the copper grids for two samples ('sunny event' and 'foggy morning event' samples) using an environmental transmission electron microscope (E-TEM Titan, FEI) operated at 300 kV. The TEM images were used for energy dispersive X-ray spectroscopy and for particle classification. We used the FE-SEM and TEM images to calculate several morphological parameters with the freely available image processing software ImageJ (Schneider et al., 2012). During image analysis, we used a Gaussian blur filter for smoothing the edges of the binarized images.

2.3.3.1 Morphology and mixing state of soot

To To quantify the structural changes that soot underwent during cloud processing and assess the degree of compaction, we investigated several morphological parameters. These include roundness, convexity, aspect ratio (AR) and area equivalent diameter (D_{Aeq}). Next, we provide a succinct description of these parameters, additional details and the limitations of image processing and analysis can be found elsewhere (China et al., 2014;China et al., 2013;Bhandari et al., 2017). Roundness is the ratio of the projected area of an aggregate (A_p) to the area of a circle having a diameter of L_{max}, and is a measure of the particle geometry and topology. Convexity is the ratio of A_p to the area of the convex hull polygon inscribing the aggregate and is a topological property of the particle. AR is the ratio of L_{max} and the width of the projected aggregate (W) orthogonal to L_{max} , and is a measure of the elongation of the particle. D_{Aeq} is the diameter of a spherical particle with an area

equivalent to A_p and provides a quantitative measure of the particle size. The three parameters *AR*, convexity, and roundness incorporate different and somewhat complementary information. For example, a spherical particle has projected convexity, roundness and *AR* values each equal to unity, while a rectangular parallelepiped laying on its long side has a projected convexity of unity, but its roundness is lower than one and its *AR* is larger than one. Specifically, lacy soot particles with an open structure are expected to show lower convexity and roundness, and higher *AR* values, with respect to compact soot particles. This is true even if the particles (compact or lacy) have the same mass and identical monomer diameter. When a soot particle compacts instead we expect the D_{Aeq} to decrease. An example of an SEM image of a soot particle and a schematic representation of the *AR*, and convexity and roundness calculations from the respective binary image are shown in Figs. 2-3 a, b, and c, respectively.

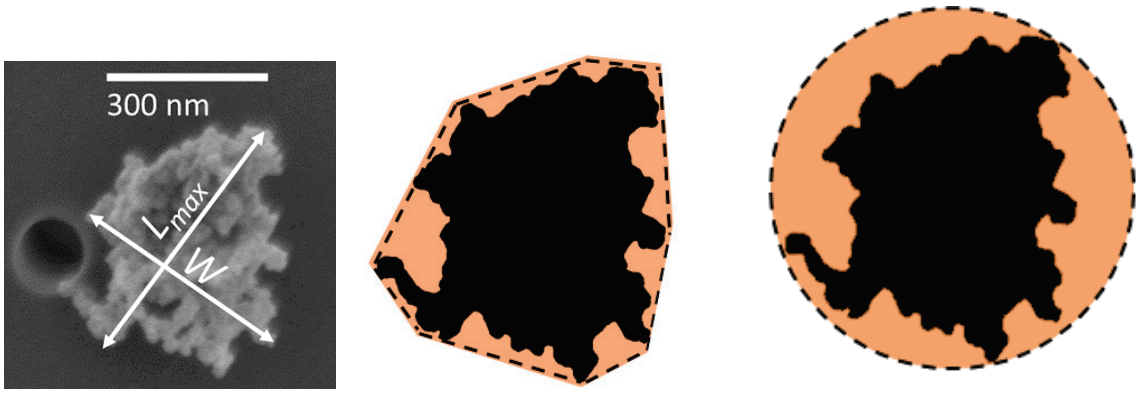

AR =1.28 Convexity = 0.79 Roundness = 0.59

(a) (b) (c)

Figure 2-3a) Example of SEM image of a soot particle collected in the laboratory on January 30, 2017, showing how we calculate the AR from the maximum length and maximum width of the particle (orthogonal to each other). The black circle in the middle left side of the image is a pore in the substrate. **b**) Schematic representation of the convexity calculation for the same soot particle shown in a). **c**) Schematic representation of the roundness calculation for the same soot particle shown in a). The pink shades in b) and c)

represent the equivalent area for the convex hull and the inscribing circle, respectively. The binary image of the soot particle is in black.

To quantify the morphology of soot, we also calculated the fractal dimension (D_f) of soot particles. However, D_f values are more difficult to calculate and the method used to calculate the D_f requires several soot particles, it becomes more difficult and more uncertain for ambient particles and therefore, the results are discussed in the SI.

Often, ambient soot particles are coated by other material and some are so thickly coated that the monomers are not clearly distinguishable, this can bias the calculation of the morphological parameters. Therefore, we first classified the ambient soot particles into four categories based on a visual inspection of the coating thickness: C0, C1, C2, and C3, as described by Girotto Giulia (2015). In brief, a bare or thinly coated soot particle, in which all the monomers are clearly visible, is classified as C0. In C1, the soot particle has some of the monomers covered by a thin coating, and in category C2, the soot particle has some monomers covered by thick coating; finally, in C3, most of the monomers are completely covered by the coating material and are barely distinguishable (Fig. 2-4a). In some cases, the soot particles appear to be attached to, or partially engulfed by, other particles. Such partially encapsulated/surface attached soot is classified in an additional separate category, PE (Fig. 2-4b). For example, as shown in Fig. 2-4b), the soot is thickly coated (C2), and also surface attached with another particle (PE-C2).

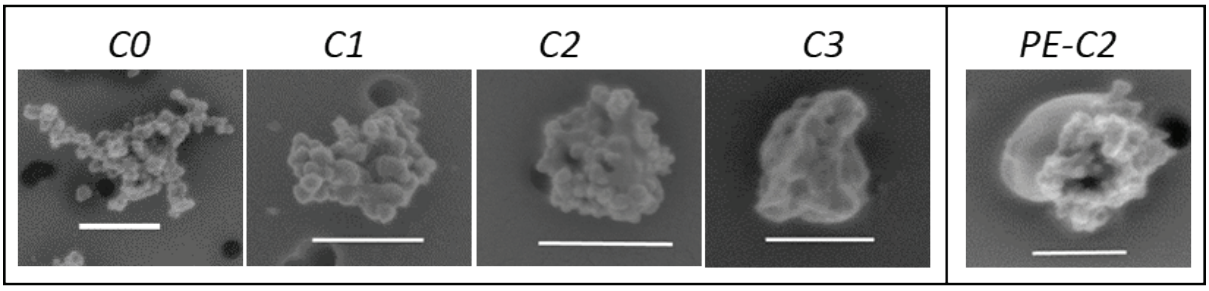

(a) (b)

Figure 2-4a) Soot particles with different degrees of coating: category-(C0-C3). **b)** Soot particle of category PE-C2. The scale bar on each micrograph corresponds to 300 nm.

We note that this soot classification is based on a visual evaluation from the SEM micrographs, and therefore, it presents some subjectivity and some potential bias. For example, a heavily coated soot that would fall in category C3 might be excluded from the soot classification when none of the monomers in the SEM image were discernible. Also, the vacuum in the electron microscope chamber might result in evaporation of some of the coating material. However, these biases are not a real concern here, as we will focus on particles in the C0 and C1 category only. Soot particles collected in the laboratory were freshly emitted and mostly uncoated, and therefore, were considered all to be in the C0 category.

2.3.3.2 Uncertainties in the image processing

Bhandari et al. (2017) provided a discussion of the uncertainties associated with the calculation of the morphological parameters determined from the SEM images. In addition to the statistical error, there are potential errors in the parameters associated with image acquisition and image processing. Bhandari et al. (2017) estimated the errors in convexity and roundness to be 3.9 % and 4.4 %, respectively. Similarly, the errors in L_{max}, W and d_p were estimated to be 1.5 %, 1.8 % and 14%, respectively. Using the errors in L_{max} and W we calculate a 1.9% uncertainty in the AR. The uncertainty in D_{Aeq} was 3.2%. Unless differently stated, here forth, we will use the mean ± the total error calculated by adding all the errors (statistical error and errors associated with image acquisition and image processing) in quadrature.

2.4 Results

2.4.1 Mixing state of the San Pietro Capofiume soot particles

As discussed above, for the SPC ambient soot, we visually classified the mixing state of more than 840 individual particles from SEM images from five samples. We also classified

348 soot particles from TEM images of two additional samples collected during the sunny and the foggy morning events.

Figure 2-5 shows the classification of soot particles (from both SEM and TEM images) from different events (Table 2-1).

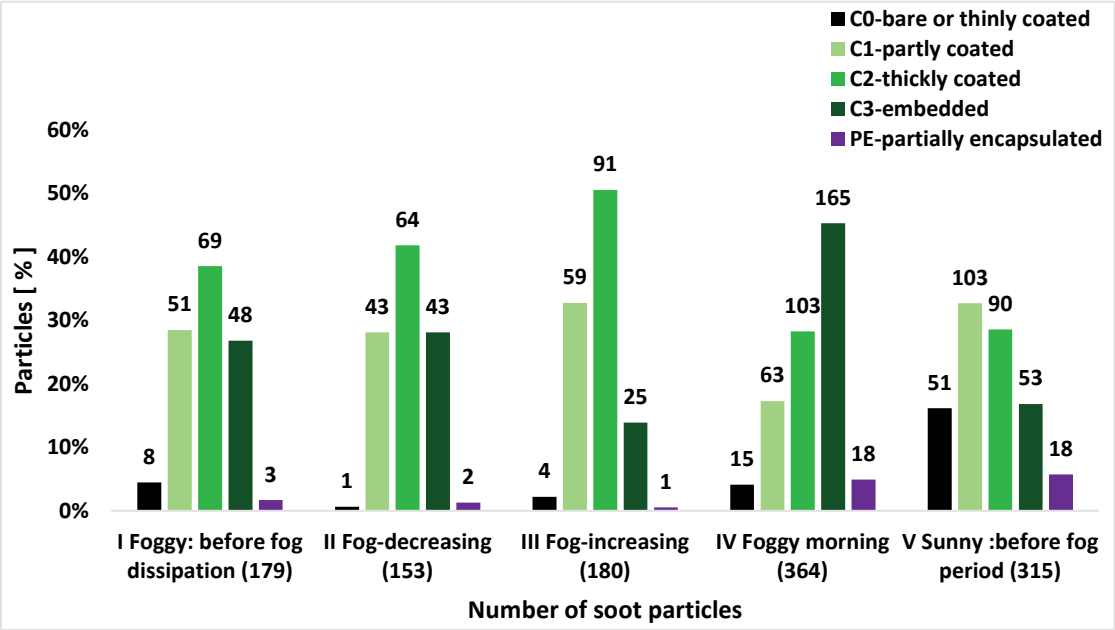

Figure 2-5. The contribution of soot particles for each category during different events. The total number of particles in each category is reported above each bar. The numerals in the bracket represent the number of soot particles for each sample.

We found that most of the soot particles were partly or thickly coated (soot of category C1 or C2). As mentioned before, ambient soot can acquire a coating during aging. A substantial fraction of soot in all samples was embedded. These fractions suggest that soot was aged and mixed with other materials such as organics or sulfate, common in polluted regions (Adachi et al., 2010;Peng et al., 2016). The aerosol mass spectrometer data showed more than 30% organics and ~ 5% sulfate in all five samples. Elemental analysis of soot particles from the sunny and foggy morning events showed an appreciable abundance of sulfur in both samples (Fig. 2-6). On average 53% of all the soot particles analyzed

exhibited S/C >0.001 for the sunny event while the number fraction was 48% for the foggy morning event. The average (± S.D.) S/C values were 0.010 (0.006) and 0.009 (0.005) for the sunny and foggy morning events, respectively. The presence of sulfur in the soot suggests that these particles were likely to participate in cloud activation (Zhang et al., 2017). In all events, the number fraction of soot in category PE was small (< 5%) suggesting that coagulation processes had only a minor role in determining the mixing state of soot.

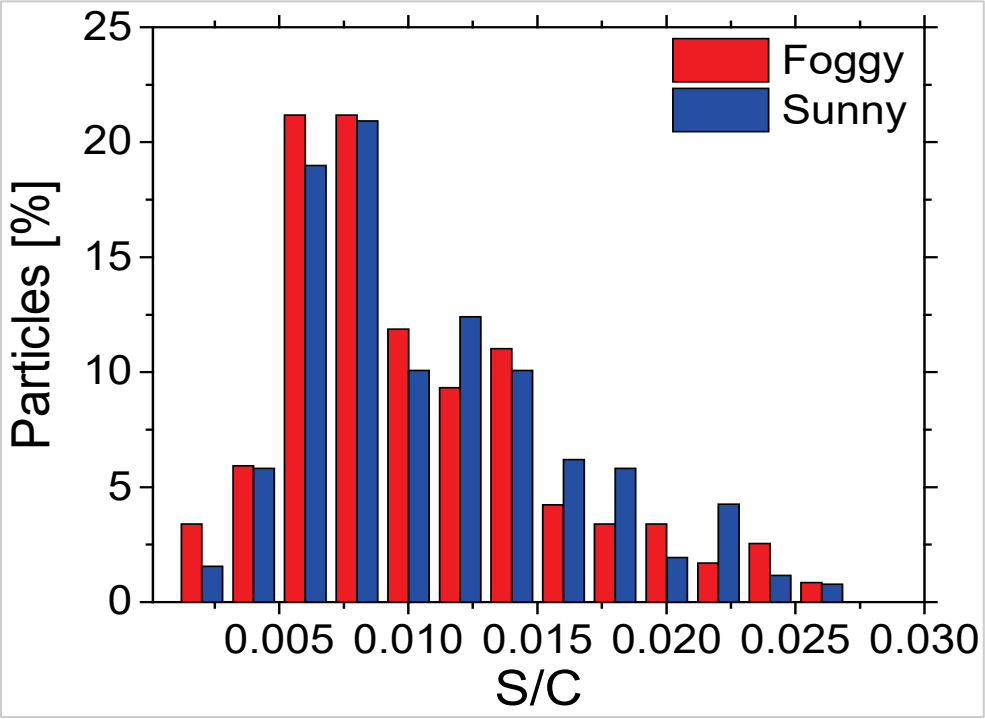

Figure 2-6. Ratio of sulphur and carbon in coated soot for the samples from the sunny and the foggy morning events.

2.4.2 Morphology of ambient soot particles

During the image analysis, we noticed many compact soot particles with and without an appreciable amount of coating material. Minimally coated, but compact soot particles have been found in the atmosphere previously; for example, China et al. (2015c) found 26% of compact soot particles in the free troposphere over the North Atlantic, with a minimal

amount of coating. They hypothesized that the presence of such compact soot might have been the result of cloud processing. Because we quantify compaction with the morphological parameters discussed earlier in section 2.3.3.1, and because coating might affect the results of the 2D projected image, we focus here only on those particles with a small amount of coating (categories C0 and C1). This choice maximizes the chances of quantifying soot compaction due to cloud processing and minimizes the potential contribution to compaction by coating, other than water. However, this approach excludes those soot particles that became compact through cloud processing and were coated later. As mentioned earlier, we compared the soot from the sunny event to that from the foggy morning, to find evidence of cloud processing in their morphologies. A total of 109 individual soot particles were imaged and analyzed for the sunny event and 144 soot particles were imaged and analyzed for the foggy morning event. The mean, standard deviation (S.D.), and standard error (S.E.) values for different morphological parameters are summarized in Table S1. The total error for each parameter (as discussed in section 2.3.3.2) is reported in the square brackets in Table S1.

From Table S1 it can be noticed that the mean values for convexity and roundness are lower for soot particles collected during the sunny event compared to those collected during the foggy event (Fig. 2-7a and b, respectively). A bootstrap method, in which frequency distributions are constructed from the raw data with 100,000 resampling with replacement (Wilks, 2011), was used to calculate the mean and S.D. for each bin in the distributions shown in Fig. 2-7.

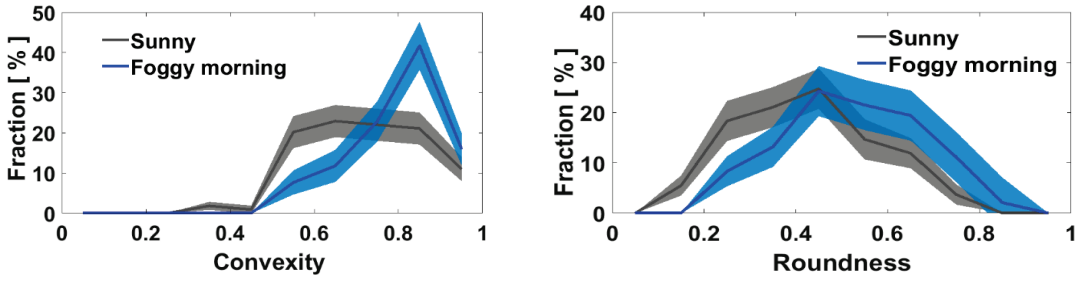

(a) *(b)*

Figure 2-7. Distributions of **(a)** convexity and **(b)** roundness of soot particles of category C0 and C1. The colored shadings represent plus and minus one standard deviation of the 100,000 bootstrapped distributions within each bin (see main text).

After cloud processing, the convexity and the roundness distributions both appear to shift toward larger values. Also, the *AR* and D_{Aeq} distribution of the soot particles shifted to lower values during the foggy morning event with respect to the sunny event (see S1a and S2a in supplementary for *AR* and D_{Aeq} distribution plots). While the size of monomers (Table S1) in the soot aggregates did not show significant change. These findings support the hypothesis that soot compaction can arise from cloud processing of ambient soot.

2.4.3 Morphology of soot particles from the π-chamber

As mentioned in the method section 2.3.2, we simulated the cloud processing of soot using the π-Chamber to further investigate the effect of cloud processing on the soot morphology in laboratory conditions. Soot particles sampled from the π-Chamber showed clear changes in the morphology between the IS and RS particles. Most of the soot particles sampled through the PCVI (i.e., RS) showed a more compact morphology (Fig. 2-8).

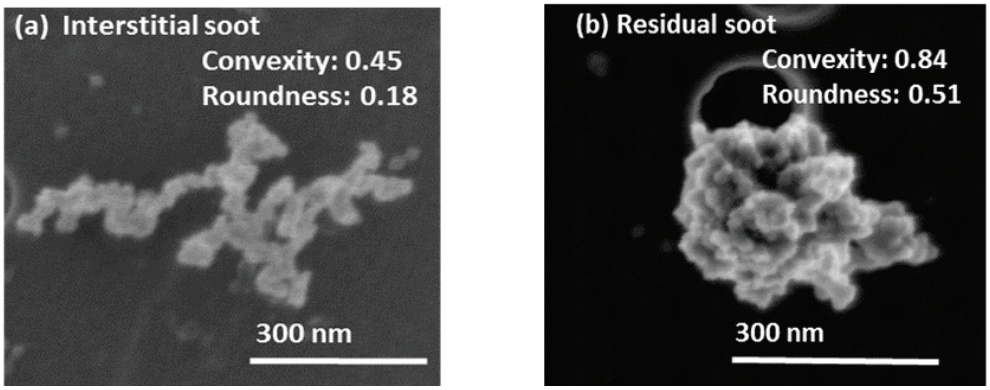

Figure 2-8. SEM images of soot particles collected on polycarbonate membrane from the π-Chamber on January 30, 2017 and imaged at an accelerating voltage of 1 kV, an emission current of 10 μA and a working distance of 4 mm for: **a)** an interstitial soot particle (magnification of 80 kX), and **b)** a residual soot particle (magnification of 100 kX). The

dark spot in (b) is a pore in the filter. The convexity and roundness of each particle are reported as well.

Convexity and roundness were significantly higher for the RS compared to the IS samples, indicating a substantial compaction of soot particles by cloud processing, as shown in the distribution plots in Fig. 2-9.

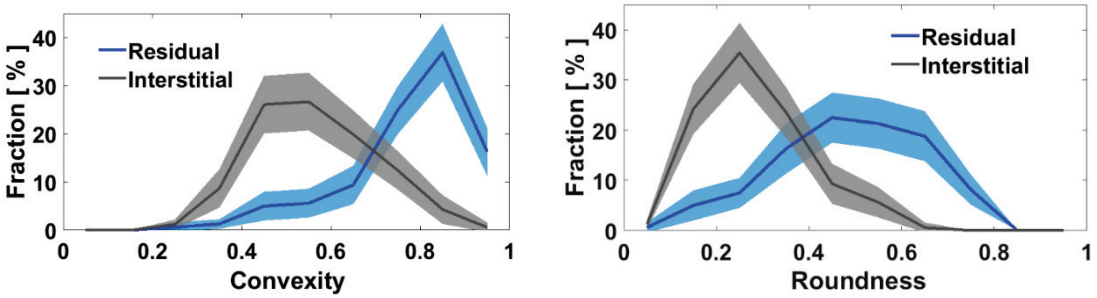

Figure 2-9. Distribution of: **(a)** convexity, and **(b)** roundness for residual and interstitial soot particles. The shaded colored bands represent one S.D.

The findings are substantiated by a decrease in *AR* and D_{Aeq}. for RS as clearly visible in the distribution plots shown in the SI (Figs. S1b and S2b).

The large range in D_{Aeq} is because the soot particles generated during the experiments were injected into the chamber without size selection. However, no significant change in the size of monomers was detected.

We should note that the size of the monomers for the soot particles from the π-chamber was smaller than that of ambient soot. The size of the monomers in soot aggregates depends on various factors like flaming condition, fuel type etc. (Bambha et al., 2013;Bond et al., 2004), but they also depend on atmospheric aging processes**.** The soot particles sampled in the π-chamber were fresh (collected within an hour of emission), while the particles sampled at the SPC site were mostly aged, as discussed earlier.

2.5 Discussion and conclusion

Ambient Ambient soot particles showed a range of mixing states and morphologies. The fraction of soot particles with minimal coating was higher on the sunny than the foggy events. However, most of the soot particles were coated for all samples. The AMS data showed a large fraction (29-46%) of organics, along with nitrate (17-42%), ammonium (7-15%) and sulfate (4-7%) that might have contributed to the coating on the soot particles and potentially have contributed to the soot hydrophilicity. Also, only a minor fraction of soot particles (< 6%) were partially encapsulated/attached with other materials, implying that coagulation was not a significant process affecting the soot mixing, similar to what has been found in other studies (China et al., 2015c;China et al., 2014). Our results show that soot particles become compact because of cloud processing. Both roundness and convexity were higher and significantly different for the soot particles from the foggy morning event compared to the sunny event. Consistently with these findings, the AR and D_{Aeq} were significantly lower in the foggy morning sample.

In the cloud chamber experiments, the soot roundness and convexity were both significantly higher for the RS compared to the IS, whereas the AR and D_{Aeq} were significantly smaller, demonstrating the soot compaction by cloud processing even in absence of added coating material. The π-chamber samples showed more evident changes in morphology with respect to the ambient samples. This observation is consistent with the fact that the ambient samples are a complex mixture of soot of different degrees of aging and processing, compared to the chamber experiments. In addition, a PCVI was not available during the ambient sampling. During the sunny event, pre-existing soot might already have been cloud processed in a previous fog event. It is therefore reasonable, that the roundness and the convexity of the ambient soot for the sunny event were higher compared to the IS collected from the π-chamber. It is interesting to note, however, that the roundness and convexity distribution plots for the foggy morning event (blue curves in Fig. 2-7) and those for the RS from the cloud chamber (blue curves in Fig. 2-9) are quite similar. This suggests that the right side of these convexity and roundness distributions

might represent upper limits for these parameters in warm cloud conditions and short processing times. The mean values of convexity and roundness are comparable also to the mean values of convexity (0.75) and roundness (0.45) observed by China et al. (2015a) in diesel soot liquid water residuals. The values presented here, are instead lower than the values obtained for ice crystal residuals (convexity =0.83 and roundness = 0.55) by China et al. (2015a), suggesting that ice nucleation might indeed further compact soot. These observations might explain why the mean values of roundness and convexity for our cloud processed soot (from the cloud chamber and SPC ambient samples) are slightly lower than the convexity and roundness of soot samples retrieved from the marine free troposphere after the long-range transport (China et al., 2015c). In their study, the particles were transported in the free troposphere at heights that might have resulted in freezing for at least some of the soot, resulting in more compact overall soot population. In addition, the soot analyzed in their study was transported for several days in the atmosphere, allowing for multiple cycles of cloud processing. Therefore, both cloud processing type (cold vs. warm) and transport time probably play a role in determining the upper limit of soot compaction in the atmosphere.

To further put these results in a broader context, we compile the probability distribution for convexity with a box plot (distribution plot for roundness is shown in SI in Fig. S8) for ambient soot particles collected by our group from different global locations in Fig. 2-10. On each plot, the bar represents the probability distribution function of convexity distribution and the vertical white line on each box plot represents the median and the grey diamond represents the confidence interval for the mean of the distribution. It is to be noted that the roundness and convexity plots were only from thinly coated or partly coated soot as for the data shown in the previous sections. In Table S3, we present the mean values of roundness and convexity for these ambient soot samples along with some laboratory samples and their collection date. Freshly emitted ambient soot particles collected in Bhaktapur (Nepal) and West Bengal (India) had lower values for roundness and convexity compared to other soot samples. Samples in Bhaktapur were collected near roads around the brick kiln sites consisted of fresh emission (few seconds) from kilns and on-road

vehicles. Samples collected from a rural site in West Bengal, India showed slightly higher values of roundness and convexity than the samples from Bhaktapur but are lower than other samples suggesting slightly aged samples (few hours). Ambient soot particles, collected during the 2010 Carbonaceous Aerosol and Radiative Effects Study (CARES) in Sacramento showed slightly higher values than the rural site at West Bengal. CARES samples collected from the foothills of the Sierra Nevada Mountains in Cool showed higher values of roundness and convexity than at Sacramento, consistent with the longer aging times (in the order of a day). The roundness and convexity of ambient soot from the T0 site in Mexico City during the Megacity Initiative: Local and Global Research Observations (MILAGRO) campaign with an aging time like that during CARES showed comparable values to those of CARES. Soot compaction with aging was also observed for the two fire events in our study. Both the roundness and convexity are higher for the more-aged smoke plume from Whitewater-Baldy complex fire collected at Las Alamos (Las Alamos National Laboratory) compared to the Las Conchas fire. Surprisingly, the fresh samples collected at a road site from Ann Arbor (China et al., 2014) shows comparable values of roundness and convexity to the samples collected during the MILAGRO and CARES campaign. It might be due to the compact soot particles collected in the samples when there were more heavy-duty vehicles on road. (China et al., 2014) have found that D_f of soot got increased when more heavy-duty vehicles plighted on the road. Also, the samples might have pre-existing soot particles that had been transported to the sampling sites from other nearby highways and surrounding. For the ambient soot collected in Detling, the UK during the 2012 ClearfLo (clean air for London) campaign (Liu et al., 2015), the values were higher suggesting somewhat longer aging times for the airmass originating from London outskirts and Benelux region to arrive Detling. The higher values of roundness and convexity of the soot particles in Detling compared to those of Mexico City and California (Sacramento and Cool) might also be due to the moist weather conditions (winter) in the UK compared to the dry atmosphere of Mexico City and ??California. The highest values (mean) of roundness (0.58) and convexity (0.84), also evident from the distribution plots were found for soot particles collected in the Pico mountain at Azores (Portugal), with probable aging

times of several days, due to the long-range transport from the source and the high likelihood of multiple cloud processing, possibly including ice formation as discussed earlier (China et al., 2015b). Roundness and convexity values seem to clearly increase as the aging time becomes longer. A separate laboratory experiment in the π-chamber at Michigan Tech showed that the degree of compaction is higher for turbulent mixing cloud (multiple cloud processing of soot) compared to the single cloud expansion experiment suggesting that soot particles at Pico mountain might have undergone multiple cloud processing (Fig. S7). In addition, highly compact soot particles retrieved during the long-range transport might have been processed in ice clouds before they are entrained to the free troposphere. In laboratory experiments at Pacific Northwest National Laboratory, China et al. (2015a) found that the cloud processed ice crystal residuals (soot particles) underwent severe compaction corroborating the hypothesis of soot compaction in Pico mountain, possibly by the cloud processing in ice-clouds.

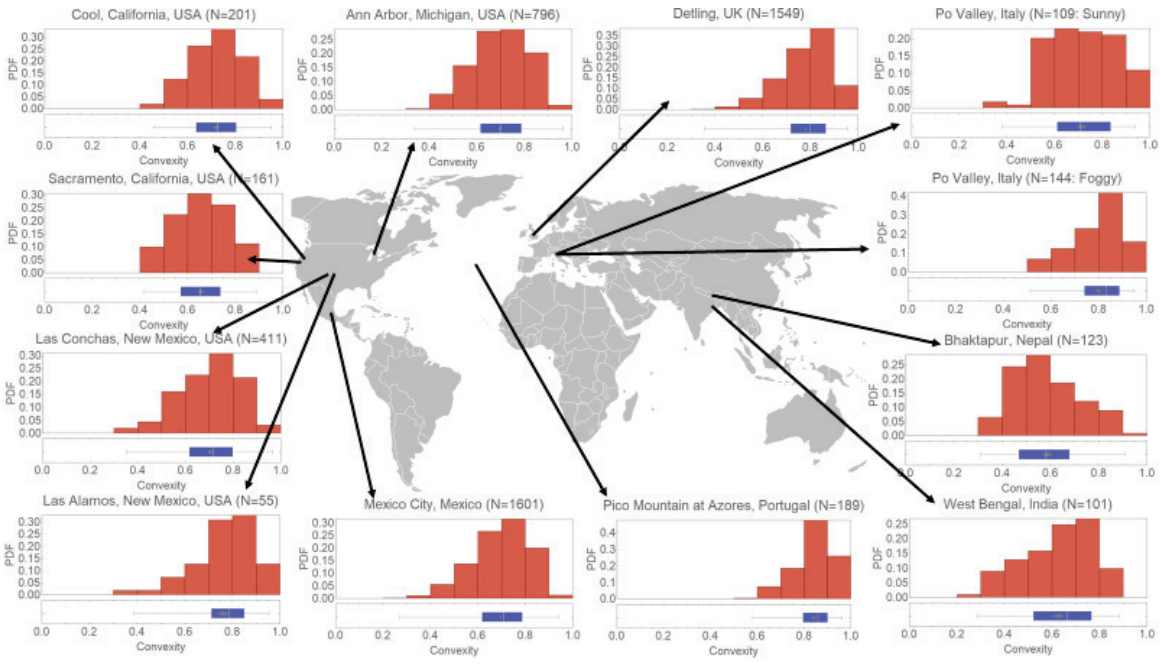

Figure 2-10. Histogram and box plot for convexity of thinly coated soot particles from different locations. On each box plot, the vertical white line represents the median and the grey diamond represents the mean confidence interval for each distribution. For each

distribution, N in the bracket is the number of soot particles analyzed and PDF on the y-axis is the probability distribution of particles for each bin as a function of convexity.

Table 2-2. Mean value of roundness and convexity of ambient soot particles (soot category C0 and C1) from different locations. The last three samples in the table are from the laboratory sources.

S. No.	Roundness	Convexity	Soot source	# particles analyzed	Literature
1.	0.47	0.78	Plumes from London and Benelux collected at Detling, the UK (January 31st Benelux, February 2-3, London, 2012)	1549	Girotto (thesis 2015)
2.	0.45	0.76	Whitewater-Baldy Complex Fire, New Mexico (May 2012)	55	Girotto (thesis 2015)
3.	0.42	0.72	CARES campaign, Cool (June 2010)	201	This study
4.	0.38	0.65	CARES campaign, Sacramento (June 2010)	161	This study
5.	0.41	0.70	Mexico City, Mexico (March 2006)	1601	China (thesis 2014)
6.	0.32	0.59	Bhaktapur, Nepal (March 2017) (fresh emission)	123	This study
7.	0.36	0.63	West Bengal, India () (fresh emission)	101	This study
8.	0.58	0.84	Pico Mountain at the Azores, Portugal (July 2012) (> a week aged)	189	(China et al., 2015b)
9.	0.40	0.70	Ann Arbor, Michigan (July-August 2010) (fresh soot)	796	(China et al., 2014)
10.	0.41	0.70	Los Conchas Fire, New Mexico (July 2011) (1-2 hours aged)	411	(China et al., 2013)
11.	0.43	0.71	Po Valley, Italy, sunny day (December 2015)	109	This study
12.	0.52	0.80	Po Valley, Italy, foggy morning (December 2015)	144	This study
13.	0.29	0.56	Michigan Tech Cloud Chamber π at Houghton, Michigan (January 2017) (interstitial soot-few minutes aged)	161	This study
14.	0.48	0.78	Michigan Tech Cloud Chamber π at Houghton, Michigan (January 2017) (residual soot-few minutes aged)	160	This study
15.	0.55	0.83	Pacific Northwest National Laboratory, Richland, Washington (November 2013-January 2014) (Ice crystal residual from diesel soot)	241	(China et al., 2015a)

These results can have implications on how we should model the properties of soot particles transported in the atmosphere. Several lines of evidence have shown that the optical properties of soot change when the soot becomes compact, with the effect of compaction being more pronounced for light scattering (Radney et al., 2014;Liu and Mishchenko, 2005;China et al., 2015a). In a recent ice nucleation study, using soot from different fuel sources, Mahrt et al. (2018) found that the ice nucleation abilities of soot are also affected by the availability of mesopores. A lower number of mesopores in compact soot compared to lacy soot can make it less effective for ice nucleation. Additionally, compact soot has a higher effective density than lacy soot (Rissler et al., 2014), which can have an effect on dry deposition and electrical mobility. Finally, studies have shown that the toxicity of inhaled aerosol, including soot particles, in lungs increases with the surface area of the particles (Oberdörster, 2000;Schmid and Stoeger, 2016;Stoeger et al., 2006). In a recent study in Japan, Kiriya et al. (2017) showed that fresh soot concentrations correlated with aerosol surface area measurements, with the correlation weakening for aged soot. In addition, the deposition of fiber-like particles, such as fresh soot in the lungs, is enhanced, for the same mass, due to higher drag (Asbach et al., 2016;Scheckman and McMurry, 2011).

2.6 References

1. Adachi, K., and Buseck, P.: Internally mixed soot, sulfates, and organic matter in aerosol particles from Mexico City, Atmospheric Chemistry and Physics, 8, 6469-6481, 2008.
2. Adachi, K., Chung, S. H., and Buseck, P. R.: Shapes of soot aerosol particles and implications for their effects on climate, Journal of Geophysical Research: Atmospheres, 115, 2010.
3. Bambha, R., Dansson, M. A., Schrader, P. E., and Michelsen, H. A.: Effects of volatile coatings on the morphology and optical detection of combustion-generated black carbon particles, Sandia National Laboratories (SNL-CA), Livermore, CA (United States), 2013.
4. Bhandari, J., China, S., Onasch, T., Wolff, L., Lambe, A., Davidovits, P., Cross, E., Ahern, A., Olfert, J., Dubey, M., and Mazzoleni, C.: Effect of Thermodenuding on the Structure of Nascent Flame Soot Aggregates, Atmosphere, 8, 166, 2017.
5. Bigi, A., and Ghermandi, G.: Trends and variability of atmospheric PM 2.5 and PM 10–2.5 concentration in the Po Valley, Italy, Atmospheric Chemistry and Physics, 16, 15777-15788, 2016.
6. Bond, T. C., Streets, D. G., Yarber, K. F., Nelson, S. M., Woo, J. H., and Klimont, Z.: A technology-based global inventory of black and organic carbon emissions from combustion, Journal of Geophysical Research: Atmospheres, 109, 2004.
7. Bond, T. C., Doherty, S. J., Fahey, D., Forster, P., Berntsen, T., DeAngelo, B., Flanner, M., Ghan, S., Kärcher, B., and Koch, D.: Bounding the role of black carbon in the climate system: A scientific assessment, Journal of Geophysical Research: Atmospheres, 118, 5380-5552, 2013.
8. Boulter, J., Cziczo, D., Middlebrook, A., Thomson, D., and Murphy, D.: Design and performance of a pumped counterflow virtual impactor, Aerosol science and technology, 40, 969-976, 2006.
9. Brasil, A., Farias, T. L., and Carvalho, M.: A recipe for image characterization of fractal-like aggregates, Journal of Aerosol Science, 30, 1379-1389, 1999.
10. Chandrakar, K. K., Cantrell, W., Chang, K., Ciochetto, D., Niedermeier, D., Ovchinnikov, M., Shaw, R. A., and Yang, F.: Aerosol indirect effect from turbulence-induced broadening of cloud-droplet size distributions, Proceedings of the National Academy of Sciences, 113, 14243-14248, 2016.
11. Chang, K., Bench, J., Brege, M., Cantrell, W., Chandrakar, K., Ciochetto, D., Mazzoleni, C., Mazzoleni, L., Niedermeier, D., and Shaw, R.: A Laboratory Facility to Study Gas–Aerosol–Cloud Interactions in a Turbulent Environment: The

Π Chamber, Bulletin of the American Meteorological Society, 97, 2343-2358, 2016.

12. China, S., Mazzoleni, C., Gorkowski, K., Aiken, A. C., and Dubey, M. K.: Morphology and mixing state of individual freshly emitted wildfire carbonaceous particles, Nature communications, 4, 2013.

13. China, S., Salvadori, N., and Mazzoleni, C.: Effect of traffic and driving characteristics on morphology of atmospheric soot particles at freeway on-ramps, Environmental science & technology, 48, 3128-3135, 2014.

14. China, S., Kulkarni, G., Scarnato, B. V., Sharma, N., Pekour, M., Shilling, J. E., Wilson, J., Zelenyuk, A., Chand, D., and Liu, S.: Morphology of diesel soot residuals from supercooled water droplets and ice crystals: implications for optical properties, Environmental Research Letters, 10, 114010, 2015a.

15. China, S., Scarnato, B., Owen, R. C., Zhang, B., Ampadu, M. T., Kumar, S., Dzepina, K., Dziobak, M. P., Fialho, P., and Perlinger, J. A.: Morphology and mixing state of aged soot particles at a remote marine free troposphere site: Implications for optical properties, Geophysical Research Letters, 42, 1243-1250, 2015b.

16. Colbeck, I., Appleby, L., Hardman, E., and Harrison, R. M.: The optical properties and morphology of cloud-processed carbonaceous smoke, Journal of Aerosol Science, 21, 527-538, 1990.

17. Cross, E. S., Onasch, T. B., Ahern, A., Wrobel, W., Slowik, J. G., Olfert, J., Lack, D. A., Massoli, P., Cappa, C. D., and Schwarz, J. P.: Soot particle studies—instrument inter-comparison—project overview, Aerosol Science and Technology, 44, 592-611, 2010.

18. DeCarlo, P. F., Slowik, J. G., Worsnop, D. R., Davidovits, P., and Jimenez, J. L.: Particle Morphology and Density Characterization by Combined Mobility and Aerodynamic Diameter Measurements. Part 1: Theory, Aerosol Science and Technology, 38, 1185-1205, 10.1080/027868290903907, 2004.

19. Decesari, S., Facchini, M., Matta, E., Mircea, M., Fuzzi, S., Chughtai, A., and Smith, D.: Water soluble organic compounds formed by oxidation of soot, Atmospheric Environment, 36, 1827-1832, 2002.

20. Ebert, M., Inerle-Hof, M., and Weinbruch, S.: Environmental scanning electron microscopy as a new technique to determine the hygroscopic behaviour of individual aerosol particles, Atmospheric Environment, 36, 5909-5916, 2002.

21. Fenimore, C. P., and Jones, G. W.: Oxidation of soot by hydroxyl radicals, The Journal of physical chemistry, 71, 593-597, 1967.

22. Fuzzi, S., Facchini, M., Orsi, G., Lind, J., Wobrock, W., Kessel, M., Maser, R., Jaeschke, W., Enderle, K., and Arends, B.: The Po valley fog experiment 1989, Tellus B, 44, 448-468, 1992.

23. Gerber, H.: Direct measurement of suspended particulate volume concentration and far-infrared extinction coefficient with a laser-diffraction instrument, Applied optics, 30, 4824-4831, 1991.

24. Gilardoni, S., Massoli, P., Giulianelli, L., Rinaldi, M., Paglione, M., Pollini, F., Lanconelli, C., Poluzzi, V., Carbone, S., and Hillamo, R.: Fog scavenging of organic and inorganic aerosol in the Po Valley, Atmospheric Chemistry and Physics, 14, 6967-6981, 2014.

25. Girotto, G., "SINGLE PARTICLE CHARACTERIZATION OF ATMOSPHERIC CARBONACEOUS PARTICLES INFLUENCED BY BIOMASS BURNING", University of Trento, Italy, 2015.

26. Hallett, J., Hudson, J., and Rogers, C.: Characterization of combustion aerosols for haze and cloud formation, Aerosol Science and Technology, 10, 70-83, 1989.

27. Haywood, J., and Boucher, O.: Estimates of the direct and indirect radiative forcing due to tropospheric aerosols: A review, Reviews of geophysics, 38, 513-543, 2000.

28. Horvath, H.: Atmospheric light absorption—A review, Atmospheric Environment. Part A. General Topics, 27, 293-317, 1993.

29. Huang, P.-F., Turpin, B. J., Pipho, M. J., Kittelson, D. B., and McMurry, P. H.: Effects of water condensation and evaporation on diesel chain-agglomerate morphology, Journal of Aerosol Science, 25, 447-459, 1994.

30. Jacobson, M. Z.: Strong radiative heating due to the mixing state of black carbon in atmospheric aerosols, Nature, 409, 695-697, 2001.

31. Katrinak, K. A., Rez, P., Perkes, P. R., and Buseck, P. R.: Fractal geometry of carbonaceous aggregates from an urban aerosol, Environmental science & technology, 27, 539-547, 1993.

32. Khalizov, A. F., Lin, Y., Qiu, C., Guo, S., Collins, D., and Zhang, R.: Role of OH-initiated oxidation of isoprene in aging of combustion soot, Environmental science & technology, 47, 2254-2263, 2013.

33. Koehler, K. A., DeMott, P. J., Kreidenweis, S. M., Popovicheva, O. B., Petters, M. D., Carrico, C. M., Kireeva, E. D., Khokhlova, T. D., and Shonija, N. K.: Cloud condensation nuclei and ice nucleation activity of hydrophobic and hydrophilic soot particles, Physical Chemistry Chemical Physics, 11, 7906-7920, 10.1039/b905334b, 2009.

34. Kotzick, R., Panne, U., and Niessner, R.: Changes in condensation properties of ultrafine carbon particles subjected to oxidation by ozone, Journal of Aerosol Science, 28, 725-735, 1997.

35. Kotzick, R., and Niessner, R.: The effects of aging processes on critical supersaturation ratios of ultrafine carbon aerosols, Atmospheric Environment, 33, 2669-2677, 1999.

36. Kulkarni, G., Pekour, M., Afchine, A., Murphy, D. M., and Cziczo, D. J.: Comparison of experimental and numerical studies of the performance characteristics of a pumped counterflow virtual impactor, Aerosol Science and Technology, 45, 382-392, 2011.

37. Kütz, S., and Schmidt-Ott, A.: Characterization of agglomerates by condensation-induced restructuring, Journal of Aerosol Science, 23, 357-360, 1992.

38. Lary, D., Shallcross, D., and Toumi, R.: Carbonaceous aerosols and their potential role in atmospheric chemistry, Journal of Geophysical Research: Atmospheres, 104, 15929-15940, 1999.

39. Lee, C., and Kramer, T. A.: Prediction of three-dimensional fractal dimensions using the two-dimensional properties of fractal aggregates, Advances in colloid and interface science, 112, 49-57, 2004.

40. Liu, L., and Mishchenko, M. I.: Effects of aggregation on scattering and radiative properties of soot aerosols, Journal of Geophysical Research: Atmospheres, 110, 2005.

41. Liu, L., Mishchenko, M. I., and Arnott, W. P.: A study of radiative properties of fractal soot aggregates using the superposition T-matrix method, Journal of Quantitative Spectroscopy & Radiative Transfer, 109, 2656-2663, 10.1016/j.jqsrt.2008.05.001, 2008.

42. Ma, X., Zangmeister, C. D., Gigault, J., Mulholland, G. W., and Zachariah, M. R.: Soot aggregate restructuring during water processing, Journal of Aerosol Science, 66, 209-219, 2013.

43. Mahrt, F., Marcolli, C., David, R. O., Grönquist, P., Barthazy Meier, E. J., Lohmann, U., and Kanji, Z. A.: Ice nucleation abilities of soot particles determined with the Horizontal Ice Nucleation Chamber, Atmos. Chem. Phys. Discuss., https://doi.org/10.5194/acp-2018-557, in review, 2018.

44. Mandelbrot, B. B., and Pignoni, R.: The fractal geometry of nature, WH freeman New York, 1983.

45. Martins, J. V., Hobbs, P. V., Weiss, R. E., and Artaxo, P.: Sphericity and morphology of smoke particles from biomass burning in Brazil, Journal of Geophysical Research: Atmospheres, 103, 32051-32057, 1998.

46. Mikhailov, E., Vlasenko, S., Podgorny, I., Ramanathan, V., and Corrigan, C.: Optical properties of soot–water drop agglomerates: An experimental study, Journal of Geophysical Research: Atmospheres, 111, 2006.

47. Oberdörster, G.: Pulmonary effects of inhaled ultrafine particles, International archives of occupational and environmental health, 74, 1-8, 2000.

48. Oh, C., and Sorensen, C.: The effect of overlap between monomers on the determination of fractal cluster morphology, Journal of Colloid and Interface Science, 193, 17-25, 1997.

49. Peng, J., Hu, M., Guo, S., Du, Z., Zheng, J., Shang, D., Zamora, M. L., Zeng, L., Shao, M., and Wu, Y.-S.: Markedly enhanced absorption and direct radiative forcing of black carbon under polluted urban environments, Proceedings of the National Academy of Sciences, 113, 4266-4271, 2016.

50. Penner, J., Eddleman, H., and Novakov, T.: Towards the development of a global inventory for black carbon emissions, Atmospheric Environment. Part A. General Topics, 27, 1277-1295, 1993.

51. Popovicheva, O., Persiantseva, N. M., Shonija, N. K., DeMott, P., Koehler, K., Petters, M., Kreidenweis, S., Tishkova, V., Demirdjian, B., and Suzanne, J.: Water interaction with hydrophobic and hydrophilic soot particles, Physical Chemistry Chemical Physics, 10, 2332-2344, 2008.

52. Pósfai, M., Anderson, J. R., Buseck, P. R., and Sievering, H.: Soot and sulfate aerosol particles in the remote marine troposphere, Journal of Geophysical Research: Atmospheres, 104, 21685-21693, 1999.

53. Pósfai, M., Simonics, R., Li, J., Hobbs, P. V., and Buseck, P. R.: Individual aerosol particles from biomass burning in southern Africa: 1. Compositions and size distributions of carbonaceous particles, Journal of Geophysical Research: Atmospheres, 108, 2003.

54. Radney, J. G., You, R., Ma, X., Conny, J. M., Zachariah, M. R., Hodges, J. T., and Zangmeister, C. D.: Dependence of soot optical properties on particle morphology: measurements and model comparisons, Environmental science & technology, 48, 3169-3176, 2014.

55. Ramanathan, V., and Carmichael, G.: Global and regional climate changes due to black carbon, Nature geoscience, 1, 221-227, 2008.

56. Ramaswamy, V., Boucher, O., Haigh, J., Hauglustine, D., Haywood, J., Myhre, G., Nakajima, T., Shi, G., and Solomon, S.: Radiative forcing of climate, Climate change, 349, 2001.

57. Reid, J., Koppmann, R., Eck, T., and Eleuterio, D.: A review of biomass burning emissions part II: intensive physical properties of biomass burning particles, Atmospheric Chemistry and Physics, 5, 799-825, 2005.

58. Rissler, J., Nordin, E. Z., Eriksson, A. C., Nilsson, P. T., Frosch, M., Sporre, M. K., Wierzbicka, A., Svenningsson, B., Löndahl, J., and Messing, M. E.: Effective density and mixing state of aerosol particles in a near-traffic urban environment, Environmental science & technology, 48, 6300-6308, 2014.

59. Russell, L. M., Maria, S. F., and Myneni, S. C.: Mapping organic coatings on atmospheric particles, Geophysical Research Letters, 29, 2002.

60. Saleh, R., Robinson, E. S., Tkacik, D. S., Ahern, A. T., Liu, S., Aiken, A. C., Sullivan, R. C., Presto, A. A., Dubey, M. K., and Yokelson, R. J.: Brownness of organics in aerosols from biomass burning linked to their black carbon content, Nature Geoscience, 7, 647-650, 2014.

61. Schmid, O., and Stoeger, T.: Surface area is the biologically most effective dose metric for acute nanoparticle toxicity in the lung, Journal of Aerosol Science, 99, 133-143, 2016.

62. Schneider, C. A., Rasband, W. S., and Eliceiri, K. W.: NIH Image to ImageJ: 25 years of image analysis, Nature methods, 9, 671-675, 2012.

63. Schnitzler, E. G., Gac, J. M., and Jäger, W.: Coating surface tension dependence of soot aggregate restructuring, Journal of Aerosol Science, 106, 43-55, 2017.

64. Shingler, T., Sorooshian, A., Ortega, A., Crosbie, E., Wonaschütz, A., Perring, A. E., Beyersdorf, A., Ziemba, L., Jimenez, J. L., and Campuzano-Jost, P.: Ambient observations of hygroscopic growth factor and f (RH) below 1: Case studies from surface and airborne measurements, Journal of Geophysical Research: Atmospheres, 121, 2016.

65. Slowik, J. G., Stainken, K., Davidovits, P., Williams, L. R., Jayne, J. T., Kolb, C. E., Worsnop, D. R., Rudich, Y., DeCarlo, P. F., and Jimenez, J. L.: Particle Morphology and Density Characterization by Combined Mobility and Aerodynamic Diameter Measurements. Part 2: Application to Combustion-Generated Soot Aerosols as a Function of Fuel Equivalence Ratio, Aerosol Science and Technology, 38, 1206-1222, 10.1080/027868290903916, 2004.

66. Slowik, J. G., Cross, E. S., Han, J.-H., Kolucki, J., Davidovits, P., Williams, L. R., Onasch, T. B., Jayne, J. T., Kolb, C. E., and Worsnop, D. R.: Measurements of morphology changes of fractal soot particles using coating and denuding experiments: Implications for optical absorption and atmospheric lifetime, Aerosol science and technology, 41, 734-750, 2007.

67. Smith, D., Keifer, J., Novicky, M., and Chughtai, A.: An FT-IR study of the effect of simulated solar radiation and various particulates on the oxidation of SO 2, Applied spectroscopy, 43, 103-107, 1989.

68. Smith, D., and Chughtai, A.: Photochemical effects in the heterogeneous reaction of soot with ozone at low concentrations, Journal of Atmospheric Chemistry, 26, 77-91, 1997.

69. Sorensen, C., Cai, J., and Lu, N.: Light-scattering measurements of monomer size, monomers per aggregate, and fractal dimension for soot aggregates in flames, Applied Optics, 31, 6547-6557, 1992.

70. Stoeger, T., Reinhard, C., Takenaka, S., Schroeppel, A., Karg, E., Ritter, B., Heyder, J., and Schulz, H.: Instillation of six different ultrafine carbon particles indicates a surface area threshold dose for acute lung inflammation in mice, Environmental health perspectives, 114, 328, 2006.

71. Tivanski, A. V., Hopkins, R. J., Tyliszczak, T., and Gilles, M. K.: Oxygenated interface on biomass burn tar balls determined by single particle scanning transmission X-ray microscopy, The Journal of Physical Chemistry A, 111, 5448-5458, 2007.

72. Tritscher, T., Jurányi, Z., Martin, M., Chirico, R., Gysel, M., Heringa, M. F., DeCarlo, P. F., Sierau, B., Prévôt, A. S., and Weingartner, E.: Changes of hygroscopicity and morphology during ageing of diesel soot, Environmental Research Letters, 6, 034026, 2011.

73. Van Poppel, L. H., Friedrich, H., Spinsby, J., Chung, S. H., Seinfeld, J. H., and Buseck, P. R.: Electron tomography of nanoparticle clusters: Implications for atmospheric lifetimes and radiative forcing of soot, Geophysical research letters, 32, 2005.

74. Wang, Y., Liu, F., He, C., Bi, L., Cheng, T., Wang, Z., Zhang, H., Zhang, X., Shi, Z., and Li, W.: Fractal Dimensions and Mixing Structures of Soot Particles during Atmospheric Processing, Environmental Science & Technology Letters, 4, 487-493, 2017.

75. Weingartner, E., Burtscher, H., and Baltensperger, U.: Hygroscopic properties of carbon and diesel soot particles, Atmospheric Environment, 31, 2311-2327, 1997.

76. Wilks, D. S.: Statistical methods in the atmospheric sciences, Academic press, 2011.

77. Zhang, G., Lin, Q., Peng, L., Bi, X., Chen, D., Li, M., Li, L., Brechtel, F. J., Chen, J., and Yan, W.: The single-particle mixing state and cloud scavenging of black carbon: a case study at a high-altitude mountain site in southern China, Atmospheric Chemistry and Physics, 17, 14975-14985, 2017.

78. Zuberi, B., Johnson, K. S., Aleks, G. K., Molina, L. T., Molina, M. J., and Laskin, A.: Hydrophilic properties of aged soot, Geophysical research letters, 32, 2005.

2.7 Supplemental Information

Table S1. Morphological parameters calculated for soot particles from the sunny and the foggy morning events for soot in category C0 and C1, only. The total error (in square brackets) is calculated by adding all the errors in quadrature, as discussed earlier in section 2.3.3.2 in the main paper.

Parameter	Sunny: 109 particles Mean ± S.D. (S.E.) [total error]	Foggy morning: 144 particles Mean ± S.D. (S.E.) [total error]
Convexity	0.71 ± 0.13 (0.01) [0.03]	0.80 ± 0.11 (0.01) [0.03]
Roundness	0.43 ± 0.15 (0.01) [0.02]	0.52 ± 0.14 (0.01) [0.03]
L_{max} (nm)	529 ± 290 (28) [29]	343 ± 150 (13) [14]
W (nm)	330 ± 200 (19) [20]	227 ± 95 (7.9) [8.9]
AR	1.66 ± 0.45 (0.04) [0.05]	1.53 ± 0.34 (0.03) [0.04]
d_m (nm)	38.7 ± 10.2 (1.4) [5.6]	35.7 ± 6.7 (0.56) [5.0]
D_{Aeq} (nm)	326 ± 155 (15) [18]	237 ± 93 (8) [11]

Table S2. Morphological parameters studied for IS and RS with mean and 1 S.D. values.

Parameter	IS: 161 particles Mean ± S.D. (S.E.) [total error]	RS: 160 particles Mean ± S.D. (S.E.) [total error]
Convexity	0.56 ± 0.13 (0.01) [0.02]	0.78 ± 0.14 (0.01) [0.03]
Roundness	0.29 ± 0.12 (0.01) [0.02]	0.48 ± 0.16 (0.01) [0.02]
L_{max} (nm)	491 ± 240 (19) [20]	300 ± 190 (15) [16]
W (nm)	260 ± 130 (10) [11]	186 ±110 (8.4) [9.1]
AR	1.95 ± 0.6 (0.05) [0.06]	1.63 ± 0.44 (0.03) [0.05]
d_m (nm)	26.4 ± 4.3 (0.74) [3.8]	29.8 ± 6.1 (1.2) [4.3]
D_{Aeq} (nm)	239 ± 89 (7) [10]	192 ± 96 (8) [10]

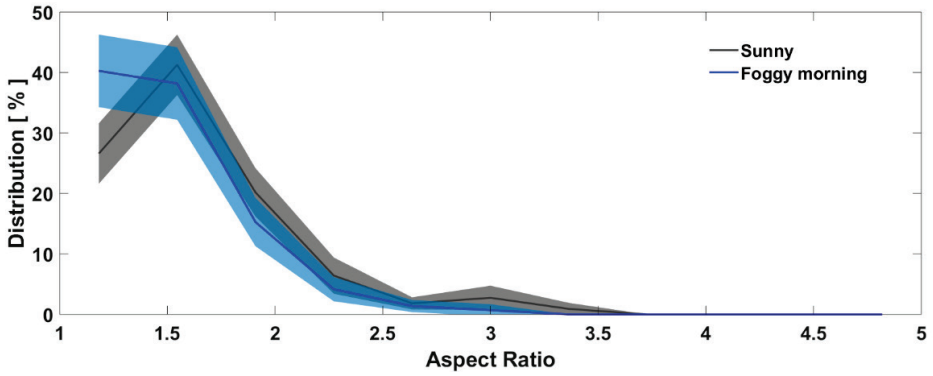

(a)

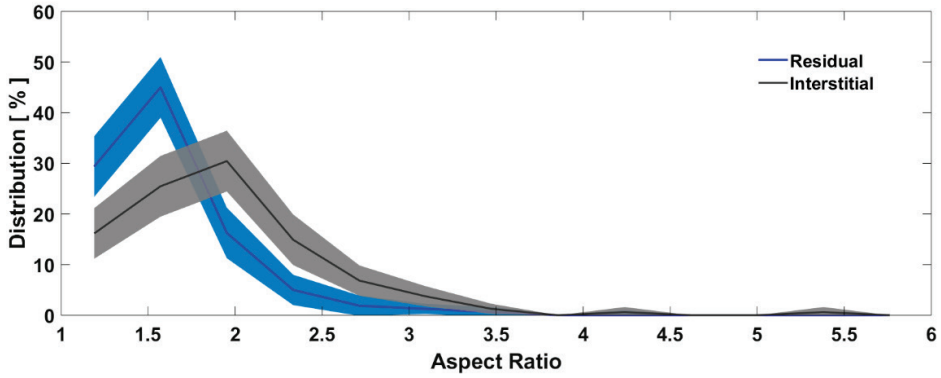

(b)

Figure S1. Distribution of aspect ratio of soot particles **a**) in category C0 and C1 for sunny and foggy morning events, **b**) for IS and RS samples from the π-chamber. The colored bands on each plot represent ± 1 S.D.

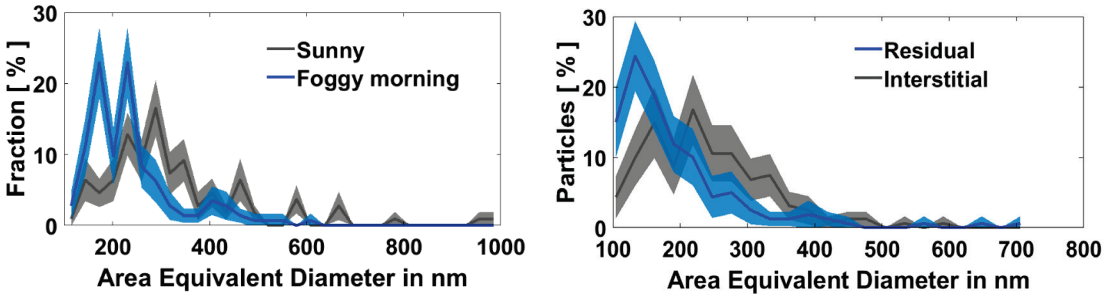

(a) (b)

Figure S2. Distribution of the area equivalent diameter of soot particles (**a**) in category C0 and C1 for sunny and foggy morning events, (**b**) for IS and RS samples. The coloured bands on each plot represent the ±1 S.D.

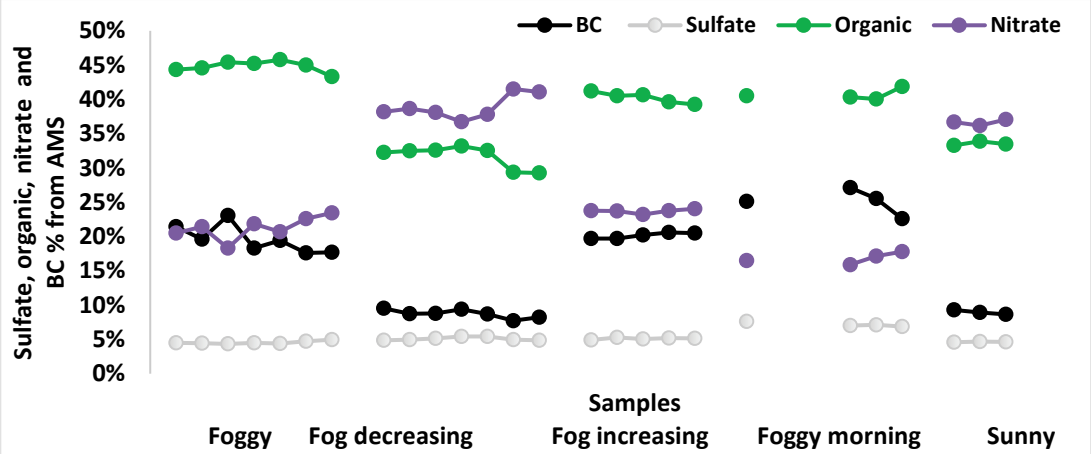

Figure S3. AMS aerosol composition for sunny and foggy events. The dots represent 5-minutes averaged data points for each sample.

Since fresh soot particles have a fractal-like structure (Oh and Sorensen, 1997), the mass of soot scales with its length following a power law given by Mandelbrot and Pignoni (1983). Because the mass of soot is proportional to the number of monomers N in the aggregate, this scaling law is often expressed as:

$$N = k_g \left(\frac{2R_g}{d_m}\right)^{D_f} \quad \text{(SI-1)}$$

where K_g is the fractal prefactor, R_g is the radius of gyration of the aggregate, and d_m is the arithmetic mean diameter of the monomers. The exponent D_f is the fractal dimension. Lacy soot aggregates have lower values of D_f than compact soot particles. The ensemble method, in which N for several soot particles is plotted as a function of the radius of gyration (or a surrogate of it) and a power law is fitted to the data, is commonly used to calculate D_f for lacy aggregates when $D_f < 2$ (Brasil et al., 1999;China et al., 2014;Oh and Sorensen, 1997). However, for the purpose of our study, we are also interested in highly compact soot

particles with D_f>2. For such compact soot aggregates, the use of the ensemble method would provide erroneous results due also to an underestimation of N calculated from 2-D (projected) images (China et al., 2015). Thus, we calculated what we call a 2-D ensemble fractal dimension (D_{2f}) where the particle projected area (A_p) scales with one of its length scales, chosen to be L_{max}, similarly to the scaling law given by Lee and Kramer (2004):

$$A_p = K_{2g} (L_{max})^{D_{2f}} \quad \text{(SI-2)}$$

where K_{2g} is a "two-dimensional" prefactor and L_{max} is the maximum length of the aggregate.

The D_{2f} values for the samples from sunny and foggy morning events along with the π-chamber samples are listed in table below.

Sample	D_{2f} with S.D.
Sunny event (109 particles)	1.79 (0.01)
Foggy morning event (144 particles)	1.81 (0.02)
IS (161 particles)	1.54 (0.02)
RS (160 particles)	1.63 (0.01)

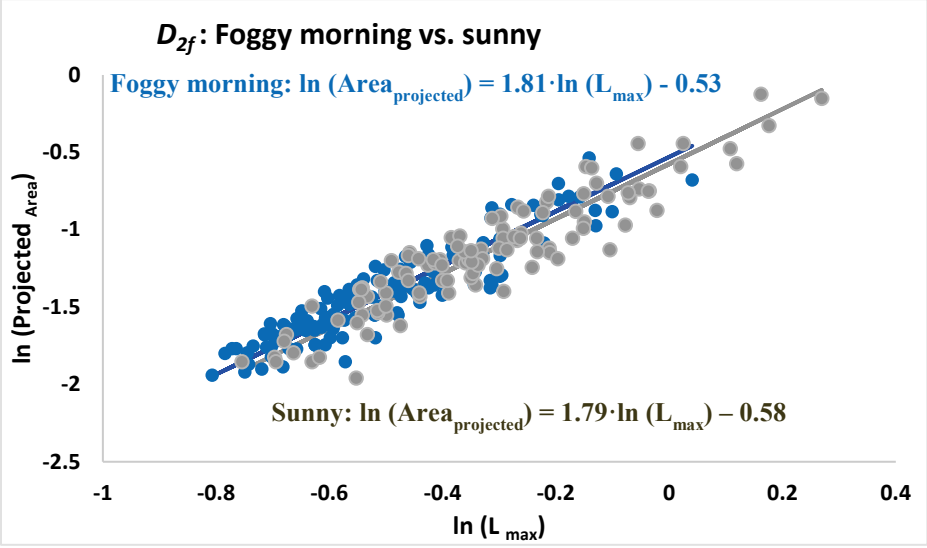

(a)

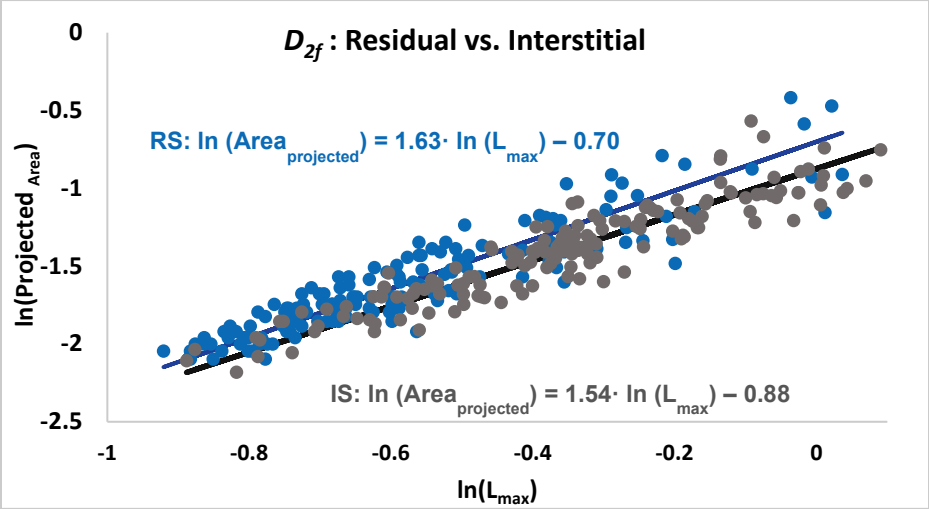

(b)

Figure S4. D_{2f} for **a**) RS and IS, **b**) sunny and foggy events. The dots represent the data points and the lines represent the linear fitting.

We calculated the D_{2f} between the IS and RS to quantify soot restructuring and compaction by cloud processing. The D_{2f} for the IS and RS soot are shown in Fig. S3 where the logarithm of A_p is plotted as a function of the logarithm of L_{max}. The slope for the RS is higher than for the IS (1.63 vs. 1.54) indicating compaction of soot particles after cloud processing. In earlier studies, higher values of D_f have been reported for soot particles after cloud processing (e.g., Colbeck et al., 1990;Zuberi et al., 2005).

It may be noted that for both soot samples from sunny and foggy morning events, D_{2f} has similar values. This might reflect the fact that different soot sources contribute to the ambient samples making the ensemble approach needed for the D_{2f} estimate less appropriate and sensitive for detecting changes in morphology than non-ensemble parameters such as the convexity and roundness.

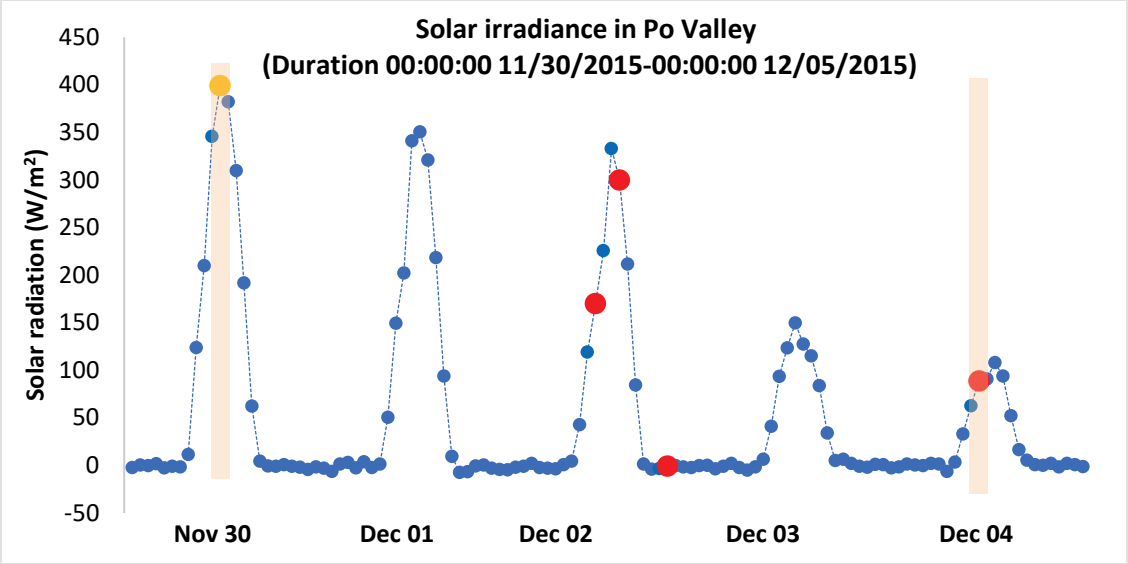

Figure S5. Solar irradiance in the Po Valley during the period of collection of the five samples studied here. The yellow and red dots represent the sunny and foggy events, respectively. The shades represent those samples that have been used for the study of cloud processing. The data points are hourly data points.

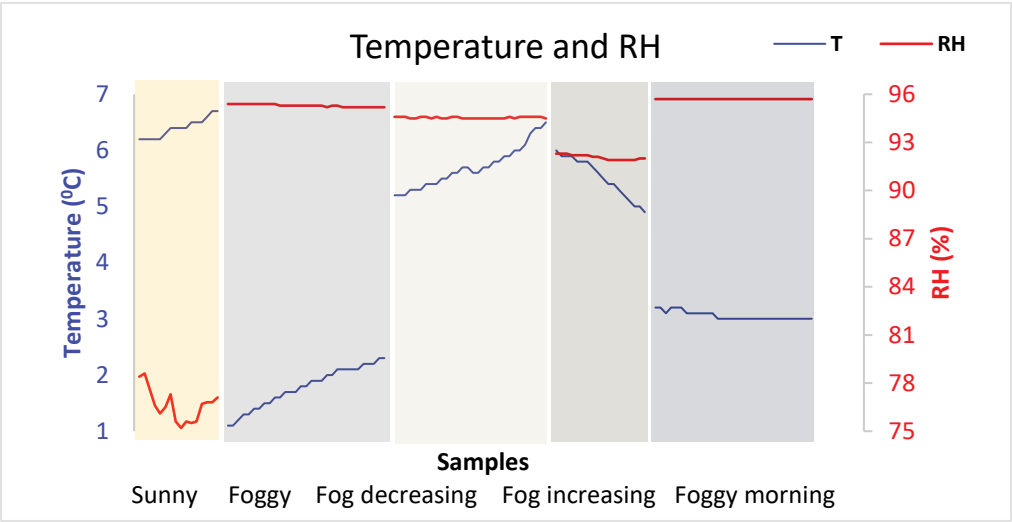

Figure S6. Temperature and relative humidity in the Po Valley, during the collection of the five samples under study.

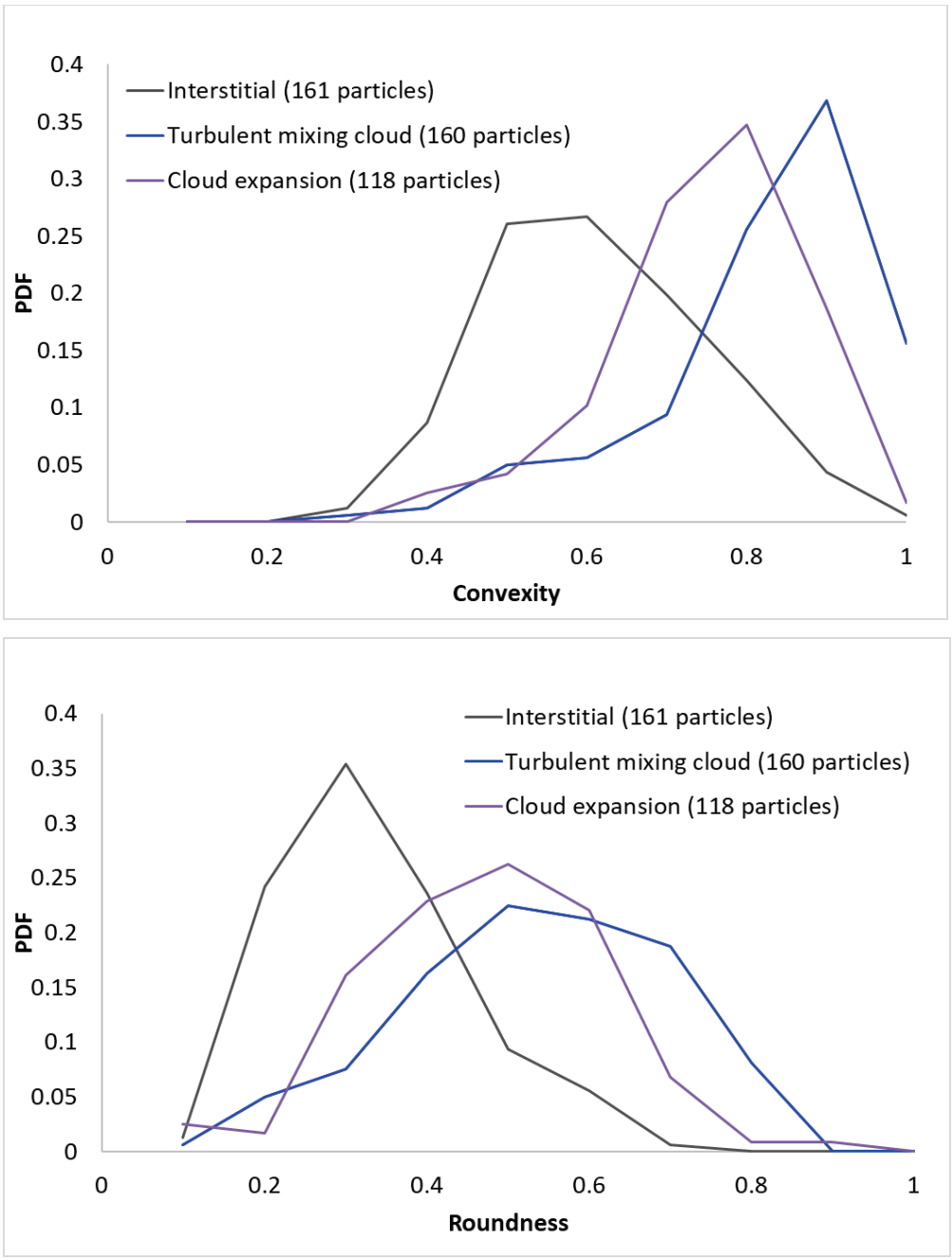

Figure S7. Convexity and roundness distribution of soot particles from the π-chamber for fresh (interstitial) soot, soot from single expansion and soot after turbulent mixing cloud processing experiments.

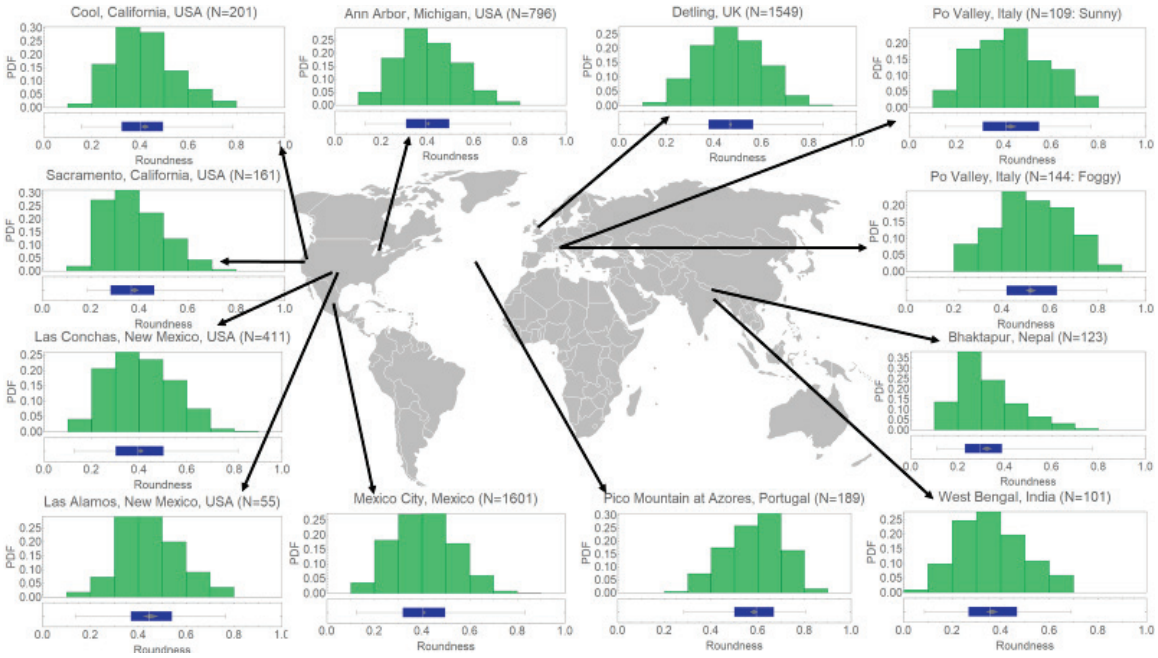

Figure S8. Histogram and box plot for the roundness of thinly coated soot particles from different locations. On each box plot, the vertical white line represents the median and the grey diamond represents the mean confidence interval for each distribution. For each distribution, N in the bracket is the number of soot particles analyzed and PDF on the y-axis is the probability distribution of particles for each bin as a function of roundness.

References

1. Brasil, A., Farias, T. L., and Carvalho, M.: A recipe for image characterization of fractal-like aggregates, Journal of Aerosol Science, 30, 1379-1389, 1999.

2. China, S., Salvadori, N., and Mazzoleni, C.: Effect of traffic and driving characteristics on morphology of atmospheric soot particles at freeway on-ramps, Environmental science & technology, 48, 3128-3135, 2014.

3. China, S., Scarnato, B., Owen, R. C., Zhang, B., Ampadu, M. T., Kumar, S., Dzepina, K., Dziobak, M. P., Fialho, P., and Perlinger, J. A.: Morphology and mixing state of aged soot particles at a remote marine free troposphere site: Implications for optical properties, Geophysical Research Letters, 42, 1243-1250, 2015.

4. Colbeck, I., Appleby, L., Hardman, E., and Harrison, R. M.: The optical properties and morphology of cloud-processed carbonaceous smoke, Journal of Aerosol Science, 21, 527-538, 1990.

5. Lee, C., and Kramer, T. A.: Prediction of three-dimensional fractal dimensions using the two-dimensional properties of fractal aggregates, Advances in colloid and interface science, 112, 49-57, 2004.

6. Mandelbrot, B. B., and Pignoni, R.: The fractal geometry of nature, WH freeman New York, 1983.

7. Oh, C., and Sorensen, C.: The effect of overlap between monomers on the determination of fractal cluster morphology, Journal of Colloid and Interface Science, 193, 17-25, 1997.

8. Zuberi, B., Johnson, K. S., Aleks, G. K., Molina, L. T., Molina, M. J., and Laskin, A.: Hydrophilic properties of aged soot, Geophysical research letters, 32, 2005.

3 Chapter 3: Effect of thermodenuding on the structure of nascent flame soot aggregates[2]

3.1 Abstract

The optical properties (absorption and scattering) of soot particles depend on soot size and index of refraction, but also on the soot complex morphology and the internal mixing with materials that can condense on a freshly emitted (nascent) soot particle and coat it. This coating can affect the soot optical properties by refracting light, or by changing the soot aggregate structure. A common approach to studying the effect of coating on soot optical properties is to measure the absorption and scattering coefficients in ambient air, and then measure them again after removing the coating using a thermodenuder. In this approach, it is assumed that: (1) most of the coating material is removed; (2) charred organic coating does not add to the refractory carbon; (3) oxidation of soot is negligible; and, (4) the structure of the pre-existing soot core is left unaltered, despite the potential oxidation of the core at elevated temperatures. In this study, we investigated the validity of the last assumption, by studying the effect of thermodenuding on the morphology of nascent soot. To this end, we analyzed the morphological properties of laboratory generated nascent soot, before and after thermodenuding. Our investigation shows that there is only minor restructuring of nascent soot by thermodenuding.

---

[2] The material contained in this chapter was previously published in the *MDPI Atmosphere* journal: Bhandari, J., China, S., Onasch, T., Wolff, L., Lambe, A., Davidovits, P., Cross, E., Ahern, A., Olfert, J., Dubey, M. and Mazzoleni, C., 2017. Effect of thermodenuding on the structure of nascent flame soot aggregates. *Atmosphere*, *8*(9), p.166.

3.2 Introduction

Soot particles are mostly composed of refractory carbonaceous material that forms from incomplete combustion during burning activities (Haynes and Wagner, 1981). A nascent soot particle appears as a fractal-like (sometimes referred to as a lacy) aggregate of small spherules (called nanospheres or monomers) (Buseck et al., 2014) and its structure is scale invariant (Sorensen, 2001). Here, the term "nascent" is used to refer to freshly emitted soot particles that have a negligible coating on the monomers. The diameter of these monomers varies in a range from 10 nm to more than 50 nm, depending on the fuel source and combustion conditions (Adachi and Buseck, 2008; Bambha et al., 2013a; China et al., 2014; Park et al., 2004). During the atmospheric processing, soot particles interact with organic and inorganic materials (in the form of aerosol or condensable vapors). During these interactions, soot undergoes morphological changes including compaction, coagulation, and coating (China et al., 2015). Combustion generated nascent soot aggregates often have different kinds of polycyclic aromatic hydrocarbons (PAHs) that thinly coat the monomers, depending upon the flaming conditions and fuel types, even in very controlled combustions (Cross et al., 2010). In this case, coating is acquired at the source, and not added later through atmospheric processing. The degree of coating in atmospheric particles is very variable (China et al., 2014; China et al., 2015; Adachi et al., 2010; China et al., 2013; Healy et al., 2015; Liu et al., 2015a; Zhang et al., 2008). In some studies, thinly coated soot particles have been found in large fractions in the atmosphere. For example, in the study by China et al. (2014), a large fraction (by number) of freshly emitted soot particles collected on freeway on ramps were thinly coated (72%). In another field study, carried out at Pico Mountain Observatory in the Azores, China et al. (2015) found that 37% of the soot particles in one sample, were thinly coated, even after days of atmospheric processing during the long range transport in the free troposphere from the source. These two studies were carried out at very different locations (very near the source in the first study, and very far from the source in the second study), showing that thinly coated soot particles can exist in the atmosphere in different environments and geographic locations. In another study, in two plumes one sampled from Mexico City and one from

outside of Mexico City, Adachi and Buseck (2008) found that 7% of particles were soot without coating. Coating or internal mixing in general, changes the optical properties of soot, even when the structure of the refractory components remains the same. These changes consequently affect the radiative forcing of soot (Adachi and Buseck, 2013; Ghazi and Olfert, 2013; Jacobson, 2001; Lack and Cappa, 2010; Liu et al., 2015b); Schnitzler et al., 2014; Van Poppel et al., 2005; Westcott et al., 2008). Several studies have also shown that coating of soot by partially-absorbing or non-absorbing materials increases the absorption and scattering cross sections (Liu et al., 2015a; Lack and Cappa, 2010; Cappa et al., 2012; Fuller et al., 1999; Khalizov et al., 2009). These increases are termed "absorption and scattering enhancements" (E_{abs} and E_{sca}). The enhancement is typically calculated as the ratio of the light absorption or scattering coefficient of the coated soot to the light absorption or scattering coefficient of the soot core, after the coating material has been removed (Lack and Cappa, 2010).

Thermodenuders (TDs) that remove the coating by evaporation, are often used in the field and in the laboratory to study and quantify these optical enhancements (Ghazi and Olfert, 2013; Bambha et al., 2013b; Lack et al., 2012; Xue et al., 2009). During the thermodenuding process, coated soot particles are passed through a heated column, typically at ~200–300 °C to evaporate the volatile coating material while leaving behind the refractory soot (Huffman et al., 2008; Wehner et al., 2002). The temperature gradient within the TD can result in particle losses due to thermophoretic forces, though these losses can be measured and accounted for Huffman et al., 2008).To correctly assess the E_{abs} and E_{sca} using a TD, one needs to make the following assumptions: (1) most of the coating material is removed from the soot by the TD; (2) organic coating material does not transform into refractory carbon due to charring; (3) refractory carbon is not oxidized to a substantial extent under elevated temperatures; and, (4) the structure of the refractory soot particle is unaffected, meaning that the thermodenuding process alone does not induce restructuring of the core lacy soot aggregates.

Contrary to assumption (1), thermodenuding may not remove refractory particulate material, such as some inorganic salts, and may not remove all of the non-refractory material from soot particles [23]. For example, Liu et al. (2015a) observed that denuded soot still contained heavily coated soot particles, although, in a smaller fraction with respect to ambient particles, suggesting that the TD may not completely remove the coating. Healy et al. (2015) found that, on average, only 74% of the mass of coating material was removed from soot samples after thermodenuding. The mass removal efficiency by the TD was even less (approximately 60%) for wildfire emission samples. Swanson and Kittelson (2010) have also cautioned about semi-volatile particle artifacts due to incomplete removal of evaporated compounds in the TD. Similarly, Knox et al. (2009) found that there was no significant difference in the mass absorption cross section between themodenuded and non-thermodenuded aged-soot particles as compared to fresh soot, due to the incomplete removal of coating materials from aged soot particles. On the other hand, Khalizov et al. (2013) hypothesized that the thermodenuder may remove all of the coating material from ambient soot, including the coating acquired during atmospheric processing, as well as the nascent coating present on soot at the source, and therefore, they suggested that the denuded particles cannot represent the nascent soot morphology.

Next, we briefly review assumptions (2) and (3). The elevated temperatures during the thermodenuding process may cause charring of some organic matter into refractory, elemental carbon, and /or some oxidation of the carbonaceous matter. The charring of organic particulate material into elemental carbon is a known phenomenon under the elevated temperatures employed in organic carbon and elemental carbon (OCEC) analyses (Chow et al., 2004; Countess, 1990). Issues that influence the charring include temperatures and residence times, as well as chemical composition. Charring is likely to be more of an issue for oxidized organics, such as biomass burning or secondary organic aerosol (SOA), than reduced organics, such as efficient combustion products (i.e., diesel and laboratory flame soot) (Cheng et al., 2011; Khan et al., 2012). Two significant differences between OCEC and thermodenuding include: (1) OCEC techniques typically operate at higher temperatures than TDs, and (2) OCEC charring occurs in a helium

atmosphere, whereas thermodenuding occurs in air (i.e., oxidizing environment). Thus, at a low temperature (<300 °C), thermodenuding will be less likely to char, and the particles may be more susceptible to oxidation due to an oxidizing environment. Oxidation of refractory carbon soot typically occurs at significantly elevated temperatures, but can occur at lower temperatures as well, especially if catalyzed by impurities in the soot (Stanmore et al., 2001). Soot oxidation is likely limited in thermodenuding due to the low temperatures and the relatively short residence time, but this issue will require more study in the future.

We finally discuss the assumption (4), which is the focus of our study. Previous studies have shown that nascent soot particles can restructure during the condensation or evaporation of the coating material, depending on their surface tension (Ebert et al., 2002; Ma et al., 2013; Tritscher et al., 2011). Xue et al. (2009) found significant restructuring of soot particles when the particles were first coated with glutaric acid and then denuded. Ghazi and Olfert (2013) reported the dependence of soot restructuring on the mass amount of different coating material types. This restructure alone can affect the optical properties of soot particles. For example, a laboratory study was performed on soot compacted upon humidification; the study measured modest changes in the absorption cross-section (5% to 14%), but the extinction cross-section was much more sensitive to compaction, with changes of more than 30% (Radney et al., 2014). Similarly, China et al. (2015, 2015b), using numerical simulations, predicted small changes in the absorption cross-section (a few percent), but a much more substantial change in the total scattering cross section (up to ~300%) upon soot compaction. In addition to affecting the optical properties, changes in the soot structure can also affect the results of laser induced incandescence measurements (Bambha et al., 2013a. Finally, the condensation of secondary organic matter preferentially takes place in empty pores on soot particles, and therefore, it is possible that compaction will affect secondary organic condensation on soot (Popovicheva et al., 2003). Two potential explanations for the coated soot restructuring detected during these studies can be: (1) Soot might be compacted during condensation of the coating materials due to surface tension effects (Zhang et al., 2008; Tritscher et al., 2011; Huang et al., 1994; Schnitzler et al., 2017). (2) The removal of the coating material during the subsequent

thermodenuding may cause compaction when the coating evaporates, still due to surface tension effects (Ebert et al., 2002; Ma et al., 2013). However, we hypothesize a third potential pathway, in which soot restructuring might take place solely due to the thermodenuding process, through the added thermal energy. Coating alone might not cause full compaction (i.e., completely collapsed structure). For example, in an experiment, Leung et al. (2017) found that the coating did not restructure the soot aggregate even when the aggregate was completely covered by the coating material. Some coating material indeed results in substantial or even maximum compaction, but other coating materials actually result in negligible compaction. A clear example is shown in a laboratory study where particles coated with sulfuric acid did undergo severe restructuring, while the soot particles coated by dioctyl sebacate showed only minimal or no compaction (Cross et al., 2010). Also, from Mexico City samples, Adachi and Buseck (2008) found coated soot but with lacy structure**.** For the case of coated but yet only partially compacted soot, thermodenuding may facilitate further restructuring. The coating material can become less viscous at the elevated temperatures during the thermodenuding and restructure the soot core Leung et al. (2017).

Next, we will discuss some lines of evidence that the thermodenuding process alone can in some cases, favor the compaction of lacy aggregates of various materials, even in the absence of coating material that condenses onto the primary aggregates. If a similar process happens for ambient soot, such a process would potentially bias the measured properties (e.g., absorption or scattering enhancements) of soot when a thermodenuder is used. The main objective of our study is to test this hypothesis, to assure that the themodenuding process alone does not introduce this bias. A couple of potential restructuring processes induced during thermodenuding, are discussed next:

(a) When heated, fractal-like aggregates of metal nanoparticles, such as silver, copper, and metallic oxides (e.g., titania), have been found to restructure to more compact morphologies at temperatures well below the bulk material melting points. For example, thermal restructuring has been found in silver aggregates, even at temperatures as low as 100 °C, with full compaction at just 350 °C (much below

the melting temperature of silver), while the primary particle size remained unchanged (Weber et al., 1996; Weber and Friedlander, 1997). Another study found that aggregates of titania started to collapse when temperatures reached 700 °C (Jang and Friedlander, 1998). These authors speculated that the heating causes the weakest branches in an aggregate to rotate around their contact points, resulting in the aggregate restructuring. Alternatively, Schmidt-Ott (1998) hypothesized that the monomers in silver nanoparticles aggregates might slide on each other when heated, also causing compaction. Both processes would restructure the aggregates without a complete breakage of the bonds between the monomers due to Van der Waals forces.

(b) As mentioned earlier, nascent soot aggregates typically have polycyclic aromatic hydrocarbons thinly coating them. This nascent coating could play a role in determining the soot structure if the coating properties (i.e., viscosity and surface tension) change at the higher temperature of the thermodenuder. Chen et al. (2016) found that some polycyclic aromatic hydrocarbons, like phenanthrene and flouranthene, when present as a subnanometer layer on soot, behaved as subcooled liquid that weakened the bonds between the monomers, allowing them to slide and roll over each other and resulting in soot restructuring. Rothenbacher et al. (2008) provided evidence that thermodenuding might make a difference in the strength of the adhesive bonds between the monomers. For aged soot, they found a higher degree of fragmentation for thermodenuded particles (75% at 280 °C) than for untreated (not thermodenuded) particles (60%) when impacted at ~200 m/s. The degree of fragmentation was defined as the fraction of broken bonds in an aggregate. Although the process involved both the effect of coating and impaction, the higher degree of fragmentation for thermodenuded particles suggests that the thermal energy has a role on the increased degree of fragmentation.

These lines of evidence motivated us to study the potential effects of thermodenuding on the specific case of nascent soot. With this goal in mind, we analyzed the structure of

laboratory generated nascent soot particles produced from two different fuel sources (ethylene flame and methane flame) and size selected at different mobility diameters before and after thermodenuding. This assessment is important for evaluating the potential biases that might be introduced by thermodenuding while, for example, estimating the absorption or scattering enhancements of laboratory or ambient soot particles.

3.3 Experiments

3.3.1 Experimental Setup and Sample Collection

We analyzed five pairs of mobility-selected soot samples collected during two different experiments: the Boston College Experiment 2 (BC2) and the Boston College Experiment 4 (BC4). The sampling schematics are shown in the Figs. 3-1a, b. None of the soot particles were coated with additional external coating material, and the minimal coating present on the nascent soot was solely due to the fuel residuals accumulated during the combustion and dilution processes.

Three soot sample sets were collected during BC2 from the combustion of ethylene and oxygen using a premixed flat flame burner (Cross et al., 2010). The fuel equivalence ratio (∅) for all the three sample sets was 2.1. A TD (Huffman et al., 2008) was used to remove volatile components from the nascent soot particles. The heating section of the TD was set at 250 °C to vaporize the non-refractory soot components, which were absorbed by a charcoal section maintained at room temperature. Particles for a range of mobility diameters (d_m) were selected to investigate the effect of thermodenuding on particle size. For our investigation, we selected three sets of nascent vs. nascent-denuded soot particles with d_m = 153 nm, 181 nm and 250 nm for nascent and d_m = 151 nm, 175 nm, and 241 nm for the corresponding denuded soot particles. Soot particles were collected on 13 mm diameter Nuclepore polycarbonate filters having a pore size of 0.3 μm (Whatman Inc., Chicago, IL, USA). Additional details regarding the BC2 experimental set-up are provided elsewhere (Cross et al., 2010).

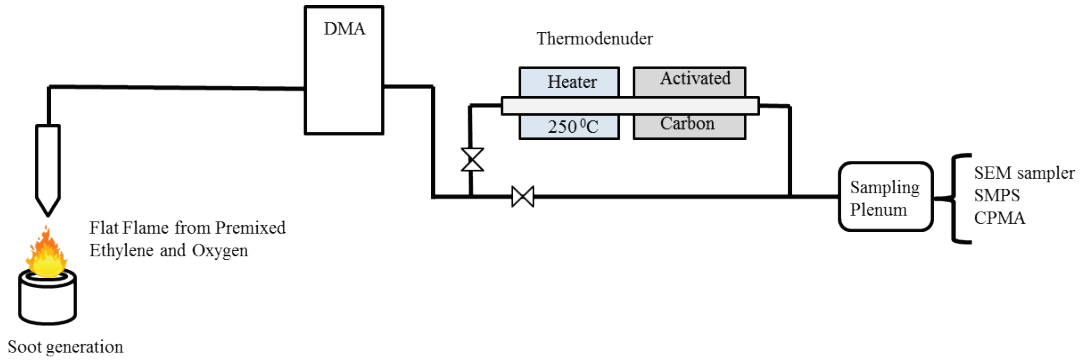

(a)

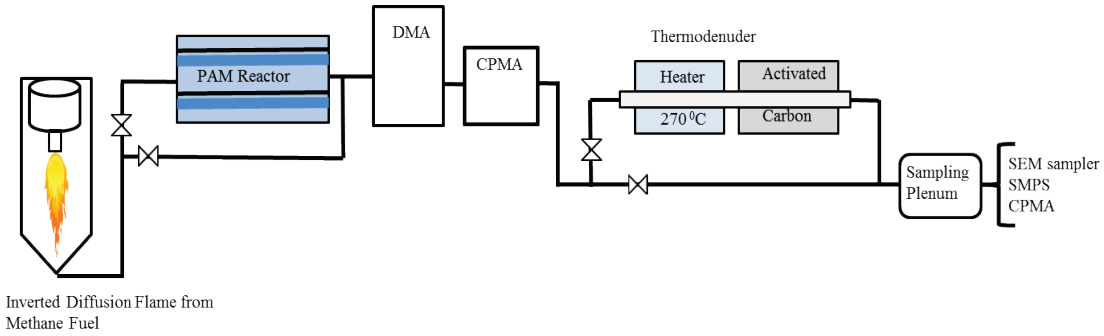

(b)

Figure 3-**1.** Soot generation and sampling set-ups in **a**) Boston College Experiment 2 (BC2) and **b**) Boston College Experiment 4 (BC4).

In addition, we selected two sets of soot samples generated during BC4 from the combustion of methane in an inverted diffusion flame burner (methane and O_2 mixture) at a d_m = 253 nm and 252 nm for nascent and d_m = 253 nm, and 251 nm for the corresponding denuded soot particles. The global ∅ for both sample sets was about 0.7, but the actual value of ∅ is unknown. In the diffusion flame, the fuel burns in excess of air making the value of ∅ less than 1. Effluent from the flame burner was passed through separate annular denuders loaded with molecular sieves and activated charcoal to remove water vapor and

volatile organic compounds from the sample flow**.** As in BC2, a Huffman TD (heating section set at 270 °C) was used to remove the volatile components. For both experiments, the sample flow rate through the TD was 2 LPM, resulting in a residence time of 5 s in the heating section and 4 s in the denuder section. During BC4, unlike during BC2, particles were first mobility size selected by a Differential Mobility Analyzer (DMA) (TSI Inc., St. Paul, MN, USA) and the mass was selected by a Centrifugal Particle Mass Analyzer (CPMA) (Cambustion Ltd., Cambridge, U.K) before thermodenuding. The first set of samples consisted of nascent and nascent-denuded soot, while the second set consisted of nascent-oxidized and nascent-oxidized-denuded soot. Soot was oxidized by exposure to ozone (O_3) and hydroxyl (OH) radicals in a Potential Aerosol Mass (PAM) oxidation flow reactor (Lambe et al., 2011), at input O_3 and H_2O mixing ratios of ~15 ppm and ~1%, and UV actinic flux ~2×10^{12} ph cm^{-2} s^{-1} ($\lambda = 254$ nm). These operating conditions correspond to an integrated OH exposure of approximately 2×10^{12} molec cm^{-3} s (Lambe et al., 2015a), and likely generate highly oxygenated organic molecules, such as carboxylic acids on the surface of the nascent-oxidized soot particles (Lambe et al., 2015b). The nascent-oxidized soot was thermo-denuded at a temperature of 270 °C. The set of nascent-oxidized soot samples was included here to investigate if the thermodenuding effect is different for nascent versus nascent-oxidized soot. During BC4, soot particles were collected on 13 mm diameter Nuclepore filters having a pore size of 0.1 μm diameter (Whatman Inc, Chicago, IL, USA).

All the filters were coated with 1.8 (±10%) nm thick layer of Pt/Pd alloy in a sputter coater (Hummer® 6.2, Anatech USA, Union city, CA, USA) and imaged with a field emission scanning electron microscope (FE-SEM) (Hitachi S-4700, Tokyo, Japan). From the FE-SEM images, several morphological parameters were evaluated (China et al., 2014) using the image processing software ImageJ (National Institutes of Health, Bethesda, Maryland, USA) (Schneider et al., 2012).

3.3.2 Soot Morphological Parameters

As mentioned in the introduction, soot particles are aggregates of monomers that exhibit scale-invariant fractal structures (Forrest and Witten Jr, 1979; Sorensen et al., 1992). Soot aggregates can therefore be characterized by a fractal dimension *(D_f),* in which the mass of the aggregate *M* (proportional to the number of monomers *N* in the aggregate) scales with the ratio of the radius of gyration *(R_g)* to the radius of the monomers *(R_p),* as in *M* (or *N*) $\propto (R_g/R_p)^{D_f}$, (Lin et al., 1989). D_f is a commonly used parameter to quantify the soot morphology. Lacy soot particles have low D_f values, while compact soot particles have higher D_f values. The D_f of an ensemble of soot particles can be calculated by plotting *N* vs. R_g (or a surrogate for it). *N* scales with R_g as a power law with exponent D_f (Köylü et al., 1995):

$$N = k_g \left(\frac{R_g}{R_p}\right)^{D_f} \tag{1}$$

where k_g is a pre-factor whose value depends on the overlap between the monomers in the aggregate. The relation formulated by Köylü et al. (1995) was used to estimate D_f with the geometric mean diameter of the aggregate, $\sqrt{LW}$, as a surrogate for $2R_g$:

$$N = k_{LW} \left(\frac{\sqrt{LW}}{2R_p}\right)^{D_f} \tag{2}$$

where *L* is the maximum length and *W* is the maximum width (orthogonal to *L)*, K_{LW} is a prefactor and R_p is calculated from the mean of the projected area of the monomer. In general, it is difficult to measure *N* using an SEM image alone, because only two-dimensional (2-D) projections of the soot particles are typically available. Therefore, *N* is often estimated from the projected area of the soot aggregate A_p and the mean projected area of the monomers A_m using the relation provided by Oh and Sorensen (1997):

$$N = k_a \left(\frac{A_p}{A_m}\right)^{\alpha} \tag{3}$$

where α and k_a are constants that depend on the overlap between monomers in the 2-D projected image of the particle. In our case, we used K_a = 1.15 and $\alpha = 1.09$ for all of our nascent and nascent-denuded soot aggregates (Köylü et al., 1995). This selection of K_a and α values is reasonable since we only studied nascent soot particles that are minimally coated.

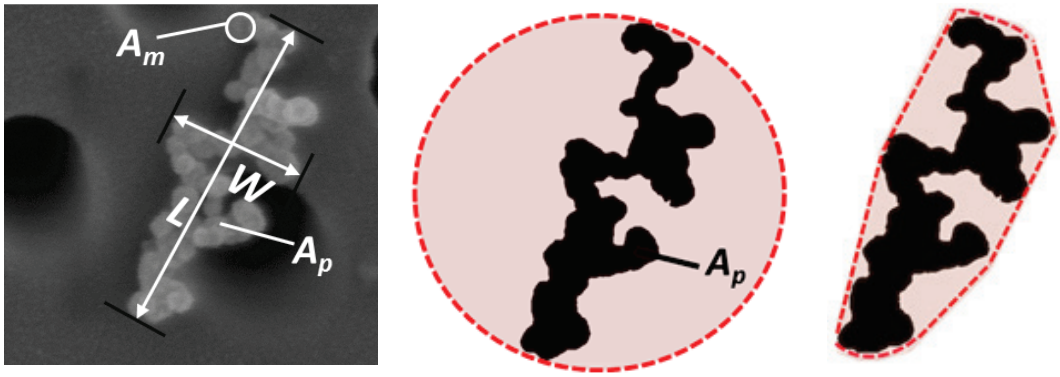

(a) (b) (c)

Figure 3-2a) Example of SEM image of a soot particle showing the definition of several parameters measured from the projected image: maximum projected length L, maximum projected width W, projected area of monomer A_m and projected area of particle A_p. **b**) Schematic representation of the roundness calculation for the same soot particle shown in (a). **c**) Schematic representation of the convexity calculation for the same soot particle shown in (a). The pink shades in (b) and (c) represent the equivalent area for a circle and the convex hull, respectively, for the binary image of the soot particle shown in (a).

In addition to D_f, several other 2-D morphological parameters were calculated from the FE-SEM images to investigate potential changes due to thermodenuding. The calculated parameters included roundness, convexity, aspect ratio (AR), and area equivalent diameter (D_{Aeq}). Figure 3-2a shows the definition of some of these parameters. D_{Aeq} is the diameter of a spherical particle with a projected area equivalent to the projected area of the aggregate. Roundness is calculated from the ratio of the projected area of the aggregate to the area of the circle having a diameter equal to the maximum projected length L, and fully

inscribing the projected image of the aggregate (Fig. 3-2b). Convexity (sometimes termed solidity) is the ratio of the projected area of the particle to the area of the smallest convex hull polygon, in which the 2-D projection of the aggregate is inscribed (Fig. 3-2c). *AR* is calculated as the ratio of *L* to *W*. Higher values of roundness and convexity or lower *AR* often corresponds to more compact soot particles. However, it has to be noted that D_f, roundness and convexity are parameters with very different meanings and definitions. The first is a scaling factor, the second is a geometric property, and the third is a measure of the particle topology. That is why we investigated all of these three parameters to characterize the morphology of soot rather than looking at a single one. We analyzed a total of 1223 images of individual soot particles.

3.4 Results and Discussion

As mentioned earlier, we analyzed images from four sets of nascent and nascent-denuded soot sample pairs of different sizes and a fifth set of nascent-oxidized denuded soot. Examples of images of soot particles before and after thermodenuding are shown in Fig. 3-3.

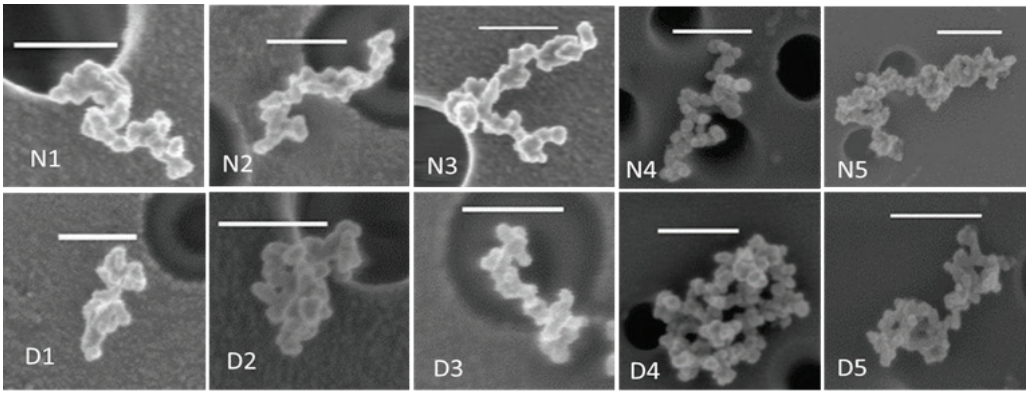

Figure 3-3. SEM micrographs of nascent (*N*) and thermodenuded (*D*) soot particles. The white horizontal bar in each micrograph represents a length scale of 200 nm. Dark circles are the holes in the filter.

N1, N2, N3, and *N4* are four differently sized nascent soot samples and *D1, D2, D3,* and *D4* are the corresponding nascent-denuded sets. *N5-D5* is a pair of nascent-oxidized soot before and after thermodenuding. Table 3-1 summarizes the features of the analyzed soot particles. Sets *N1-D1, N2-D2,* and *N3-D3* are the three sets from BC2, while sets *N4-D4,* and *N5-D5* are from BC4.

Table 3-1. Summary of physical and morphological parameters for the soot particles analyzed.

Experiment	**Statistics**	**BC2**						**BC4**			
Sample		N1	D1	N2	D2	N3	D3	N4	D4	N5	D5
Fuel type		E	E	E	E	E	E	M	M	M	M
#Particles analyzed		108	151	113	163	114	109	113	105	122	125
N	Mean	41	55	121	104	110	153	158	188	155	166
	S.D	16	26	65	53	44	90	96	87	75	106
	S.E	2	2	6	4	4	9	9	8	7	9
d_m (nm)	Mean	153	151	181	175	250	241	253	253	252	251
M_{CPMA} (fg)	Mean	1.02	0.78	1.52	1.08	2.85	2.20	2.37	2.34	2.41	2.18
	S.D.	(0.03)	(0.03)	(0.05)	(0.04)	(0.14)	(0.13)	(0.11)	(0.13)	(0.11)	(0.11)
D_f	Fit slope	1.86	1.84	1.73	1.72	1.78	1.79	1.80	1.76	1.65	1.80
	S.E.	(0.05)	(0.04)	(0.05)	(0.06)	(0.08)	(0.05)	(0.05)	(0.06)	(0.05)	(0.05)
K_g	Fit intercept	1.78	1.98	2.50	2.50	2.22	2.00	2.10	2.56	2.87	2.16
	S.E.	(0.04)	(0.03)	(0.05)	(0.05)	(0.08)	(0.06)	(0.06)	(0.07)	(0.06)	(0.06)
d_p (nm)	Mean	33.5	31.8	26.8	25.7	32.1	30.3	23.5	22.8	23.9	23.1
	Median	33.5	32.4	26.5	25.9	32.1	28.9	23.2	22.5	23.7	23.0

	S.D.	(2.1)	(3.3)	(2.7)	(2.6)	(2.1)	(6.9)	(3.1)	(2.2)	(2.5)	(3.4)
	S.E.	(0.21)	(0.27)	(0.26)	(0.21)	(0.20)	(0.66)	(0.30)	(0.22)	(0.23)	(0.31)
Roundness	Mean	0.41	0.43	0.36	0.34	0.38	0.31	0.31	0.35	0.33	0.33
	Median	0.42	0.42	0.35	0.35	0.35	0.30	0.30	0.34	0.32	0.31
	S.D.	(0.12)	(0.12)	(0.11)	(0.10)	(0.12)	(0.09)	(0.11)	(0.12)	(0.11)	(0.11)
	S.E.	(0.01)	(0.01)	(0.01)	(0.01)	(0.01)	(0.01)	(0.01)	(0.01)	(0.01)	(0.01)
Convexity	Mean	0.72	0.75	0.66	0.66	0.62	0.59	0.61	0.66	0.61	0.63
	Median	0.73	0.74	0.66	0.65	0.62	0.58	0.61	0.66	0.61	0.62
	S.D.	(0.09)	(0.08)	(0.09)	(0.10)	(0.09)	(0.10)	(0.10)	(0.11)	(0.12)	(0.11)
	S.E.	(0.01)	(0.01)	(0.01)	(0.01)	(0.01)	(0.01)	(0.01)	(0.01)	(0.01)	(0.01)
D_{Aeq} (nm)	Mean	169	181	220	196	255	262	215	230	219	214
	Median	171	175	208	189	262	260	199	220	213	202
	S.D.	(33)	(35)	(55)	(41)	(46)	(49)	(54)	(56)	(50)	(59)
	S.E.	(3)	(3)	(5)	(3)	(4)	(5)	(5)	(5)	(5)	(5)
AR	Mean	1.79	1.73	1.84	1.92	1.78	1.85	1.99	1.95	1.85	1.88
	Median	1.66	1.62	1.70	1.78	1.68	1.72	1.85	1.82	1.80	1.83
	S.D.	(0.51)	(0.42)	(0.49)	(0.51)	(0.57)	(0.50)	(0.60)	(0.60)	(0.50)	(0.50)
	S.E.	(0.05)	(0.03)	(0.05)	(0.04)	(0.05)	(0.05)	(0.06)	(0.06)	(0.05)	(0.04)

In Table 3-1, E = ethylene and M = methane represents the fuel type. N is the average number of monomers per aggregate, estimated in each sample using Equation (3). K_g values have been estimated using the relation $K_g = K_{LW} \cdot (1.17)^{Df}$ where $\sqrt{LW}/2R_g = 1.17$ has been taken from Köylü et al. (1995) and the values of K_{LW} and D_f have been calculated from a log-log plot using Equation (2). dp is the mean diameter of the monomers in an aggregate, d_m is the mean mobility diameter (in nm) and M_{CPMA} represents the mean mass of the

particle (in fg) as measured by the CPMA. For D_f the term in parenthesis is the standard error (*S.E.*) calculated from the power fit using Equation (2), for the other quantities, it is the *S.E.* (standard deviation of the mean) and the standard deviation (*S.D.*).

The largest decrease in the mean value of d_p (by 5.6%) after thermodenuding is found for the *N3-D3* set. The decrease in d_p could be due to the partial removal of material volatile at the TD temperature and present on the nascent soot. A decrease in the monomer size after thermal treatment was previously observed when soot samples were heated at higher temperatures (400–900 °C) due to the removal of a part of the nascent PAH layers from the monomers surface (Raj et al. 2014). Also, the mean d_p size, as well as the differences in the mean values of d_p after thermodenuding are smaller for the inverted diffusion flame with respect to those of the McKenna flame. These changes suggest that there was less volatile material present in the nascent soot generated from the inverted flame. This effect could be due to the different type of fuel, as well as different $\emptyset$. In a study of ethylene flame generated soot from a McKenna burner, the size of d_p in thermodenuded soot particles was found larger for higher $\emptyset$ (Slowik et al., 2007). This is consistent with the study by Ghazi and Olfert (2013) that generated soot by an inverted diffusion flame and found no measurable amount of volatile material when the mass was measured after thermodenuding. While, Slowik et al. (2007), using a McKenna flame, found that thermodenuding removed only about 0.05 mass fraction of volatile material for the nascent soot containing 0.1 mass fraction of non-refractory material ($\text{at } \emptyset = 2.1$) from an ethylene flat flame.

To investigate whether the soot aggregates restructured after thermodenuding, we first analyze the changes in D_f as summarized in Fig. 3-4.

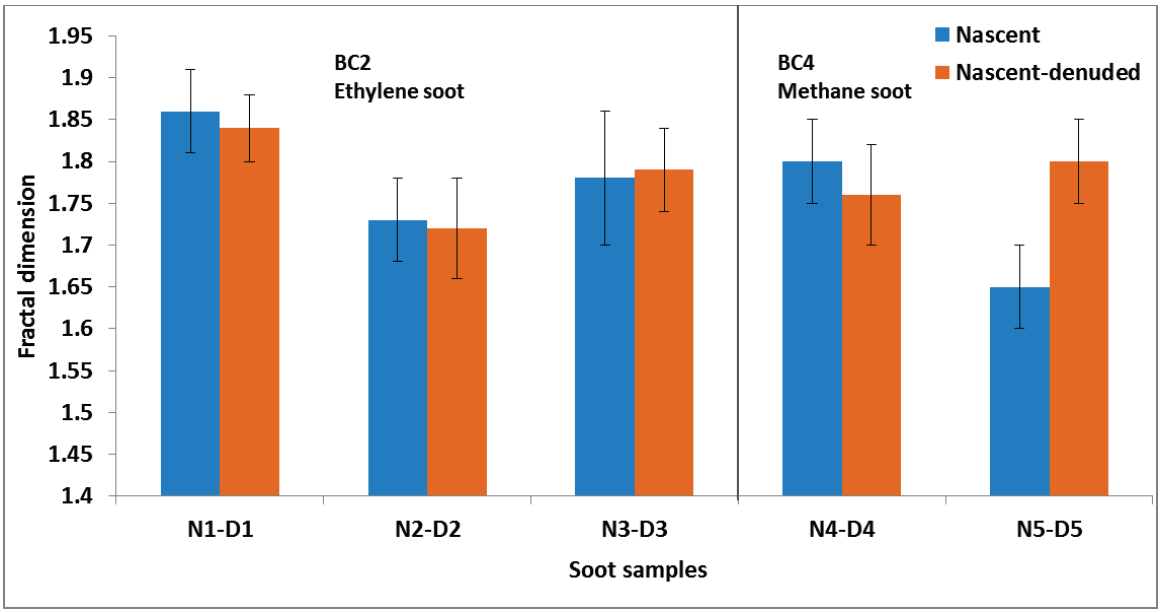

Figure 3-4. Fractal dimension of nascent (in blue) and nascent-denuded (in orange) soot pairs of different mobility sizes. The error bars represent the standard errors.

For all five sample sets, D_f lies between 1.65 and 1.86 (Table 3-1). The derivation of D_f and plots for all of the samples are shown in the supplementary material (Fig. S1). These values of D_f are in agreement with the observations made in previous studies on nascent soot particles produced from different fuel sources (Sorensen, 2001; Dhaubhadel et al., 2006). Also, for all nascent vs. denuded pairs (except for the nascent-oxidized pair: *N5-D5*), there is no significant change (within 1σ) in D_f after thermodenuding (Fig. 4). For the *N5-D5* pair, the D_f changes by about 9% (from 1.65 to 1.80), whereas for all other cases, the change is less than 2.3%. The CPMA data for the BC4 sample shows that the mass decreased from 2.37 to 2.34 fg for nascent soot, while for the nascent-oxidized soot of the same mobility size, the mass decreased from 2.41 to 2.18 fg after thermodenuding. The larger decrease in mass for the nascent oxidized soot suggests that the coating material on the oxidized soot was removed during thermodenuding. A possible explanation for the increase of D_f after thermodenuding the oxidized soot might be that the soot structure was slightly modified during the evaporation of the coating material. Interestingly, for the BC2 soot samples, there is no significant change in D_f despite the significant change in mass (up

to ~29%) of soot after thermodenuding (see CPMA data in Table 3-1). This result suggests that for the BC2 sample sets, the removal of the coating present on nascent soot did not affect the structure of soot. This is most probably due to the chemical composition of the organics that were removed by TD. This result is consistent with the thermodenuding experiment of uncoated soot (fractal soot generated at lower $\emptyset$ = 2.1) by Slowik et al. (2007) that found no change in D_f (derived from mass-mobility relation in their case) after denuding. They suggested that the removal of organics from the uncoated soot during denuding cannot change the skeletal framework of soot. Cross et al. (2010) observed only minor restructuring of soot when dioctyl sebacate coating was removed by thermodenuding, suggesting that the removal of organic coating may have little impact on the restructuring of soot. For soot from a flat flame burner, Slowik et al. (2004) found that the organic carbon (OC) content (mass fraction of 0.1) was composed of a comparable amount of aliphatic and aromatic compounds at a lower $\emptyset$ ($\emptyset = 1.85$), but at a higher $\emptyset$ ($\emptyset > 4$) , the OC content (mass fraction of 0.55) had only a minor fraction of aliphatic compounds. We thus hypothesize that the nascent organics on the soot from the BC2 experiments considered here consisted in a large fraction of aliphatic compounds.

To account for the mass change after thermodenuding on the coating of soot particle, we calculated coating thickness (ΔR_{ve}) in terms of volume equivalent radius (R_{ve}). The difference between the volume equivalent radius of nascent soot and the thermodenuded soot particle was used to estimate the thickness of the coating material. For the case of maximum mass loss (~29%), coating thickness was estimated to be 8.4 nm. (See supplementary material for the calculation).

To further investigate possible morphological changes after thermodenuding, we studied the convexity and roundness of soot particles for all five sample sets. The maximum change in the mean value of roundness occurs for set *N3-D3* (about 18%), followed by the set *N4-D4* (about 13%). For the other sets, the mean value of roundness changes by less than 10%. For the case of convexity, the maximum change in the mean value occurs for set *N4-D4* (about 8%). For all other sets, the mean value of convexity changes by less than 5%. The

larger changes in roundness and convexity for these sample sets are statistically significant (at 1σ) although still minor.

We should point out, however, that image acquisition conditions (e.g., due to different magnifications, scan rates or over/under focusing) and image processing biases (e.g., image thresholding) can introduce additional errors in roundness, convexity, and D_f. In some cases, these errors are larger than the statistical errors provided in Table 3-1. To quantify these uncertainties, we acquired multiple images of six individual particles (from sample *N5*) and processed them under different conditions, as mentioned above. We estimated the uncertainties due to image acquisition and image processing biases in roundness and convexity to be 0.01 and 0.02, respectively. Similarly, uncertainties in N and d_p were estimated to be 16% and 13% (3.4 nm), respectively, which resulted in an error of 0.08 in D_f.

In Fig. 3-5a, b we show box and whisker plots for the convexity and the roundness, respectively of the soot particles before and after thermodenuding. The convexity ranges from 0.37 to 0.91, while the roundness ranges from 0.09 to 0.75 (see Table 3-1 for details). No substantial changes in roundness or convexity are evident after thermodenuding.

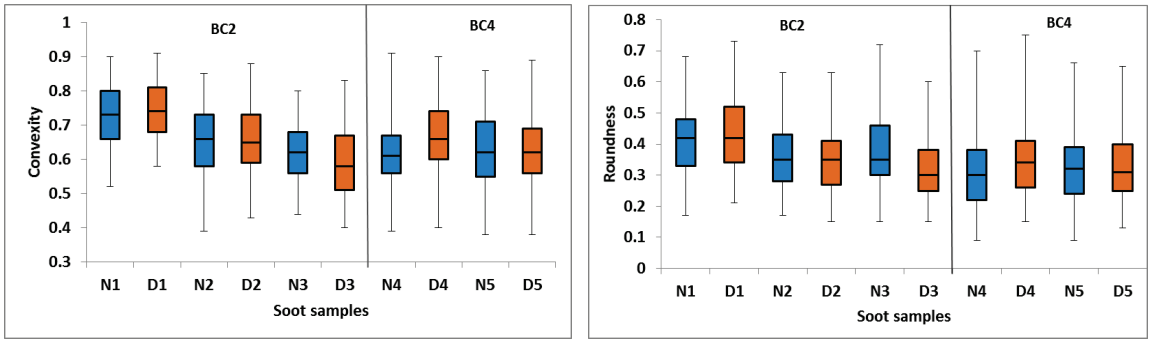

(a) (b)

Figure 3-5. Box and whisker plots of **a**) convexity and **b**) roundness. Blue boxes represent the nascent soot and orange boxes represent the nascent-denuded soot. The horizontal bar inside the box represents the median value while the lower part and upper part of the box separated by the horizontal bar represent the first and third quartiles, respectively. The

lower and upper extremities of the whiskers represent the minimum and maximum values, respectively.

In Fig. 3-6, we show the probability distributions of convexity and roundness for all nascent and denuded soot pairs. The solid and the dashed lines represent the mean values for nascent and denuded soot, respectively, while the shaded color bands in blue and orange represent one standard deviation. These means and uncertainty bands were calculated with a bootstrap approach, resampling with replacement from the raw data and constructing 100,000 frequency distributions (Wilks, 2011).

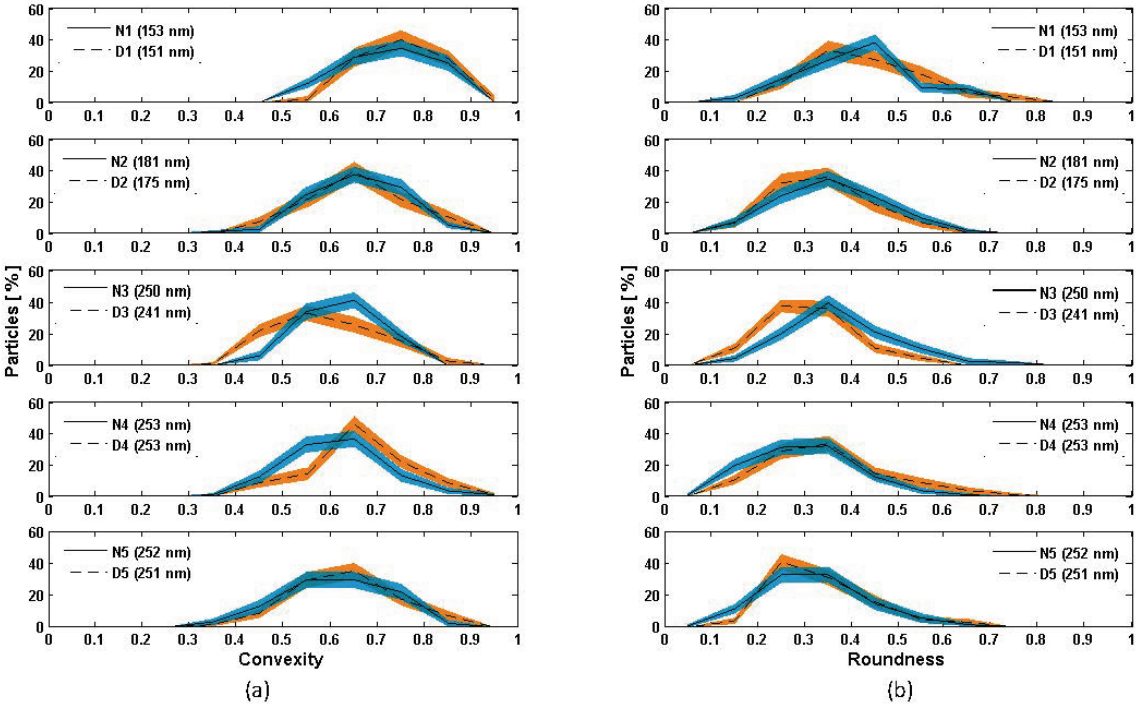

Figure 3-6. Distributions of **a**) convexity and **b**) roundness for nascent and nascent-denuded soot particles of different sizes (the mobility diameter is reported in parenthesis in the legends).

For the *N3-D3* pair, the distribution of convexity and roundness peaks at slightly lower values after thermodenuding. The convexity of particles decreases slightly with the increasing value of the mobility diameter for both nascent and denuded particles. This

suggests that the smaller soot particles are more compact when compared to larger particles, in agreement with previous studies (Chakrabarty, 2006; Virtanen, 2004). Figure 3-6a also suggests that for smaller mobility diameters, the convexity of soot from the ethylene diffusion flame might be less affected by thermodenuding as compared to the larger sized particles. With the methane diffusion flame (*N4-D4* and *N5-D5* sets) particles showed negligible changes in roundness and convexity after thermodenuding, for both nascent and nascent-oxidized soot (Fig. 3-6a *N4-D4* and *N5-D5,* respectively).

For completeness, we also investigated the changes in *AR* and D_{Aeq}. Both show only small changes after thermodenuding (Table 3-1). Our observations on the five sets of soot pairs show only minor changes in the morphology of nascent soot after thermodenuding.

To study the potential effect of PAM on nascent soot prior to thermodenuding, we compared the parameters between *N4* (nascent soot without oxidation in PAM) and *N5* (nascent soot with oxidation in PAM) samples. *N4* and *N5* have comparable masses of 2.37 fg and 2.41 fg, respectively, and a similar mobility diameter ~250 nm. A total of 113 and 122 individual soot particles were analyzed for *N4* and *N5,* respectively. Both samples show nearly the same number of monomers in the soot particles imaged. *N4* has 158 and *N5* has 155 monomers on average. Also, the mean diameter of monomers is similar in the two samples, 23.5 nm for *N4* and 23.9 nm for *N5*. The similar key properties of the soot particles in the two experiments suggest that *N4* and *N5* are suitable samples to make a comparison of nascent soot experiments with and without PAM reactor without thermodenuding.

The roundness for *N4* (0.31) and for *N5* (0.33) and the convexity (0.61 for both *N4* and *N5*) are within the error bars. However, D_f for *N5* (1.65) is smaller than for *N4* (1.80). The value of D_f for *N5* is somehow smaller than the values typically found for nascent soot (1.7–1.9) but lie within the limit when the imaging and thresholding uncertainties discussed above are added in quadrature to the statistical errors. However, in the downstream of the thermodenuder, *D5* and *D4* (samples with and without PAM treatment, respectively) show comparable values of roundness (0.35 for *D4* and 0.33 for *D5*), convexity (0.66 for *D4,*

and 0.63 for *D5*), and D_f (1.76 for *D4* and 1.80 for *D5*). Since we have only one set for the nascent-oxidized soot, we are unable to draw a firm conclusion on the effect of thermodenuding on such particles. Although at the time, we have no clear explanation for the minor difference in D_f, it is possible that the different nanophysical properties of the nascent-oxidized soot might indeed result in a higher sensitivity to thermodenuding.

From a study of young and mature soot particles under high-resolution transmission electron microscopy (HRTEM), Alfè et al. (2009) found no significant difference in the nanostructure of soot monomers. In addition, they found that the change in the H/C ratio is smaller for methane soot when compared to that of other fuels. In another study, Vander Wal and Tomasek (2003) also using HRTEM, reported that the oxidation rate of nascent soot depends upon the nanostructure, for example, the length of graphene segments, curvature, and its orientation. Ishiguro et al. (1991), Song et al. (2006), Müller et al. (2012), also showed a relation between the monomers nanostructure and the soot oxidation from different fuel sources. Other studies showed negligible influence of ozone on soot oxidation (Kaam et al., 1999; Disselkamp et al., 2000), as compared to the OH radical. In another study of soot oxidation (Browne et al., 2015), both the ozone and OH at atmospherically relevant levels were found to have no effect on the oxidation of the elemental carbon (EC) fraction in soot. In our case, the CPMA data showed that the main fraction (>90%) of methane-generated soot consisted of EC, suggesting that the oxidation in the PAM chamber might have a negligible effect on the overall morphology of soot.

In a study on the fragmentation and bond strength of diesel soot, Rothenbacher et al. (2008) made a comparison between nascent soot treated with and without a TD as a function of impact velocity and found no substantial change in the degree of fragmentation of nascent soot aggregates due to the thermodenuding. A low-pressure impactor was used to impart velocities of up to 300 m/s to the soot particles. The TD used in their study had a residence time of 0.43 s, and the sample was heated to 280 °C. In another study by Raj et al. (2014), soot fragmentation was observed after thermodenuding in the temperature range of 400–900 °C on diesel soot and commercial soot (Printex-U). However, in the lower temperature

range, below 500 °C, they found a minor effect on soot fragmentation. Bambha et al. (2013b) noticed only an effect of thermodenuding at 410 °C (transit time of ~34 s) on the morphology of soot during the removal of oleic acid coating. In another study, Slowik et al. (2007) did not observe any measurable change in the structure of soot when fresh soot (generated at $\emptyset$ = 2.1 and 3.5) was thermodenuded at 200 °C. Our results of the negligible or minor restructuring of thermodenuded soot particles are in agreement with these previous studies suggesting that these results are robust and reproducible.

3.5 Conclusions

In this study, we used scanning electron microscopy to investigate the morphology of nascent soot aggregates prior to, and after, thermodenuding in a low-temperature regime (<270 °C). Despite mass losses of up to ~29% in the nascent soot (removal of ~8 nm coating layer from the soot surface), we detected only minor effects on the soot structure after thermodenuding, irrespective of the fuel type and particle size. We observed no significant change in the fractal dimension, although roundness and convexity showed some minor changes in our case. Future work should focus on the effect on the structure of nascent soot of higher thermodenuding temperatures.

Supplementary Materials: The following material is available online at www.mdpi.com/link: a) procedure for the calculation of the coating thickness, b) procedure for the estimate of the fractal dimension, and d) Figure S1: Plots of fractal dimension fits for nascent-denuded soot pairs.

Acknowledgments: This work was supported in part by the Office of Science (BER), Department of Energy (Atmospheric System Research) Grant no. DE-SC0011935 and no. DE-SC0010019, and the Atmospheric Chemistry program of the National Science Foundation Grant no. AGS-1536939 to Boston College, 1537446 to Aerodyne Research Inc. S. China was partially supported by a NASA Earth and Space Science Graduate Fellowships no. NNX12AN97H.

Author Contributions: This manuscript describes the analysis of soot samples obtained in two experimental projects performed in the laboratories of Prof. Paul Davidovits at Boston College. Paul Davidovits and Tim Onasch participated in the planning, setting up and supervising of BC2 and BC4. Adam Ahern and Jason Olfert assisted in the experimental design and the experiments. Tim Onasch and Eben Cross led the BC2 experiments including operation of all experimental aspects of the project and analysis of the SMPS and CPMA data used here. Tim Onasch, Lindsay Wolff and Andrew Lambe led the BC4 experiment including operation of all experimental aspects of the project. Swarup China and Claudio Mazzoleni collected the samples during BC4 and BC2, respectively. Manvendra Dubey participated in the experiments and provided the instrumentation used for sampling during BC2. Janarjan Bhandari and Swarup China performed the SEM analysis. Janarjan Bhandari, Claudio Mazzoleni and Swarup China wrote most of the paper with significant contributions and edits from all the coauthors.

Conflicts of Interest: The authors declare no conflict of interest.

3.6 References

1. Haynes, B.S.; Wagner, H.G. Soot formation. Progress in Energy and Combustion Science 1981, 7, 229-273.

2. Buseck, P.R.; Adachi, K.; Gelencsér, A.; Tompa, É; Pósfai, M. Ns-soot: A material-based term for strongly light-absorbing carbonaceous particles. Aerosol Science and Technology 2014, 48, 777-788.

3. Sorensen, C. Light scattering by fractal aggregates: A review. Aerosol Science and Technology 2001, 35, 648-687.

4. Adachi, K.; Buseck, P. Internally mixed soot, sulfates, and organic matter in aerosol particles from Mexico City. Atmospheric Chemistry and Physics 2008, 8, 6469-6481.

5. Bambha, R.; Dansson, M.A.; Schrader, P.E.; Michelsen, H.A. Effects of volatile coatings on the morphology and optical detection of combustion-generated black carbon particles; Sandia National Laboratories (SNL-CA), Livermore, CA (United States): 2013.

6. China, S.; Salvadori, N.; Mazzoleni, C. Effect of traffic and driving characteristics on morphology of atmospheric soot particles at freeway on-ramps. Environmental science & technology 2014, 48, 3128-3135.

7. Park, K.; Kittelson, D.B.; McMurry, P.H. Structural properties of diesel exhaust particles measured by transmission electron microscopy (tem): Relationships to particle mass and mobility. Aerosol Science and Technology 2004, 38, 881-889.

8. China, S.; Scarnato, B.; Owen, R.C.; Zhang, B.; Ampadu, M.T.; Kumar, S.; Dzepina, K.; Dziobak, M.P.; Fialho, P.; Perlinger, J.A.; Hueber, J.; Helmig, D.; Mazzoleni, L.R.; Mazzoleni, C. Morphology and mixing state of aged soot particles at a remote marine free troposphere site: Implications for optical properties. Geophysical Research Letters 2015, 42, 1243-1250.

9. Cross, E.S.; Onasch, T.B.; Ahern, A.; Wrobel, W.; Slowik, J.G.; Olfert, J.; Lack, D.A.; Massoli, P.; Cappa, C.D.; Schwarz, J.P.; Spackman, J.R.; Fahey, D.W.; Sedlacek, A.; Trimborn, A.; Jayne, J.T.; Freedman, A.; Williams, L.R.; Ng, N.L.; Mazzoleni, C.; Dubey, M.; Brem, B.; Kok, G.; Subramanian, R.; Freitag, S.; Clarke, A.; Thornhill, D.; Marr, L.C.; Kolb, C.E.; Worsnop, D.R.; Davidovits, P. Soot particle studies—instrument inter-comparison—project overview. Aerosol Science and Technology 2010, 44, 592-611.

10. 1Adachi, K.; Chung, S.H.; Buseck, P.R. Shapes of soot aerosol particles and implications for their effects on climate. Journal of Geophysical Research: Atmospheres 2010, 115, D15.

11. China, S.; Mazzoleni, C.; Gorkowski, K.; Aiken, A.C.; Dubey, M.K. Morphology and mixing state of individual freshly emitted wildfire carbonaceous particles. 2013, 4, 2122.

12. Healy, R.M.; Wang, J.M.; Jeong, C.H.; Lee, A.K.Y.; Willis, M.D.; Jaroudi, E.; Zimmerman, N.; Hilker, N.; Murphy, M.; Eckhardt, S.; Stohl, A.; Abbatt, J.P.D.; Wenger, J.C.; Evans, G.J. Light-absorbing properties of ambient black carbon and brown carbon from fossil fuel and biomass burning sources. Journal of Geophysical Research: Atmospheres 2015, 120, 6619-6633.

13. Liu, S.; Aiken, A.C.; Gorkowski, K.; Dubey, M.K.; Cappa, C.D.; Williams, L.R.; Herndon, S.C.; Massoli, P.; Fortner, E.C.; Chhabra, P.S.; Brooks, W.A.; Onasch, T.B.; Jayne, J.T.; Worsnop, D.R.; China, S.; Sharma, N.; Mazzoleni, C.; Xu, L.; Ng, N.L.; Liu, D.; Allan, J.D.; Lee, J.D.; Fleming, Z.L.; Mohr, C.; Zotter, P.; Szidat, S.; Prevot, A.S. Enhanced light absorption by mixed source black and brown carbon particles in uk winter. Nat Commun 2015, 6, 8435.

14. Zhang, R.; Khalizov, A.F.; Pagels, J.; Zhang, D.; Xue, H.; McMurry, P.H. Variability in morphology, hygroscopicity, and optical properties of soot aerosols during atmospheric processing. Proceedings of the National Academy of Sciences 2008, 105, 10291-10296.

15. Adachi, K.; Buseck, P.R. Changes of ns-soot mixing states and shapes in an urban area during calnex. Journal of Geophysical Research: Atmospheres 2013, 118, 3723-3730.

16. Ghazi, R.; Olfert, J.S. Coating mass dependence of soot aggregate restructuring due to coatings of oleic acid and dioctyl sebacate. Aerosol Science and Technology 2013, 47, 192-200.

17. Jacobson, M.Z. Strong radiative heating due to the mixing state of black carbon in atmospheric aerosols. Nature 2001, 409, 695-697.

18. Lack, D.; Cappa, C. Impact of brown and clear carbon on light absorption enhancement, single scatter albedo and absorption wavelength dependence of black carbon. Atmospheric Chemistry and Physics 2010, 10, 4207-4220.

19. Liu, D.; Taylor, J.W.; Young, D.E.; Flynn, M.J.; Coe, H.; Allan, J.D. The effect of complex black carbon microphysics on the determination of the optical properties of brown carbon. Geophysical Research Letters 2015, 42, 613-619.

20. Schnitzler, E.G.; Dutt, A.; Charbonneau, A.M.; Olfert, J.S.; Jäger, W. Soot aggregate restructuring due to coatings of secondary organic aerosol derived from aromatic precursors. Environmental Science & Technology 2014, 48, 14309-14316.

21. Van Poppel, L.H.; Friedrich, H.; Spinsby, J.; Chung, S.H.; Seinfeld, J.H.; Buseck, P.R. Electron tomography of nanoparticle clusters: Implications for atmospheric lifetimes and radiative forcing of soot. Geophysical research letters 2005, 32.

22. Westcott, S.L.; Zhang, J.; Shelton, R.K.; Bruce, N.M.; Gupta, S.; Keen, S.L.; Tillman, J.W.; Wald, L.B.; Strecker, B.N.; Rosenberger, A.T.; Davidson, R.R.; Chen, W.; Donovan, K.G.; Hryniewicz, J.V. Broadband optical absorbance spectroscopy using a whispering gallery mode microsphere resonator. The Review of scientific instruments 2008, 79, 033106.

23. Cappa, C.D.; Onasch, T.B.; Massoli, P.; Worsnop, D.R.; Bates, T.S.; Cross, E.S.; Davidovits, P.; Hakala, J.; Hayden, K.L.; Jobson, B.T.; Kolesar, K.R.; Lack, D.A.; Lerner, B.M.; Li, S.-M.; Mellon, D.; Nuaaman, I.; Olfert, J.S.; Petäjä, T.; Quinn, P.K.; Song, C.; Subramanian, R.; Williams, E.J.; Zaveri, R.A. Radiative absorption enhancements due to the mixing state of atmospheric black carbon. Science 2012, 337, 1078-1081.

24. Fuller, K.A.; Malm, W.C.; Kreidenweis, S.M. Effects of mixing on extinction by carbonaceous particles. Journal of Geophysical Research: Atmospheres 1999, 104, 15941-15954.

25. Khalizov, A.F.; Xue, H.; Wang, L.; Zheng, J.; Zhang, R. Enhanced light absorption and scattering by carbon soot aerosol internally mixed with sulfuric acid. The Journal of Physical Chemistry A 2009, 113, 1066-1074.

26. Bambha, R.P.; Dansson, M.A.; Schrader, P.E.; Michelsen, H.A. Effects of volatile coatings and coating removal mechanisms on the morphology of graphitic soot. Carbon 2013, 61, 80-96.

27. Lack, D.A.; Langridge, J.M.; Bahreini, R.; Cappa, C.D.; Middlebrook, A.M.; Schwarz, J.P. Brown carbon and internal mixing in biomass burning particles. Proceedings of the National Academy of Sciences 2012, 109, 14802-14807.

28. Xue, H.; Khalizov, A.F.; Wang, L.; Zheng, J.; Zhang, R. Effects of coating of dicarboxylic acids on the mass−mobility relationship of soot particles. Environmental Science & Technology 2009, 43, 2787-2792.

29. Huffman, J.A.; Ziemann, P.J.; Jayne, J.T.; Worsnop, D.R.; Jimenez, J.L. Development and characterization of a fast-stepping/scanning thermodenuder for chemically-resolved aerosol volatility measurements. Aerosol Science and Technology 2008, 42, 395-407.

30. Wehner, B.; Philippin, S.; Wiedensohler, A. Design and calibration of a thermodenuder with an improved heating unit to measure the size-dependent volatile fraction of aerosol particles. Journal of Aerosol Science 2002, 33, 1087-1093.

31. Swanson, J.; Kittelson, D. Evaluation of thermal denuder and catalytic stripper methods for solid particle measurements. Journal of Aerosol Science 2010, 41, 1113-1122.

32. Knox, A.; Evans, G.J.; Brook, J.R.; Yao, X.; Jeong, C.H.; Godri, K.J.; Sabaliauskas, K.; Slowik, J.G. Mass absorption cross-section of ambient black carbon aerosol in relation to chemical age. Aerosol Science and Technology 2009, 43, 522-532.

33. Khalizov, A.F.; Lin, Y.; Qiu, C.; Guo, S.; Collins, D.; Zhang, R. Role of oh-initiated oxidation of isoprene in aging of combustion soot. Environmental Science & Technology 2013, 47, 2254-2263.

34. Chow, J.C.; Watson, J.G.; Chen, L.-W.A.; Arnott, W.P.; Moosmüller, H.; Fung, K. Equivalence of elemental carbon by thermal/optical reflectance and transmittance with different temperature protocols. Environmental Science & Technology 2004, 38, 4414-4422.

35. Countess, R.J. Interlaboratory analyses of carbonaceous aerosol samples. Aerosol Science and Technology 1990, 12, 114-121.

36. Cheng, Y.; Duan, F.-k.; He, K.-b.; Zheng, M.; Du, Z.-y.; Ma, Y.-l.; Tan, J.-h. Intercomparison of thermal–optical methods for the determination of organic and elemental carbon: Influences of aerosol composition and implications. Environmental Science & Technology 2011, 45, 10117-10123.

37. Khan, B.; Hays, M.D.; Geron, C.; Jetter, J. Differences in the oc/ec ratios that characterize ambient and source aerosols due to thermal-optical analysis. Aerosol Science and Technology 2012, 46, 127-137.

38. Stanmore, B.R.; Brilhac, J.-F.; Gilot, P. The oxidation of soot: A review of experiments, mechanisms and models. Carbon 2001, 39, 2247-2268.

39. Ebert, M.; Inerle-Hof, M.; Weinbruch, S. Environmental scanning electron microscopy as a new technique to determine the hygroscopic behaviour of individual aerosol particles. Atmospheric Environment 2002, 36, 5909-5916.

40. Ma, X.; Zangmeister, C.D.; Gigault, J.; Mulholland, G.W.; Zachariah, M.R. Soot aggregate restructuring during water processing. Journal of Aerosol Science 2013, 66, 209-219.

41. Torsten, T.; Zsófia, J.; Maria, M.; Roberto, C.; Martin, G.; Maarten, F.H.; Peter, F.D.; Berko, S.; André, S.H.P.; Ernest, W.; Urs, B. Changes of hygroscopicity and morphology during ageing of diesel soot. Environmental Research Letters 2011, 6, 034026.

42. Radney, J.G.; You, R.; Ma, X.; Conny, J.M.; Zachariah, M.R.; Hodges, J.T.; Zangmeister, C.D. Dependence of soot optical properties on particle morphology: Measurements and model comparisons. Environmental Science & Technology 2014, 48, 3169-3176.

43. Swarup, C.; Gourihar, K.; Barbara, V.S.; Noopur, S.; Mikhail, P.; John, E.S.; Jacqueline, W.; Alla, Z.; Duli, C.; Shang, L.; Allison, C.A.; Manvendra, D.; Alexander, L.; Rahul, A.Z.; Claudio, M. Morphology of diesel soot residuals from supercooled water droplets and ice crystals: Implications for optical properties. Environmental Research Letters 2015, 10, 114010.

44. Popovicheva, O.B.; Persiantseva, N.M.; Kuznetsov, B.V.; Rakhmanova, T.A.; Shonija, N.K.; Suzanne, J.; Ferry, D. Microstructure and water adsorbability of aircraft combustor soots and kerosene flame soots: Toward an aircraft-generated soot laboratory surrogate. The Journal of Physical Chemistry A 2003, 107, 10046-10054.

45. Huang, P.-F.; Turpin, B.J.; Pipho, M.J.; Kittelson, D.B.; McMurry, P.H. Effects of water condensation and evaporation on diesel chain-agglomerate morphology. Journal of Aerosol Science 1994, 25, 447-459.

46. Schnitzler, E.G.; Gac, J.M.; Jäger, W. Coating surface tension dependence of soot aggregate restructuring. Journal of Aerosol Science 2017, 106, 43-55.

47. Leung, K.K.; Schnitzler, E.G.; Jäger, W.; Olfert, J.S. Relative humidity dependence of soot aggregate restructuring induced by secondary organic aerosol: Effects of water on coating viscosity and surface tension. Environmental Science & Technology Letters 2017.

48. Weber, A.P.; Baltensperger, U.; Gäggeler, H.W.; Schmidt-Ott, A. In situ characterization and structure modification of agglomerated aerosol particles. Journal of Aerosol Science 1996, 27, 915-929.

49. Weber, A.P.; Friedlander, S.K. In situ determination of the activation energy for restructuring of nanometer aerosol agglomerates. Journal of Aerosol Science 1997, 28, 179-192.

50. Jang, H.D.; Friedlander, S.K. Restructuring of chain aggregates of titania nanoparticles in the gas phase. Aerosol Science and Technology 1998, 29, 81-91.

51. Schmidt-Ott, A. New approaches to in situ characterization of ultrafine agglomerates. Journal of Aerosol Science 1988, 19, 553-563.

52. Chen, C.; Fan, X.; Shaltout, T.; Qiu, C.; Ma, Y.; Goldman, A.; Khalizov, A.F. An unexpected restructuring of combustion soot aggregates by subnanometer coatings of polycyclic aromatic hydrocarbons. Geophysical Research Letters 2016, 43, 11,080-011,088.

53. Rothenbacher, S.; Messerer, A.; Kasper, G. Fragmentation and bond strength of airborne diesel soot agglomerates. Particle and Fibre Toxicology 2008, 5, 9.

54. Lambe, A.; Ahern, A.; Williams, L.; Slowik, J.; Wong, J.; Abbatt, J.; Brune, W.; Ng, N.; Wright, J.; Croasdale, D. Characterization of aerosol photooxidation flow reactors: Heterogeneous oxidation, secondary organic aerosol formation and cloud condensation nuclei activity measurements. Atmospheric Measurement Techniques 2011, 4, 445-461.

55. Lambe, A.; Chhabra, P.; Onasch, T.; Brune, W.; Hunter, J.; Kroll, J.; Cummings, M.; Brogan, J.; Parmar, Y.; Worsnop, D. Effect of oxidant concentration, exposure time, and seed particles on secondary organic aerosol chemical composition and yield. Atmospheric Chemistry and Physics 2015, 15, 3063-3075.

56. Lambe, A.; Ahern, A.; Wright, J.; Croasdale, D.; Davidovits, P.; Onasch, T. Oxidative aging and cloud condensation nuclei activation of laboratory combustion soot. Journal of Aerosol Science 2015, 79, 31-39.

57. Schneider, C.A.; Rasband, W.S.; Eliceiri, K.W. Nih image to imagej: 25 years of image analysis. Nat Meth 2012, 9, 671-675.

58. Forrest, S.; Witten Jr, T. Long-range correlations in smoke-particle aggregates. Journal of Physics A: Mathematical and General 1979, 12, L109.

59. Sorensen, C.; Cai, J.; Lu, N. Light-scattering measurements of monomer size, monomers per aggregate, and fractal dimension for soot aggregates in flames. Applied Optics 1992, 31, 6547-6557.

60. Klein, R.; Meakin, P. Universality in colloid aggregation. Nature 1989, 339, 360-392.Köylü, Ü.Ö.; Faeth, G.; Farias, T.L.; Carvalho, M.d.G. Fractal and projected structure properties of soot aggregates. Combustion and Flame 1995, 100, 621-633.

61. Oh, C.; Sorensen, C.M. The effect of overlap between monomers on the determination of fractal cluster morphology. Journal of Colloid and Interface Science 1997, 193, 17-25.

62. Raj, A.; Tayouo, R.; Cha, D.; Li, L.; Ismail, M.A.; Chung, S.H. Thermal fragmentation and deactivation of combustion-generated soot particles. Combustion and Flame 2014, 161, 2446-2457.

63. 6Slowik, J.G.; Cross, E.S.; Han, J.-H.; Kolucki, J.; Davidovits, P.; Williams, L.R.; Onasch, T.B.; Jayne, J.T.; Kolb, C.E.; Worsnop, D.R. Measurements of morphology changes of fractal soot particles using coating and denuding experiments: Implications for optical absorption and atmospheric lifetime. Aerosol Science and Technology 2007, 41, 734-750.

64. Dhaubhadel, R.; Pierce, F.; Chakrabarti, A.; Sorensen, C. Hybrid superaggregate morphology as a result of aggregation in a cluster-dense aerosol. Physical Review E 2006, 73, 011404.

65. Slowik, J.G.; Stainken, K.; Davidovits, P.; Williams, L.R.; Jayne, J.T.; Kolb, C.E.; Worsnop, D.R.; Rudich, Y.; DeCarlo, P.F.; Jimenez, J.L. Particle morphology and density characterization by combined mobility and aerodynamic diameter measurements. Part 2: Application to combustion-generated soot aerosols as a function of fuel equivalence ratio. Aerosol Science and Technology 2004, 38, 1206-1222.

66. Wilks, D.S. Statistical methods in the atmospheric sciences. Academic press: 2011; Vol. 100.

67. Chakrabarty, R.K.; Moosmüller, H.; Arnott, W.P.; Garro, M.A.; Walker, J. Structural and fractal properties of particles emitted from spark ignition engines. Environmental science & technology 2006, 40, 6647-6654.

68. Virtanen, A.K.K.; Ristimäki, J.M.; Vaaraslahti, K.M.; Keskinen, J. Effect of engine load on diesel soot particles. Environmental Science & Technology 2004, 38, 2551-2556.

69. Alfè, M.; Apicella, B.; Barbella, R.; Rouzaud, J.-N.; Tregrossi, A.; Ciajolo, A. Structure–property relationship in nanostructures of young and mature soot in premixed flames. Proceedings of the Combustion Institute 2009, 32, 697-704.

70. Vander Wal, R.L.; Tomasek, A.J. Soot oxidation: Dependence upon initial nanostructure. Combustion and Flame 2003, 134, 1-9.

71. Ishiguro, T.; Suzuki, N.; Fujitani, Y.; Morimoto, H. Microstructural changes of diesel soot during oxidation. Combustion and Flame 1991, 85, 1-6.

72. Song, J.; Alam, M.; Boehman, A.L.; Kim, U. Examination of the oxidation behavior of biodiesel soot. Combustion and Flame 2006, 146, 589-604.

73. Müller, J.-O.; Frank, B.; Jentoft, R.E.; Schlögl, R.; Su, D.S. The oxidation of soot particulate in the presence of no2. Catalysis Today 2012, 191, 106-111.

74. Kamm, S.; Möhler, O.; Naumann, K.-H.; Saathoff, H.; Schurath, U. The heterogeneous reaction of ozone with soot aerosol. Atmospheric Environment 1999, 33, 4651-4661.

75. Disselkamp, R.S.; Carpenter, M.A.; Cowin, J.P.; Berkowitz, C.M.; Chapman, E.G.; Zaveri, R.A.; Laulainen, N.S. Ozone loss in soot aerosols. Journal of Geophysical Research: Atmospheres 2000, 105, 9767-9771.

76. Browne, E.C.; Franklin, J.P.; Canagaratna, M.R.; Massoli, P.; Kirchstetter, T.W.; Worsnop, D.R.; Wilson, K.R.; Kroll, J.H. Changes to the chemical composition of soot from heterogeneous oxidation reactions. The Journal of Physical Chemistry A 2015, 119, 1154-1163.

4 Chapter 4: Optical properties and radiative forcing of fractal-like tar ball aggregates from biomass burning[3]

4.1 Abstract

Tar balls are frequently found in slightly aged biomass burning plumes. They are spherical in shape, have diameters between ~100 and 300 nm, are amorphous and composed mostly of oxygen and carbon. Tar balls are light absorbing and considered to be a component of brown carbon. Tar balls have been typically reported and analyzed as individual spheres; however, in a recent study, we reported the presence of significant fractions of fractal-like tar ball aggregates in fire plumes from different geographical locations. Aggregation affects the optical properties of particles; therefore, we use T-Matrix and Lorenz-Mie simulations to explore the effects of aggregation on the tar balls' optical properties in the 350–1150 nm wavelength range. We also evaluate the effects of different index of refraction values available from the literature, different monomer numbers, and monomer sizes, as these are key factors determining the aggregates optical properties. Furthermore, we estimate the direct radiative forcing for low and high surface albedos. The single scattering albedo of aggregates exceed by up to 77% that of individual tar balls. The hemispherical upscatter fraction of tar ball aggregates are more than 100% larger than for individual tar balls in many cases. The top of the atmosphere simple forcing efficiency over dark surfaces shows large variabilities with differences up to ~53% between the tar ball aggregates and individual tar balls. These results demonstrate that aggregation of tar balls can have a significant impact on their optical properties and radiative forcing.

4.2 Introduction

Biomass Biomass burning releases large amounts of carbonaceous aerosol in the atmosphere (Bond et al., 2004;Einfeld et al., 1991). The properties of carbonaceous aerosol

[3] The material in this chapter has been recommended for publication by the reviewers in the '*Journal of Quantitative Spectroscopy and Radiative Transfer'* after making a minor revision.

from biomass burning depend upon parameters such as fuel type and moisture content, plume age, and combustion conditions (Reid et al., 2004;Martins et al., 1998). Carbonaceous aerosol emitted by low-temperature combustions (during the smoldering phase) can result in the formation of abundant spherical particles, primarily composed of organic carbon (OC). On the contrary, high-temperature combustions (during the flaming phase) produce a large fraction of soot, fractal-like aggregates of carbonaceous monomers (Chakrabarty et al., 2006;Martins et al., 1998). Tar balls (TBs) are a specific type of spherical carbonaceous particles, often abundant in slightly aged (minutes to hours) biomass burning plumes (Chakrabarty et al., 2010;Pósfai et al., 2003;Pósfai et al., 2004;China et al., 2013;Girotto et al., 2018;Sedlacek III et al., 2018;Adachi and Buseck, 2011). TBs are typically detected using electron microscopy and they are resistant to the electron beam. They generally have a size between ~100 and 300 nm, with an amorphous nanostructure, and they are mostly composed of oxygen and carbon. TBs are found in variable fractions in biomass burning smoke; for example, in a recent study of aged smoke plumes from wildfires, Sedlacek III et al. (2018) found that a significant number fraction of the smoke particles (64%) was made up of TBs. Pósfai et al. (2004) and Hand et al. (2005), reported that up to ~90% of smoke particles from aged plumes were TBs. Similarly, China et al. (2013) and Girotto et al. (2018) found that ~80% of the particles were TBs, based on an analysis of smoke plume samples from different wildfires. In contrast, Adachi and Buseck (2011) found a lower number fraction of TBs (only 14%) in aged smoke plume samples.

Several studies from ambient and laboratory generated samples demonstrated that these TBs can absorb light and affect climate (Adachi and Buseck, 2011;Hand et al., 2005;Hoffer et al., 2016). TBs have been found to be made of high molecular weight organic matter, similar to humic-like substances (Tivanski et al., 2007) with high absorption in the ultraviolet-blue region of the electromagnetic spectrum. Therefore, TBs are often considered to be a component of brown carbon (Laskin et al., 2015 and citations therein); although, in a recent study, Hoffer et al. (2017) found that their laboratory generated TBs were also absorbing light in the red and near infra-red region, in significant amount. The

optical properties of TBs were measured by Hand et al. (2005) who found an ensemble average complex refractive index (RI = $n - ki$) of 1.56 - 0.02i at 632 nm. However, follow-up studies showed a wide spread in the imaginary part (k) of the RI. On one extreme Chakrabarty et al. (2010) found k values down to $k = 0.002$, while on the opposite extreme, Alexander et al. (2008) reported k values up to 0.27, a two-order of magnitude range. Recently, Sedlacek III et al. (2018) found that the optical properties of aerosol measured during the Biomass Burning Observation Project were better simulated when using an intermediate value of the TBs index of refraction ($k = 0.02$).

Alexander et al. (2008) concluded that the absorption cross section (C_{abs}) of a typical TB collected above the Yellow Sea is ~ 5 times larger than that of a typical soot aggregate, based on the relative size and proportion of soot and TBs present in their ambient samples. In another study of an aged plume, Adachi and Buseck (2011) compared the estimated C_{abs} at 550 nm of a single TB with that of a single soot particle and found the ratio to be between 84 and109%. They compared the absorption coefficient of the population of TBs to that of the soot particles (14% and 16% by number, respectively) and found the ratio to be 74-96%. These findings suggest that TBs can be a significant contributor to the light absorption of biomass burning aerosol.

Unlike soot particles, in which monomers are clustered together to form an aggregate (Köylü et al., 1995;Sorensen et al., 1992;Forrest and Witten Jr., 1979), TBs have been typically reported and analyzed as individual spherical particles (Adachi and Buseck, 2011;Hoffer et al., 2016;China et al., 2013;Cong et al., 2010). However, TBs are also found to form aggregates. Some sparse evidence has been reported in the literature; for example, Chakrabarty et al. (2016) found that ~ 60% of analyzed particles from a laboratory smoldering combustion consisted of TB aggregates. Other studies also found TB aggregates consisting of a few monomers (Hand et al., 2005;Hoffer et al., 2016) in ambient samples. In particular, during the analysis of samples from different wildfire plumes, we found an abundant fraction of fractal-like TB aggregates. A significant fraction (27%) of TB aggregates had more than 10 monomers, with some aggregates containing up to 110

monomers. The aggregates were found to follow a scale invariant law, similar to that of soot aggregates (Girotto et al., 2018). At a given wavelength, the optical properties of an aggregate are determined by the monomer size and the monomer number, the structure of the aggregate, and the material index of refraction (China et al., 2015a;Zhang et al., 2008;Cross et al., 2010;Sorensen et al., 1992). For example, light scattering and extinction cross sections by an aggregate change when the number of monomers in the aggregate changes (Mountain and Mulholland, 1988;China et al., 2015b;Dong et al., 2015). Compared to the smaller monomer size of soot (10-50 nm), TBs are larger in size (Pósfai et al., 2004) and the aggregation of such larger particles could significantly change the optical properties of the particle ensemble, and in turn have an effect on their radiative forcing in the atmosphere.

In our previous work (Girotto et al. (2018)), we report a few preliminary simulations of the optical properties of TB aggregates. In the current work, we expand that analysis by carrying out several additional numerical simulations including the dependence of TB aggregates optical and radiative properties on monomer size, monomer number, wavelength, and index of refractions. We use T-Matrix and Lorenz-Mie simulations from 350 nm to 1150 nm. We compare simulations for aggregated with those for non-aggregated particles, acting either as an ensemble of individual TBs, or as a single volume-equivalent spherical particle.

4.3 Method

4.3.1 Simulation of optical properties

We simulated the optical properties of TB aggregates using the superposition T-Matrix approach. With this method, we can obtain the orientation-averaged scattering matrix and the absorption cross section for clusters of spheres (Mackowski, 1994). For this work, we used the Java-based double precision T-Matrix software JaSTA (Java Superposition T-Matrix App) developed by Halder et al. (2014) to generate fractal TB aggregates and to compute their optical properties. Since our microscopy analysis showed TB aggregates

with open structures (with a three-dimensional fractal dimension, $D_{3f} \sim 2$) (Girotto et al., 2018), we followed the ballistic cluster-cluster aggregation approach to generate model lacy aggregates with different numbers of monomers ($N = 8$, 16 and 32), representative of the number of monomers in the TB aggregates reported by Girotto et al. (2018).

For the refractive indices of TBs, we used several different values available in the literature from laboratory and field studies. We list the literature sources of the various RI values, at 550 nm, in Table 4-1. In the case of Hoffer et al. (2016) and Hoffer et al. (2017), TBs were generated by dry distillation of wood samples as described by Tóth et al. (2014), while Chakrabarty et al. (2010) generated TBs from smoldering combustion of dry duffs (Ponderosa pine duff and Alaskan duff) in the laboratory. Alexander et al. (2008) observed TBs in ambient aerosols sampled above the Yellow Sea. We note that the values reported in the literature for the imaginary part of the RI, *k,* span a range of up to two orders of magnitude, even at the same wavelength. In some cases, we had to extrapolate the real and imaginary parts of the reported refractive indices to 550 nm, using power-law fits. We performed sensitivity analyses by varying the monomer numbers ($N = 8$, 16 and 32), at five different wavelengths (350 nm, 550 nm, 750 nm, 950 nm and 1150 nm) at three different monomer diameters. For this purpose, we used the extreme RI values obtained in the study by Alexander et al. (2008) (highest *k* values, corresponding to the A-AA case) and by Chakrabarty et al. (2010) (lowest *k* values, corresponding to the C-AK case in) (Table S1). For Alexander et al. (2008), we extracted the RI values from their plot at the five wavelengths listed above. For Chakrabarty et al. (2010), we calculated the imaginary part of the RI using the fit values given in their paper and using a linear fit for the real part. We assessed the sensitivity of the optical properties to the monomer diameter *D,* by comparing simulations at $D_0 = 150.5$ nm, $D_- = 100.0$ nm and $D_+ = 200.0$ nm. $D_0 = 150.5$ nm is the monomers' geometric mean diameter that we measured on ambient TB aggregates, and D_- and D_+ are close to the lower and upper limit of the measured geometric standard deviation (Girotto et al., 2018).

Because global models typically assume spherical symmetry for the calculation of the aerosol optical properties, we also performed Lorenz-Mie (shorten to "Mie" henceforth) simulations using MiePlot v4600 developed by Laven (2003). For the Mie simulations, we considered two extreme cases: a) a sphere with a radius equal to the volume equivalent radius (VER) of the TB aggregates (Mie_{VER}); and b) *N* spheres (where *N* is the number of monomers in the TB aggregate) of the same size as that of a single monomer, assuming them optically independent from each other (Mie_{N}). In Fig. 4-1, we show a few microscopy images of TB aggregates as an example, and cartoon representations of the particle models used in the T-Matrix and the Mie simulations.

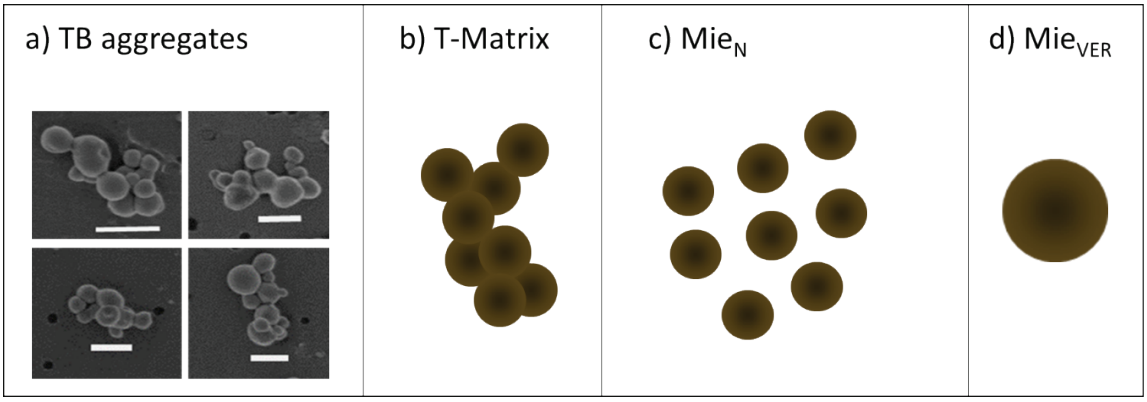

Figure. 4-1a) Collage of SEM images of TB aggregates, the horizontal bar on each image represents a length of 300 nm. Cartoon representation for the particle model used for **b)** T-matrix, **c)** Mie_N, and **d)** Mie_{VER} simulations.

Mie_{VER} simulates the optical properties of a sphere of the same mass as the entire TB aggregate. While Mie_N simulates the optical properties as if the TBs were of the same number to that in the aggregate, but optically independent from each other (i.e., not aggregated). For Mie_N, we obtained the total cross sections by multiplying the absorption cross section (C_{abs}) and the scattering cross section (C_{sca}) of a single monomer by *N*.

Table 4-1. Refractive index values, at 550 nm, from published studies on ambient and laboratory generated TBs and from different fuel types. The last column provides the acronym used in this paper to refer to the different index of refraction cases.

TBs	**RI (*n – ki*)**	**Reference**	**Acronym**
Alaskan duff (laboratory smoldering combustion)	1.74 – 0.002i*	(Chakrabarty et al., 2010)	C-AK
Ponderosa pine duff (laboratory smoldering combustion)	1.87 – 0.006i*		C-PP
European turkey oak (laboratory dry distillation)	1.84 – 0.21i	(Hoffer et al., 2016)	H-EO
Norway spruce (laboratory dry distillation)	1.88 – 0.24i	(Hoffer et al., 2017)	H-NS
Black locust (laboratory dry distillation)	1.86 – 0.25i		H-BL
Ambient aerosol	1.67 - 0.27i	(Alexander et al., 2008)	A-AA

*Extrapolated from the RI values given in Chakrabarty et al. (2010).

4.3.2 Top of the atmosphere radiative forcing by TB aggregates

We further estimated the radiative forcing of TB aggregates at the top of the atmosphere in terms of simple forcing efficiency (SFE), reported in Wg^{-1}, by considering the two extreme cases of the imaginary part of the RI, *k* (C-AK and A-AA from Table 4-1), at two different surface albedos of 0.06 and 0.80, as discussed below. In our calculations, we used the spectral SFE (*dSFE/dλ*) equation (Bond and Bergstrom, 2006;Chen and Bond, 2010;Saliba et al., 2016), which is substantially equivalent to the formulations given by, Haywood and Shine (1995), Chylek and Wong (1995) and (Lenoble et al., 1982):

$$\frac{dSFE}{d\lambda} = -\frac{1}{4}\frac{dS(\lambda)}{d\lambda}T^2(\lambda)(1-C)[2(1-a_s)^2\beta(\lambda)\cdot MSE(\lambda) - 4a_s \cdot MAE(\lambda)], \quad (1)$$

where $\frac{dS(\lambda)}{d\lambda}$ is the extraterrestrial extraterrestrial spectral solar irradiance (in $Wm^{-2}nm^{-1}$), *T* is the atmospheric transmission, *C* is the cloud fraction (assumed here to be equal to 0.6), and a_s is the surface albedo taken as 0.06 for the ocean and 0.80 as an upper value for land (Haywood and Shine, 1995), β is the hemispherical upscatter fraction (section 4.3.3), *MSE* and *MAE* are the mass scattering and the mass absorption efficiencies, respectively. These mass efficiencies are derived from C_{abs} and C_{sca}, which are obtained from numerical simulations (section 4.4.1) and using 1.5 gcm^{-3} as the density for the TBs (Alexander et al., 2008;Sedlacek III et al., 2018). For *T*, we used 0.79, which is the geometric mean value of the wavelength-averaged atmospheric transmission for the upwelling (0.87) and downwelling (0.72) radiation (Penner et al., 1992). Finally, the net top of the atmosphere forcing in the spectral range of 350-1150 nm was calculated by integrating the SFE equation (1) using the solar spectral irradiance at the top of the atmosphere (extraterrestrial) ASTM G173-03 Reference Spectra https://www.nrel.gov/grid/solar-resource/spectra.html. For completeness, we also calculated another parameter relevant to the aerosol radiative forcing, the single scattering albedo ($SSA = C_{sca}/[C_{sca}+C_{abs}] = MSE/[MSE+MAE]$).

4.3.3 Calculation of hemispherical upscatter fraction (β)

To calculate the hemispherical upscatter fraction, β, we used the first element of the scattering matrix $S_{11}(\theta)$ with the normalization condition given in equation (2), as discussed by Wiscombe and Grams (1976):

$$\frac{1}{2}\int_0^{\pi} S_{11}(\theta)\sin\theta d\theta = 1 \quad (2)$$

where θ is the scattering angle. Then, β is calculated as (e.g., Wiscombe and Grams, 1976;Andrews et al., 2006;Schwartz, 1996):

$$\beta = \int_0^{\pi/2} \beta_{\theta_0} sin\theta_0 \, d\theta_0 \quad (3)$$

where β_{θ_0} represents the fraction of solar radiation scattered toward the upward hemisphere for a solar zenith angle θ_0 (Pandey and Chakrabarty, 2016):

$$\beta_{\theta_0} = \frac{1}{2\pi}\int_{\frac{\pi}{2}-\theta_0}^{\frac{\pi}{2}+\theta_0} S_{11}(\theta)\sin\theta \, cos^{-1}(cot\theta_0 \, cot\theta)d\theta + \frac{1}{2}\int_{\frac{\pi}{2}+\theta_0}^{\pi} S_{11}(\theta)sin\theta d\theta \quad (4)$$

Other related and commonly used parameters such as the backscatter fraction (b) and the asymmetry parameter (g) were also calculated, and are discussed in the SI; however, here we focus only on β.

4.4 Results and discussion

4.4.1 Absorption, scattering and single scattering albedo

First, we present the simulation results for C_{sca}, C_{abs}, and SSA for the different cases mentioned in section 4.3.1.

4.4.1.1 Effects of monomer number and refractive index

In Fig. 4-2, we compare C_{sca}, C_{abs}, and SSA for TB aggregates calculated with T-Matrix to the Mie simulations, for D = 150.5 nm at 550 nm. The data points are arranged from left

to right, with increasing imaginary part of the refractive index. In the following figures, the blue, red, and green colors always indicate T-Matrix, Mie_{N} and Mie_{VER}, respectively, while the size of the circles indicates the number of monomers (N = 8, 16 and 32). The Mie_{VER} simulations for N = 8, 16 and 32 corresponds to volume equivalent spheres of radius 150.50 nm, 189.62 nm and 238.90 nm, respectively.

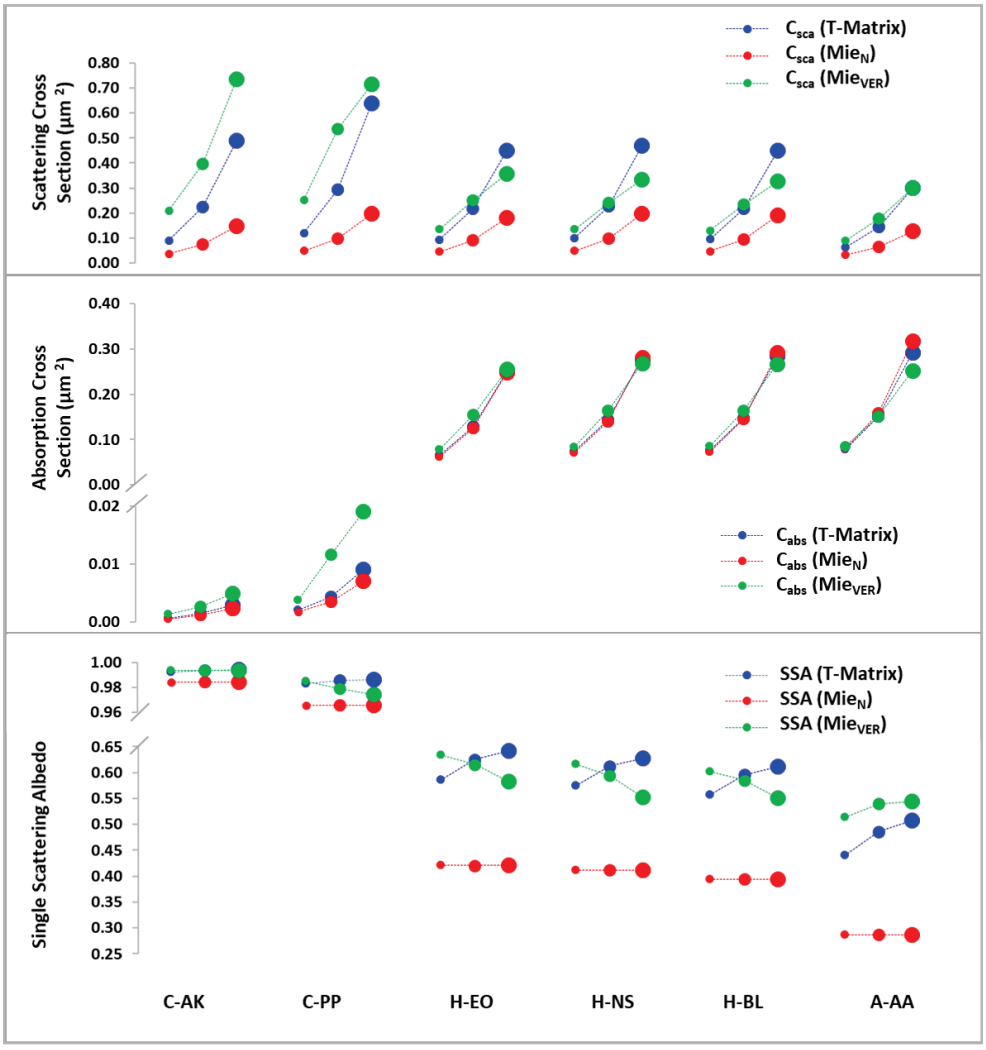

Figure 4-2. Comparison of scattering cross section, absorption cross section, and single scattering albedo for TB aggregates at 550 nm from T-Matrix and Mie simulations for different index of refractions (see Table 4-1), and for a monomer diameter D = 150.5 nm.

The size of the circles increases for increasing number of monomers in the aggregate (N = 8, 16 and 32). Notice the different y-axis scales.

As one might expect, all the scattering and absorption cross sections increase with increasing N. T-Matrix and Mie_{VER} show higher C_{sca} than Mie_N suggesting that TB aggregates can scatter more than N individual TBs, at this monomer diameter (150.5 nm). Unlike C_{sca}, C_{abs} shows closer values for all three types of simulations, except for the duff cases (C-PP and C-AK). Owing to the smaller k, C-AK and C-PP absorption values are much smaller, compared to the other cases.

The *SSA* simulations show a large spread (from 0.29 to 0.99) for the different cases. This is not surprising, considering the large spread in the k values reported in literature (Table 4-1). The T-Matrix *SSA* values increase with N, implying that scattering increases quicker than absorption. In contrast, Mie_{VER} shows higher *SSA* values for N = 8 and lower *SSA* values for N = 16 and 32, except for A-AA.

4.4.1.2 Wavelength dependence

We now present the dependence of C_{sca} and C_{abs} on the wavelength (from 350 to 1150 nm with 200 nm steps), and for different monomer numbers (N = 8, 16 and 32) for the C-AK and A-AA cases (Fig. 4-3). C_{sca} and C_{abs} increase with increasing N while C_{sca} and C_{abs} decrease with increasing wavelength, for most cases. For longer wavelengths, C_{abs} is highest for Mie_{VER} for all the aggregate sizes. For C-AK, TBs show higher C_{sca} and C_{abs} with increasing monomer number, except for C_{sca} at 350 nm owing to the strong wavelength dependence of k resulting in a rapidly increasing absorption at shorter wavelengths.

The *SSA* values are higher for Mie_{VER} compared to T-Matrix and Mie_N for all wavelengths and aggregate sizes (except at 350 nm) and the discrepancy generally increases for larger volume equivalent radii. For C-AK, the *SSA* value for Mie_{VER} decreases drastically with monomer number (and therefore, volume equivalent size) at 350 nm.

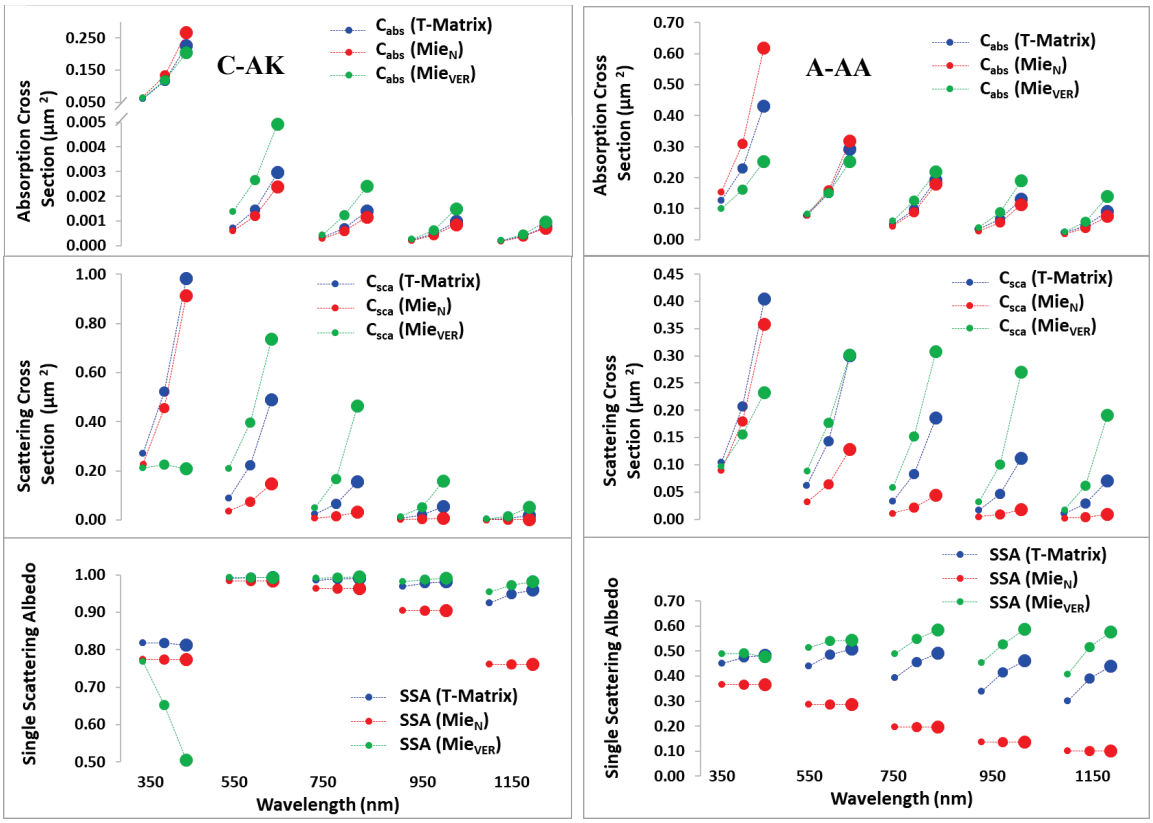

Figure 4-3. Comparison of absorption cross section, scattering cross section, and single scattering albedo for T-Matrix and Mie simulations for the TBs from the Alaskan-duff (C-AK) and the ambient (A-AA) cases, at different wavelengths. The size of the circles increases for increasing number of monomers (N = 8, 16 and 32).

4.4.1.3 Monomer diameter dependence

As mentioned earlier, we performed C_{sca}, C_{abs} and SSA simulations at 550 nm for three different monomer diameters (D): 1) a lower limit D_- = 100.0 nm, 2) a value at the geometric mean D_0 = 150.5 nm, and 3) an upper limit D_+ = 200.0 nm; this range was selected because it is close to the measured values (Girotto et al., 2018). The simulations were performed for the maximum and the minimum values of k for the C-AK and A-AA cases (Fig. 4-4).

As expected, the C_{abs} increases for larger D, for both C-AK and A-AA cases and for each monomer diameter, C_{abs} increases for higher N. For the smallest monomer diameter (D = 100.0 nm), C_{abs} for the Mie_{VER} is the highest, while the T-Matrix C_{sca} is larger for the largest D (200.0 nm) and N (32).

Like C_{abs}, C_{sca} increases with increasing D for all simulations. For the C-AK case, Mie_{VER} C_{abs} is the highest, while for the A-AA case, Mie_{N} C_{abs} is the highest when the monomer diameter is the largest (D = 200.0 nm), irrespective of N.

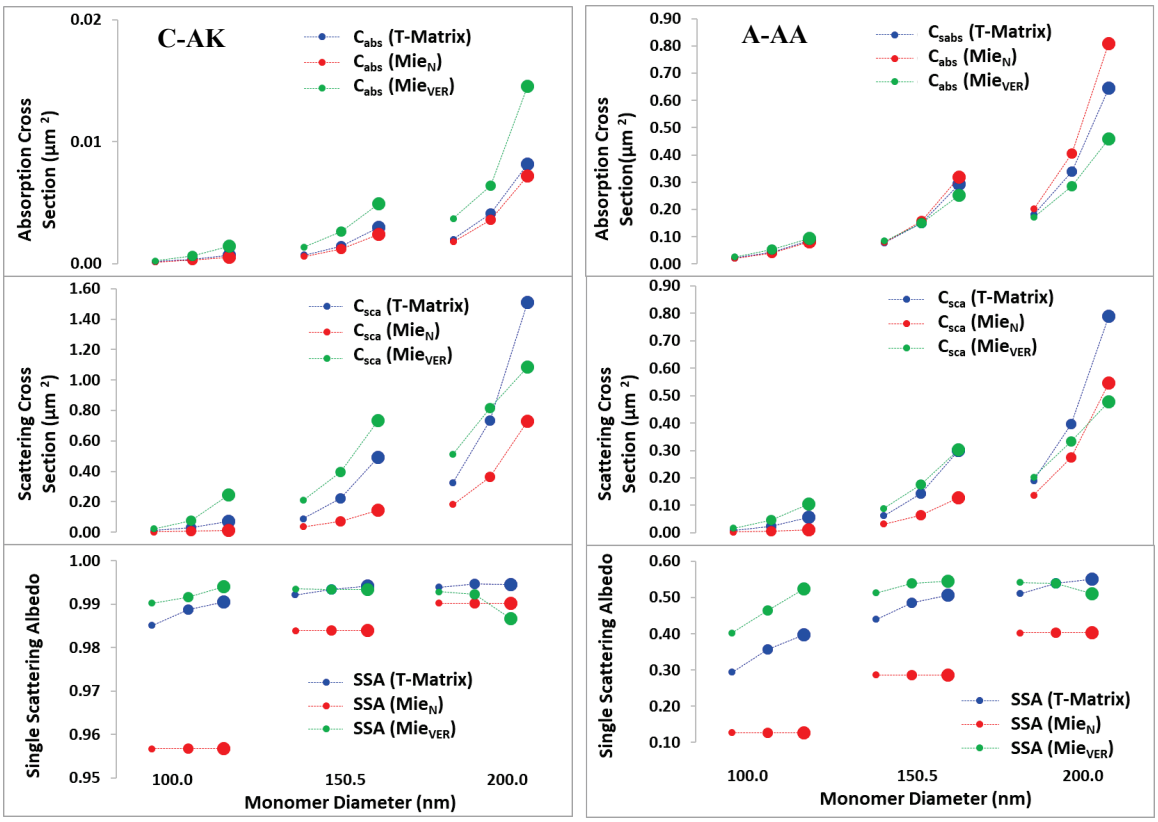

Figure 4-4. Comparison of scattering and absorption cross section, and SSA of TBs at 550 nm between the T-Matrix and the Mie simulations for the C-AK and A-AA cases at three different monomer diameters. The size of the circles increases for increasing number of monomers (N = 8, 16 and 32).

The *SSA* in general increases with increasing *D* for the T-Matrix and Mie_N simulations. However, the *SSA* for Mie_{VER} decreases for the largest *N* and *D*. For C-AK, *SSA* is close to unity (> 0.95 up to 0.99). The *SSA* for A-AA varies from a minimum of 0.13 (Mie_N) to a maximum of 0.55 (T-Matrix). This dynamic range shows that for highly absorbing TB aggregates the size of the TBs making up the aggregate can have a strong influence on the aggregate single scattering albedo, and it is probably partially related to the decreasing ratio of the skin depth to the monomer size. We remind the reader that the *k* value for C-AK is much smaller than for A-AA, which accounts for the large differences in SSA.

4.4.2 Hemispherical upscatter fraction

In this section, we present our result for the hemispherical upscatter fraction (β). As mentioned earlier, the results for *b* and *g* are presented in the SI, for interested readers.

4.4.2.1 Effects of monomer number and refractive index on β

The β-values for T-Matrix and Mie_{VER} are very similar, except for the duff, but are considerably smaller than for Mie_N at 550 nm; owing to the general increase of the forward scattering with increasing particle size parameter, implying that β decreases for larger particle sizes (Fig. 4-5).

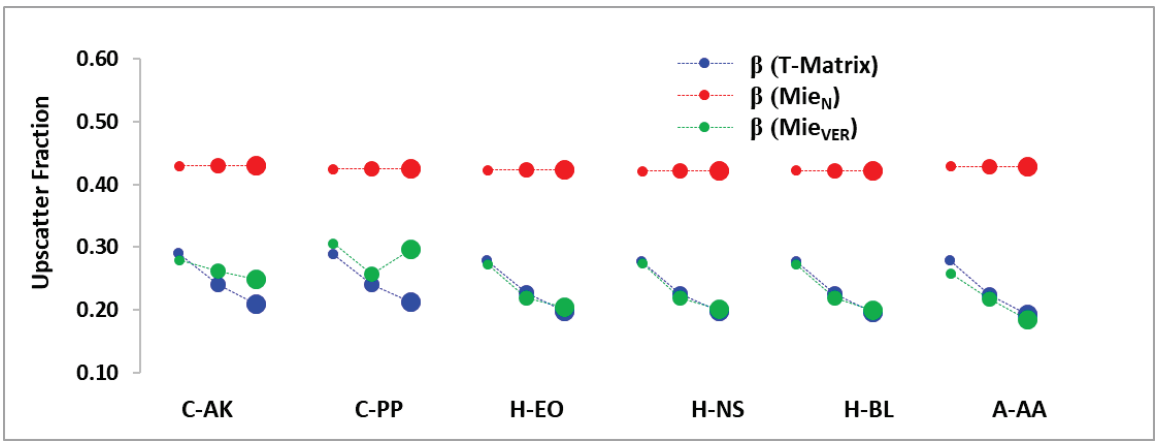

Figure 4-5. Comparison of hemispherical upscatter fraction (β) for T-Matrix and Mie

calculations at 550 nm. The size of the circles increases for increasing number of monomers in the aggregate (N = 8, 16 and 32).

For a given simulation, the β values are similar irrespective of the RI. The exception is the the Mie$_{VER}$ C-PP case for N = 32; the increase in β for that simulation may be due to a Mie resonance at the specific volume equivalent particle size, correspondent to N = 32, and for the given RI and wavelength.

4.4.2.2 Dependence of β on wavelength

We also quantified the increase of β with wavelength for the C-AK and A-AA (Fig. 4-6). The T-Matrix β values are lower than Mie$_{VER}$ at wavelengths larger than ~750 nm for both samples. Individual TBs always scatter light more effectively in the upward hemisphere compared to the TB aggregates.

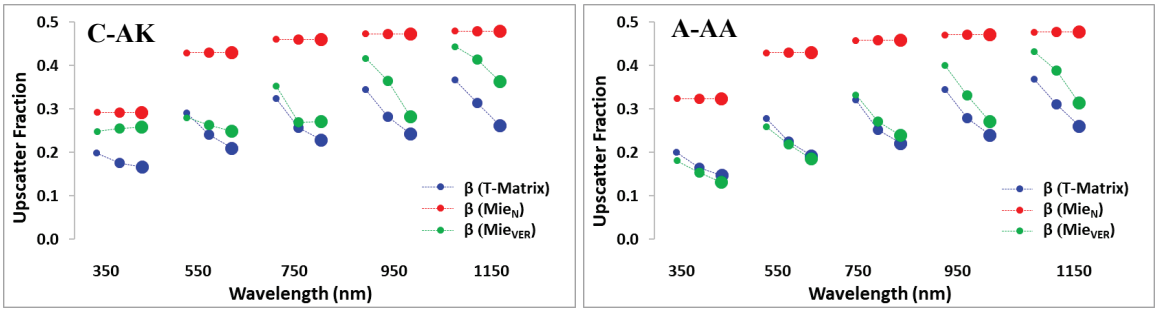

Fig. 4-6. Comparison of hemispherical upscatter fraction (β) for T-Matrix and Mie at different wavelengths for TBs from the C-AK and A-AA cases. The size of the circles increases for increasing number of monomers in the aggregate (N = 8, 16 and 32).

4.4.2.3 Effects of monomer size on β

Finally, we studied the effect of monomer diameter on β. As before, we selected the C-AK and A-AA cases as they represent the extremes of the k values. For both cases, the β values are higher for Mie$_N$ than the Mie-VER and T-Matrix (Fig. 4-7). For A-AA, β decreases when the monomer diameter or the number of monomers increases; but for C-AK, Mie$_{VER}$ β in some cases increases with N.

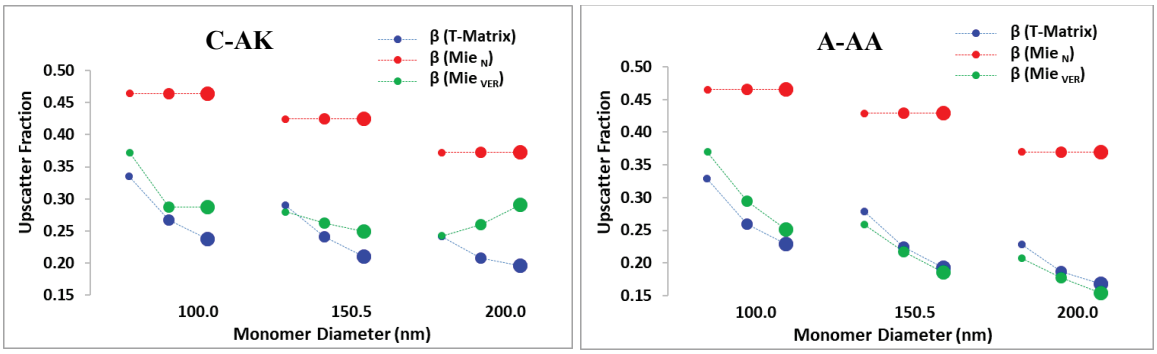

Figure 4-7. Comparison between T-Matrix and Mie simulations of upscatter fraction (β) for TBs at 550 nm for the C-AK and A-AA at different monomer diameters. The size of the circles increases for increasing number of monomers in aggregate (N = 8, 16 and 32).

4.4.3 Top of the atmosphere radiative forcing by TB aggregates

Finally, we present the top of the atmosphere radiative forcing estimates in term of SFE (W g^{-1}) integrating the spectral SFE in the 350-1150 nm spectral region, for two different surface albedos. We calculated the SFE for the C-AK and A-AA cases to estimate the extreme range of radiative forcing by TBs and TB aggregates in the atmosphere.

4.4.3.1 High surface albedo

We estimated the SFE for a surface albedo (a_s) of 0.8, which is representative of highly reflective surfaces, such as snow. The spectral forcing efficiency for the TB aggregates consisting of eight monomers is shown in Fig. 4-8, as an example. The dSFE/dλ values (at 5 nm intervals) are mostly positive and higher for the A-AA (dashed lines) than for the C-AK case (solid lines). For C-AK, the dSFE/dλ decreases steeply from 450 nm to 550 nm, after which it becomes almost constant and oscillates around zero.

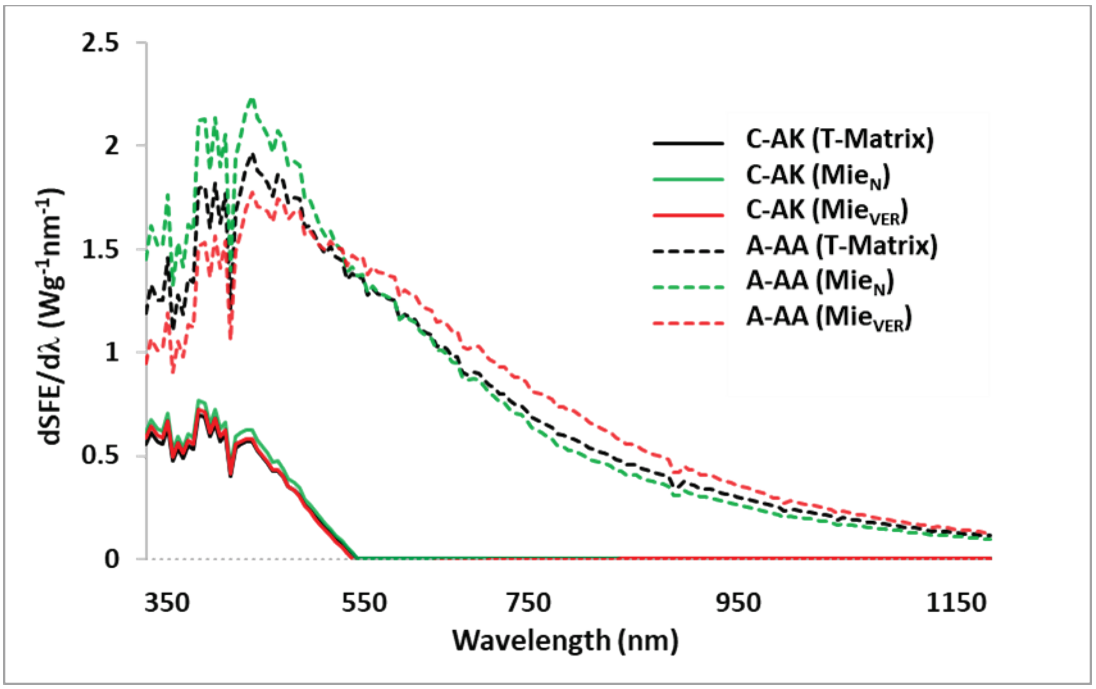

Figure 4-8. Comparison of dSFE/dλ between the T-Matrix and Mie simulations from 350 nm to 1150 nm at high surface albedo ($a_s = 0.8$) and for $N = 8$.

Integrating the curves in Fig. 4-8, we found that for high a_s, the SFE ranges between 69 and 96 Wg^{-1} for C-AK, and between 523 and 646 Wg^{-1} for A-AA. We found that the SFE by TB aggregates is close to the SFE of the volume equivalent single TBs (< 9%) for the A-AA case, but the value differs by more than 15% for the C-AK case. The SFE for TBs for high surface albedo are tabulated in Table S2 in the supplement.

4.4.3.2 Low surface albedo

Finally, we calculated the dSFE(λ)/dλ from 350-1150 nm, for the C-AK and A-AA cases, and for low $a_s = 0.06$, which is representative of highly absorbing surfaces, such as the ocean; an example is shown in Fig. 4-9 for $N = 8$. The dSFE/dλ plots for $N = 16$ and 32 monomers for high and low surface albedos are provided in the SI (see Fig. S4 and S5). Integrating the spectral efficiencies, we found that the SFE is always negative and varies between -89 and -269 Wg^{-1} for the C-AK case, and between -10 and -48 Wg^{-1} for the A-

AA case. The SFE for TBs for low surface albedo are tabulated in Table S3 in the supplement. In the SI (Fig. S6) we also provide plots of dSFE/dλ at 550 nm from all cases for low a_s and high a_s.

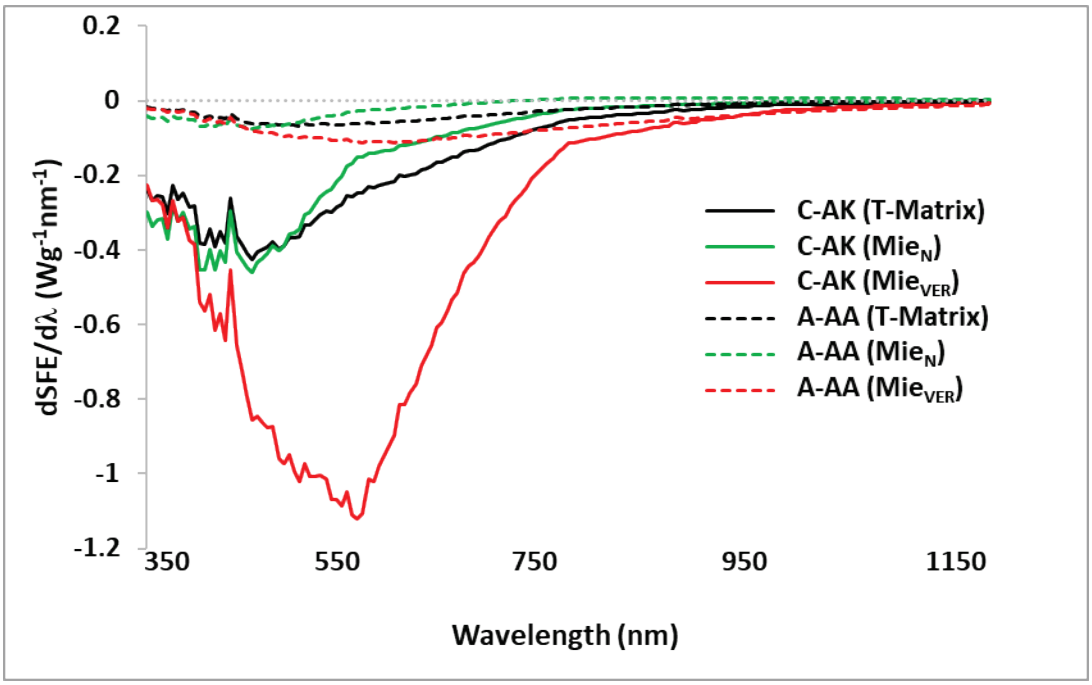

Figure 4-9. Comparison of dSFE/dλ between the T-Matrix and the Mie simulations from 350 nm to 1150 nm at low surface albedo, $a_s = 0.06$, and for $N = 8$.

For comparison, Chakrabarty et al. (2016) estimated mean forcing efficiencies of 20 and 38 Wg^{-1} for brown carbon aerosols from Alaskan peat and Siberian peat, respectively, for a_s = 0.8. In another study on aerosols from wood burning, Chen (2011) reported brown carbon SFE values reaching up to 41 W g^{-1} over bright land surfaces (a_s = 0.8), which is lower than our values (see Table S2). The author also reported a black carbon SFE value of 210 W g^{-1} for $a_s = 0.19$; for comparison, our T-Matrix SFE value is 94 Wg^{-1}, about half of Chen's value, for the A-AA case for $a_s = 0.19$ ($N = 16$). We should caution, that different studies use somewhat different spectral range limits for the integration of dSFE/dλ.

4.5 Summary and Conclusions

Our Because of the large parameter space investigated, we summarized the spread of all the results of our simulations in graphical form in Fig. 4-10, by incorporating all the data points (including the simulation results for different monomer sizes and numbers, different wavelengths and different RI, when applicable) in a single plot. We summarize the relative differences between the different simulations as ratios:

$$RX_{Mie_N}[\%] = \frac{X_{T-Matrix} - X_{Mie_N}}{X_{T-Matrix}}$$

And

$$RX_{Mie_{VER}}[\%] = \frac{X_{T-Matrix} - X_{Mie_{VER}}}{X_{T-Matrix}},$$

where $X_{T-Matrix}$, X_{Mie_N} and $X_{Mie_{VER}}$ represent the scattering or absorption cross section, the *SSA, β* or *SFE,* for the T-Matrix, Mie_N, and Mie_{VER} simulations, respectively.

For the SFE, we simulated only the C-AK and A-AA, cases as discussed earlier in section 4.4.3, which reduces the number of data points. The data points are the relative differences between the integrated SFE values for the TBs from 350 -1150 nm.

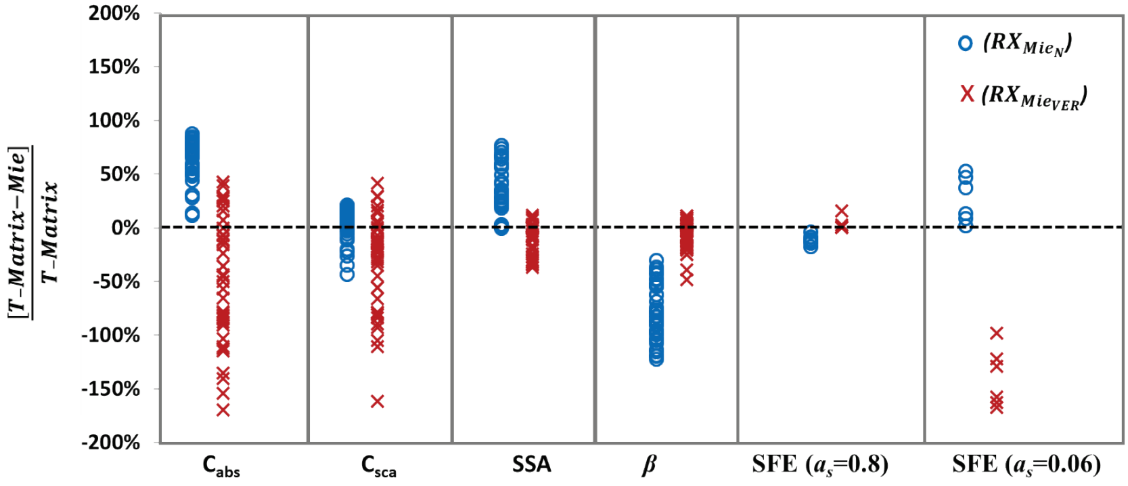

Figure 4-10. Comparison of different parameters between T-Matrix and Mie simulations. The open circles in blue color represent the comparison between the T-Matrix and Mie_N, while the crosses in red color represent the comparison between the T-Matrix and Mie_{VER}. The dashed horizontal line in black color represents zero deviation.

The numerical simulations show that fractal-like TB aggregates have considerably different optical and radiative properties when compared to individual TBs. The broad range of *k* values reported in the literature results in a wide range of values for scattering and absorption cross sections and therefore, for the *SSA* values (from 0.10 to 0.99). Although this issue was not the focus of our current work, these results further underscore the need to narrow the range of RI values, endeavor that should be a subject of future studies. However, when comparing simulations with the same RI, the *SSA* for the aggregates is larger than for individual TBs. The values of *SSA* for the TB aggregates, as calculated using T-Matrix, are different from those calculated using Mie_N by up to 77% and from those calculated from Mie_{VER} by up to 37%. The simulations also show that aggregation has a strong effect on β. TB aggregates always have smaller β values compared to individual TBs. The calculations of the top of the atmosphere SFE show that TB aggregates have different forcing from that of individual TBs. For high surface albedo, the SFE for the volume equivalent Mie model is within ~17% of that calculated from T-matrix.

This finding suggests that, over bright surfaces, Mie simulations might provide reasonable SFE, when one uses the aggregate volume equivalent diameter. However, the relative discrepancy is much larger (up to ~170%) for low surface albedo, suggesting that Mie might not be a good approximation, even when using the volume equivalent model. These findings suggest that aggregation must be considered to accurately assess the influence of TBs on the Earth radiative balance. Accounting for aggregation might be needed also when retrieving aerosol properties from remote sensing measurements and for heating rates calculations, and to correct for potential biases introduced by sampling artifacts that might arise due to their large sizes, all topics that should be further investigated. We note that we purposely performed these comparisons on single particles. Therefore, the results will not reflect necessarily the net effect of a population of particles that might contain different fractions of individual TBs, TB aggregates, soot and organic particles that are often also abundant in biomass burning smoke. Future work should also focus on assessing the relative abundance of these TB aggregates.

Acknowledgments

All the simulation results are freely available in digital commons at the Michigan Tech repository https://digitalcommons.mtu.edu/physics-fp/135/. This work was supported in part by the U.S. Department of Energy, Office of Science (BER), Atmospheric System Research (grant # DE-SC0006941), by a NASA Earth and Space Science Graduate Fellowships (grant # NNX12AN97H) and by the U.S. National Science Foundation (grant # AGS-1110059). We are thankful to the JaSTA team and P. Laven for making the T-matrix App and the Mie-code freely available.

4.6 References

1. Adachi, K., and Buseck, P. R.: Atmospheric tar balls from biomass burning in Mexico, Journal of Geophysical Research: Atmospheres, 116, 2011.

2. Alexander, D. T., Crozier, P. A., and Anderson, J. R.: Brown carbon spheres in East Asian outflow and their optical properties, Science, 321, 833-836, 2008.

3. Andrews, E., Sheridan, P. J., Fiebig, M., McComiskey, A., Ogren, J. A., Arnott, P., Covert, D., Elleman, R., Gasparini, R., and Collins, D.: Comparison of methods for deriving aerosol asymmetry parameter, Journal of Geophysical Research: Atmospheres, 111, 2006.

4. Bond, T. C., Streets, D. G., Yarber, K. F., Nelson, S. M., Woo, J. H., and Klimont, Z.: A technology-based global inventory of black and organic carbon emissions from combustion, Journal of Geophysical Research: Atmospheres, 109, 2004.

5. Bond, T. C., and Bergstrom, R. W.: Light absorption by carbonaceous particles: An investigative review, Aerosol science and technology, 40, 27-67, 2006.

6. Chakrabarty, R., Moosmüller, H., Chen, L.-W., Lewis, K., Arnott, W., Mazzoleni, C., Dubey, M., Wold, C., Hao, W., and Kreidenweis, S.: Brown carbon in tar balls from smoldering biomass combustion, Atmospheric Chemistry and Physics, 10, 6363-6370, 2010.

7. Chakrabarty, R. K., Moosmüller, H., Garro, M. A., Arnott, W. P., Walker, J., Susott, R. A., Babbitt, R. E., Wold, C. E., Lincoln, E. N., and Hao, W. M.: Emissions from the laboratory combustion of wildland fuels: Particle morphology and size, Journal of Geophysical Research: Atmospheres, 111, 2006.

8. Chakrabarty, R. K., Gyawali, M., Yatavelli, R. L., Pandey, A., Watts, A. C., Knue, J., Chen, L.-W. A., Pattison, R. R., Tsibart, A., and Samburova, V.: Brown carbon aerosols from burning of boreal peatlands: microphysical properties, emission factors, and implications for direct radiative forcing, Atmospheric Chemistry and Physics, 16, 3033-3040, 2016.

9. Chen, Y., and Bond, T.: Light absorption by organic carbon from wood combustion, Atmospheric Chemistry and Physics, 10, 1773-1787, 2010.

10. Chen, Y.: Characterization of carbonaceous aerosols from biofuel combustion: emissions and climate relevant properties, University of Illinois at Urbana-Champaign, 2011.

11. China, S., Mazzoleni, C., Gorkowski, K., Aiken, A. C., and Dubey, M. K.: Morphology and mixing state of individual freshly emitted wildfire carbonaceous particles, Nature communications, 4, 2013.

12. China, S., Kulkarni, G., Scarnato, B. V., Sharma, N., Pekour, M., Shilling, J. E., Wilson, J., Zelenyuk, A., Chand, D., and Liu, S.: Morphology of diesel soot residuals from supercooled water droplets and ice crystals: implications for optical properties, Environmental Research Letters, 10, 114010, 2015a.

13. China, S., Scarnato, B., Owen, R. C., Zhang, B., Ampadu, M. T., Kumar, S., Dzepina, K., Dziobak, M. P., Fialho, P., and Perlinger, J. A.: Morphology and mixing state of aged soot particles at a remote marine free troposphere site: Implications for optical properties, Geophysical Research Letters, 42, 1243-1250, 2015b.

14. Chylek, P., and Wong, J.: Effect of absorbing aerosols on global radiation budget, Geophysical research letters, 22, 929-931, 1995.

15. Cong, Z., Kang, S., Dong, S., Liu, X., and Qin, D.: Elemental and individual particle analysis of atmospheric aerosols from high Himalayas, Environmental monitoring and assessment, 160, 323-335, 2010.

16. Cross, E. S., Onasch, T. B., Ahern, A., Wrobel, W., Slowik, J. G., Olfert, J., Lack, D. A., Massoli, P., Cappa, C. D., and Schwarz, J. P.: Soot particle studies—instrument inter-comparison—project overview, Aerosol Science and Technology, 44, 592-611, 2010.

17. Dong, J., Zhao, J., and Liu, L.: Morphological effects on the radiative properties of soot aerosols in different internally mixing states with sulfate, Journal of Quantitative Spectroscopy and Radiative Transfer, 165, 43-55, 2015.

18. Einfeld, W., Ward, D. E., and Hardy, C.: Effects of fire behavior on prescribed fire smoke characteristics: A case study, in: Global biomass burning. Atmospheric, climatic, and biospheric implications, 1991.

19. Forrest, S., and Witten Jr., T.: Long-range correlations in smoke-particle aggregates, Journal of Physics A: Mathematical and General, 12, L109, 1979.

20. Girotto, G., China, S., Bhandari, J., Gorkowski, K., Scarnato, B. V., Capek, T., Marinoni, A., Veghte, D. P., Kulkarni, G., Aiken, A. C., Dubey, M., and Mazzoleni, C.: Fractal-like Tar Ball Aggregates from Wildfire Smoke, Environmental Science & Technology Letters, 10.1021/acs.estlett.8b00229, 2018.

21. Halder, P., Chakraborty, A., Roy, P. D., and Das, H.: Java application for the superposition T-matrix code to study the optical properties of cosmic dust aggregates, Computer Physics Communications, 185, 2369-2379, 2014.

22. Hand, J. L., Malm, W., Laskin, A., Day, D., Lee, T.-b., Wang, C., Carrico, C., Carrillo, J., Cowin, J. P., and Collett, J.: Optical, physical, and chemical properties of tar balls observed during the Yosemite Aerosol Characterization Study, Journal of Geophysical Research: Atmospheres, 110, 2005.

23. Haywood, J., and Shine, K.: The effect of anthropogenic sulfate and soot aerosol on the clear sky planetary radiation budget, Geophysical Research Letters, 22, 603-606, 1995.

24. Hoffer, A., Tóth, A., Nyirő-Kósa, I., Pósfai, M., and Gelencsér, A.: Light absorption properties of laboratory-generated tar ball particles, Atmospheric Chemistry and Physics, 16, 239-246, 2016.

25. Hoffer, A., Tóth, Á., Pósfai, M., Chung, C. E., and Gelencsér, A.: Brown carbon absorption in the red and near infrared spectral region, Atmos. Meas. Tech. Discuss., 2017, 1-14, 10.5194/amt-2016-392, 2017.

26. Köylü, Ü. Ö., Faeth, G., Farias, T. L., and Carvalho, M. d. G.: Fractal and projected structure properties of soot aggregates, Combustion and Flame, 100, 621-633, 1995.

27. Laskin, A., Laskin, J., and Nizkorodov, S. A.: Chemistry of atmospheric brown carbon, Chemical reviews, 115, 4335-4382, 2015.

28. Laven, P.: Simulation of rainbows, coronas, and glories by use of Mie theory, Applied optics, 42, 436-444, 2003.

29. Lenoble, J., Tanre, D., Deschamps, P., and Herman, M.: A simple method to compute the change in earth-atmosphere radiative balance due to a stratospheric aerosol layer, Journal of the Atmospheric Sciences, 39, 2565-2576, 1982.

30. Mackowski, D. W.: Calculation of total cross sections of multiple-sphere clusters, JOSA A, 11, 2851-2861, 1994.

31. Martins, J. V., Hobbs, P. V., Weiss, R. E., and Artaxo, P.: Sphericity and morphology of smoke particles from biomass burning in Brazil, Journal of Geophysical Research: Atmospheres, 103, 32051-32057, 1998.

32. Mountain, R. D., and Mulholland, G.: Light scattering from simulated smoke agglomerates, Langmuir, 4, 1321-1326, 1988.

33. Pandey, A., and Chakrabarty, R. K.: Scattering directionality parameters of fractal black carbon aerosols and comparison with the Henyey–Greenstein approximation, Optics Letters, 41, 3351-3354, 2016.

34. Penner, J. E., Dickinson, R. E., and O'Neill, C. A.: Effects of aerosol from biomass burning on the global radiation budget, Science, 256, 1432-1435, 1992.

35. Pósfai, M., Simonics, R., Li, J., Hobbs, P. V., and Buseck, P. R.: Individual aerosol particles from biomass burning in southern Africa: 1. Compositions and size distributions of carbonaceous particles, Journal of Geophysical Research: Atmospheres, 108, n/a-n/a, 10.1029/2002JD002291, 2003.

36. Pósfai, M., Gelencsér, A., Simonics, R., Arató, K., Li, J., Hobbs, P. V., and Buseck, P. R.: Atmospheric tar balls: Particles from biomass and biofuel burning, Journal of Geophysical Research: Atmospheres, 109, 2004.

37. Reid, J. S., Koppmann, R., Eck, T. F., and Eleuterio, D. P.: A review of biomass burning emissions, part II: Intensive physical properties of biomass burning particles, Atmospheric Chemistry and Physics Discussions, 4, 5135-5200, 2004.

38. Saliba, G., Subramanian, R., Saleh, R., Ahern, A. T., Lipsky, E. M., Tasoglou, A., Sullivan, R. C., Bhandari, J., Mazzoleni, C., and Robinson, A. L.: Optical properties of black carbon in cookstove emissions coated with secondary organic aerosols: Measurements and modeling, Aerosol Science and Technology, 50, 1264-1276, 10.1080/02786826.2016.1225947, 2016.

39. Schwartz, S. E.: The whitehouse effect—Shortwave radiative forcing of climate by anthropogenic aerosols: An overview, Journal of Aerosol Science, 27, 359-382, 1996.

40. Sedlacek III, A. J., Buseck, P. R., Adachi, K., Onasch, T. B., Springston, S. R., and Kleinman, L.: Formation and evolution of Tar Balls from Northwestern US wildfires, Atmospheric Chemistry and Physics, 18, 11289-11301, 2018.

41. Sorensen, C., Cai, J., and Lu, N.: Light-scattering measurements of monomer size, monomers per aggregate, and fractal dimension for soot aggregates in flames, Applied Optics, 31, 6547-6557, 1992.

42. Tivanski, A. V., Hopkins, R. J., Tyliszczak, T., and Gilles, M. K.: Oxygenated interface on biomass burn tar balls determined by single particle scanning transmission X-ray microscopy, The Journal of Physical Chemistry A, 111, 5448-5458, 2007.

43. Tóth, A., Hoffer, A., Nyirő-Kósa, I., Pósfai, M., and Gelencsér, A.: Atmospheric tar balls: aged primary droplets from biomass burning?, Atmospheric Chemistry and Physics, 14, 6669-6675, 2014.

44. Wiscombe, W., and Grams, G.: The backscattered fraction in two-stream approximations, Journal of the Atmospheric Sciences, 33, 2440-2451, 1976.

45. Zhang, R., Khalizov, A. F., Pagels, J., Zhang, D., Xue, H., and McMurry, P. H.: Variability in morphology, hygroscopicity, and optical properties of soot aerosols during atmospheric processing, Proceedings of the National Academy of Sciences, 105, 10291-10296, 2008.

4.7 Supplemental information

Table S1. Refractive index values, at five wavelengths from the ambient TBs measured by Alexander et al. (2008) and the Alaskan duff TBs by Chakrabarty et al. (2010).

Wavelength (nm)	RI (A-AA)	RI (C-AK)
350	1.57 - 0.33900i	1.86 -0.07485i
550	1.67 - 0.27000i	1.74- 0.00187i
750	1.73 - 0.23400i	1.62 - 0.00142i
950	1.76 - 0.20600i	1.50 - 0.00135i
1150	1.79 - 0.17800i	1.38 - 0.00133i

SI section 1: Backscatter fraction (*b*) and asymmetry parameter (*g*) for different refractive indices at 550 nm

Using the first element of the scattering matrix $S_{11}(\theta)$, b and g are calculated as (Wiscombe and Grams, 1976;Andrews et al., 2006;Schwartz, 1996)

$$b = \int_{\frac{\pi}{2}}^{\pi} S_{11}(\theta) \sin\theta \; d\theta \tag{S1}$$

Notice that for the case of zero solar zenith angle, b and β are equal.

$$g = \frac{1}{2}\int_{0}^{\pi} S_{11}(\theta) \sin\theta \; \cos\theta \, d\theta \tag{S2}$$

Like β, the b values for T-Matrix and Mie_{VER} simulations are considerably smaller than those obtained from Mie_{N} (Fig. S1a). However, the T-Matrix values for most cases are higher than the Mie_{VER} values. Also, b values for T-Matrix decrease for increasing aggregate size for all RI, while for Mie_{VER} simulations, b shows increasing trend for N=32.

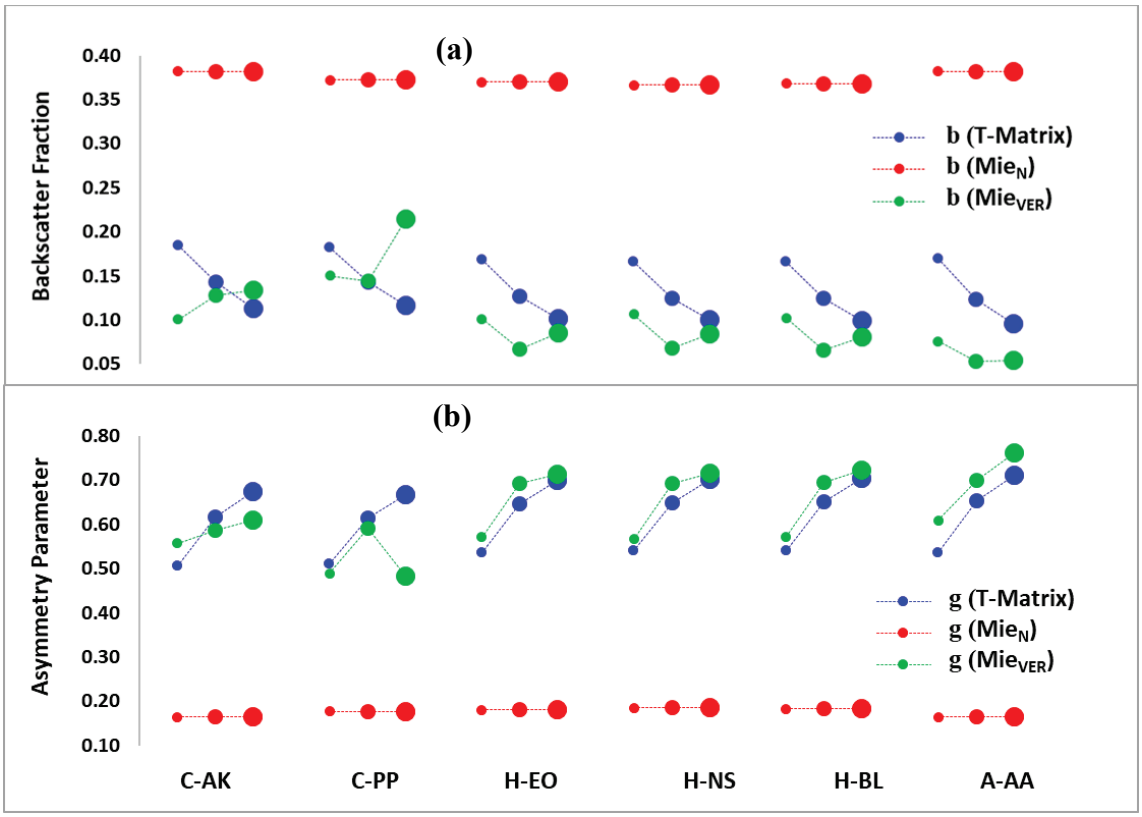

Figure S1. Comparison of **a**) backscatter fraction (b) and **b**) asymmetry parameter (g) between the T-Matrix and Mie calculations. The size of the circles increases for increasing number of monomers in the aggregate (N = 8, 16 and 32).

Finally, we compared g between the T-Matrix and the Mie calculations (Fig. S1b). For both T-Matrix and Mie$_{VER}$ simulations, g increases with N. The only exception being the C-PP and N = 32 case, which may be due to a Mie resonance, as discussed in the main paper. Since g is size-dependent, the values are smaller for the Mie$_N$ compared to the T-Matrix or the Mie$_{VER}$, especially for aggregates with many monomers. Except for the C-AK and C-PP, the Mie$_{VER}$ calculations give higher g compared to the T-Matrix. Overall, g reaches up to 0.72 for TB aggregates while the value lies below 0.20 for the individual TBs, suggesting that the aggregation of TBs can significantly increase g.

SI section 2: Backscatter fraction (*b*) and asymmetry parameter (*g*) at different wavelengths from the C-AK and A-AA cases

Like β, simulations show higher b values at longer wavelengths (Figs. S2a, b) for the TBs from both cases. Simulations show an opposite trend for g where the values decrease with increasing wavelengths (Figs. S2c, d). The g values from Mie_N are lower than Mie_{VER} and T-Matrix.

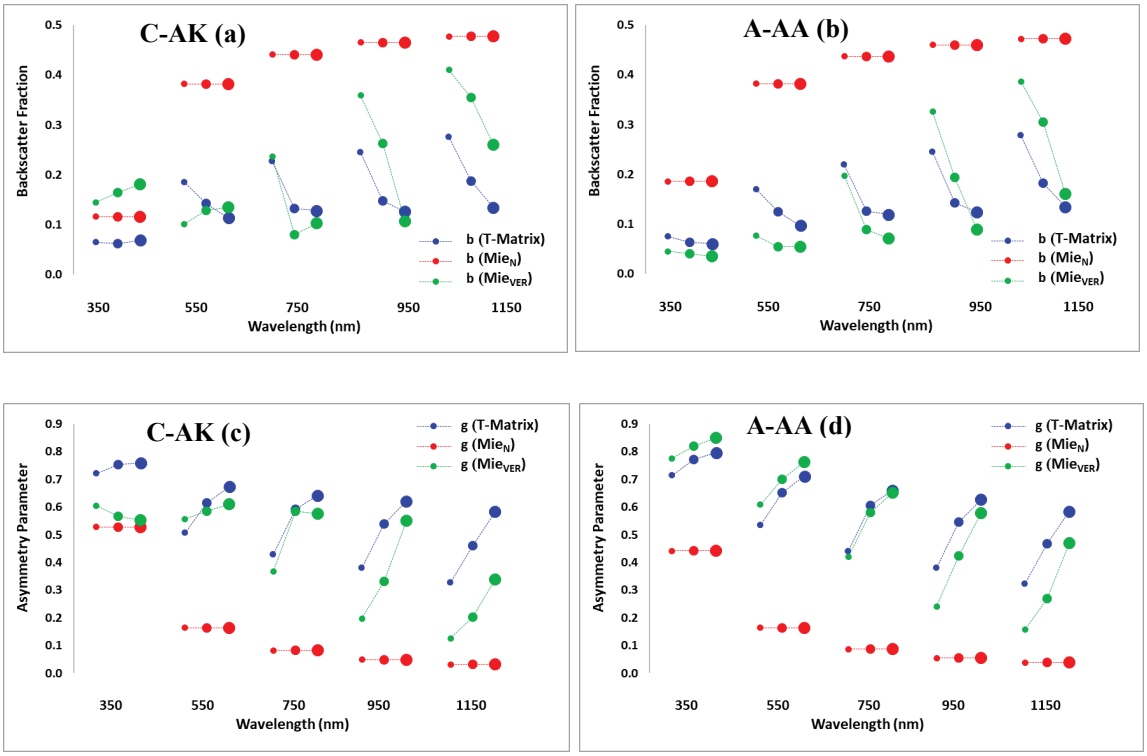

Figure S2. Comparison of **a, b**) backscatter fraction (b) and **c, d**) asymmetry parameter (g) between the T-Matrix and the Mie calculations at different wavelengths for C-AK and A-AA. The size of the circles increases for increasing number of monomers in the aggregate (N = 8, 16 and 32).

SI section 3: Backscatter fraction (*b*) and asymmetry parameter (*g*) at different monomer sizes for the C-AK and A-AA cases

For the Mie_N simulation for both C-AK and A-AA, b decreases with increasing monomer size (Figs. S3a and b, respectively). For the case of Mie_{VER} and T-Matrix simulations for

C-AK, *b* does not show a clear pattern of increase/decrease with *D* or *N*; while for the case of A-AA, the *b* values in general decrease for increasing *D* and *N*.

Regarding the *g* values, they are higher at larger *D* and *N* for both samples for most simulations. For *D* = 200.0 nm, *g* values for Mie_{VER} decreases as *N* increases for the C-AK case. The values of *g* for the Mie_N simulation are always smaller than for the Mie_{VER} and T-Matrix simulations. The plots of *g* for C-AK and A-AS are shown in Figs. S3c and d, respectively.

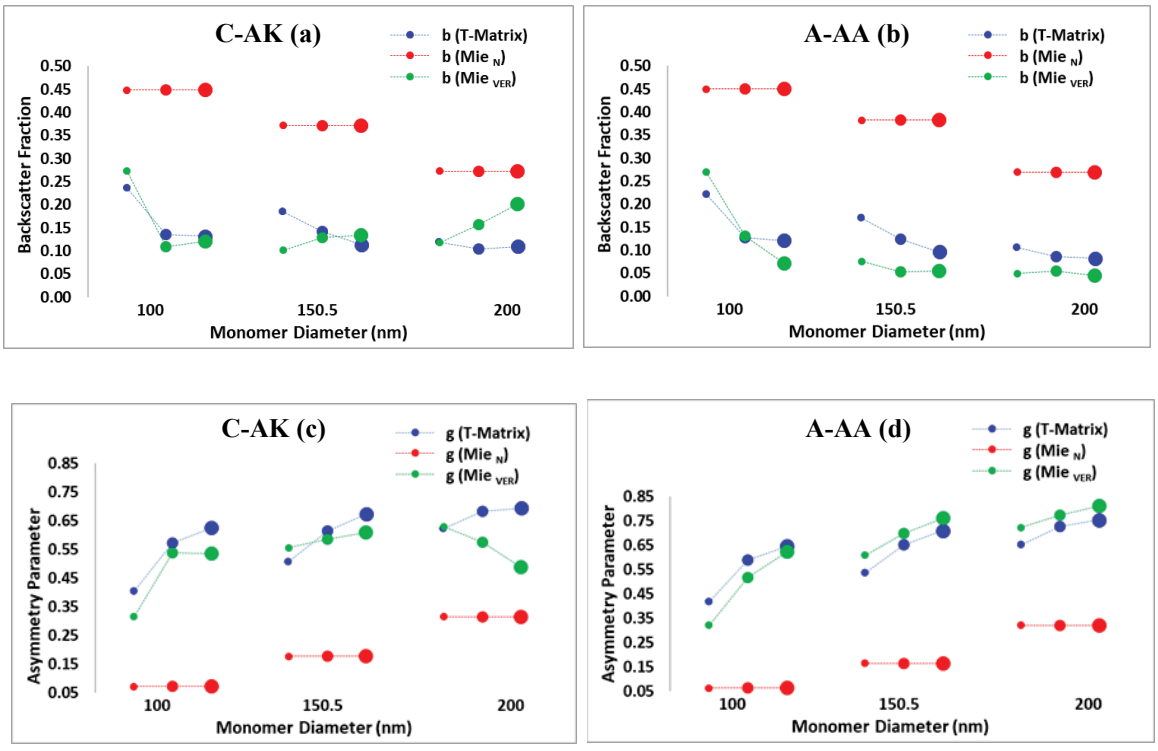

Figure S3. Comparison between T-Matrix and Mie simulations of backscatter fraction (b) and asymmetry parameter (g) at 550 nm for the Alaskan duff (C-AK) case (**Figs. S3a** and **c**, respectively) and the ambient (A-AA) case (**Figs. S3b** and **d**, respectively) at different monomer diameters. The size of the circles increases for increasing number of monomers in aggregate (*N* = 8, 16 and 32).

Our simulations show that both parameters, *b* and *g,* are affected by wavelength, monomer size and aggregate size with a minor effect of the refractive index, which agrees with the previous observations for example Horvath et al. (2016).

SI section 4: Simple forcing efficiency (SFE) *at different wavelength* for the TBs from C-AK and A-AA cases for N = 16, 32 for (*a, c*) high surface albedo and (*b, d*) low surface albedo

The dSFE/dλ plots for the high and low surface albedo for N = 16 and 32 show similar features like those for N = 8.

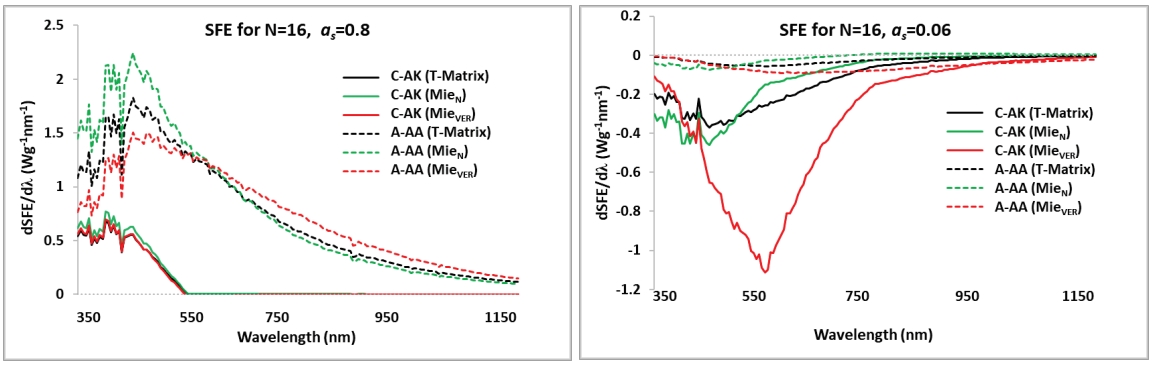

(a) (b)

Figure S4. Comparison between T-Matrix and Mie simulations of dSFE/dλ for TBs at 550 nm for the TBs from Alaskan duff (C-AK) and ambient aerosols (A-AA) for N = 16 for: **a)** a_s = 0.8) and **b)** a_s = 0.06.

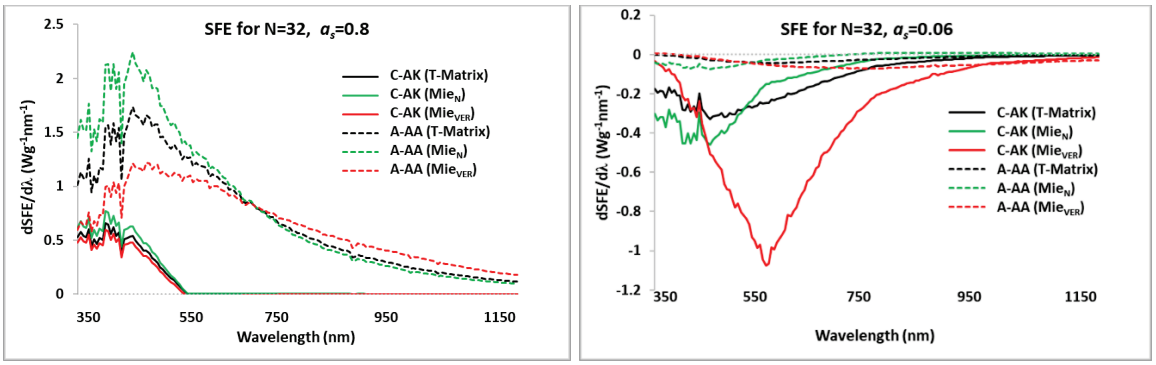

(a) (b)

Figure S5. Same as Fig. S4 but for $N = 32$.

Table S2. SFE (W g^{-1}) from 350- 1150 nm for high surface albedo ($a_s = 0.8$)

N	C-AK			A-AA		
	T-Matrix	Mie$_N$	Mie$_{VER}$	T-Matrix	Mie$_N$	Mie$_{VER}$
8	86.57	95.87	85.58	623.46	646.08	642.28
16	84.10	95.87	81.76	595.95	646.08	599.91
32	81.80	95.87	69.04	574.40	646.08	522.74

Table S3. SFE (W g^{-1}) from 350-1150 nm for low surface albedo ($a_s = 0.06$)

N	C-AK			A-AA		
	T-Matrix	Mie$_N$	Mie$_{VER}$	T-Matrix	Mie$_N$	Mie$_{VER}$
8	-102.34	-88.57	-268.89	-22.17	-10.45	-47.80
16	-96.97	-88.57	-249.64	-19.88	-10.45	-45.16
32	-90.58	-88.57	-242.21	-16.71	-10.45	-36.92

S6. Plots of $\frac{dSFE}{d\lambda}$ at 550 nm for a) high and b) low surface albedo for different RI cases.

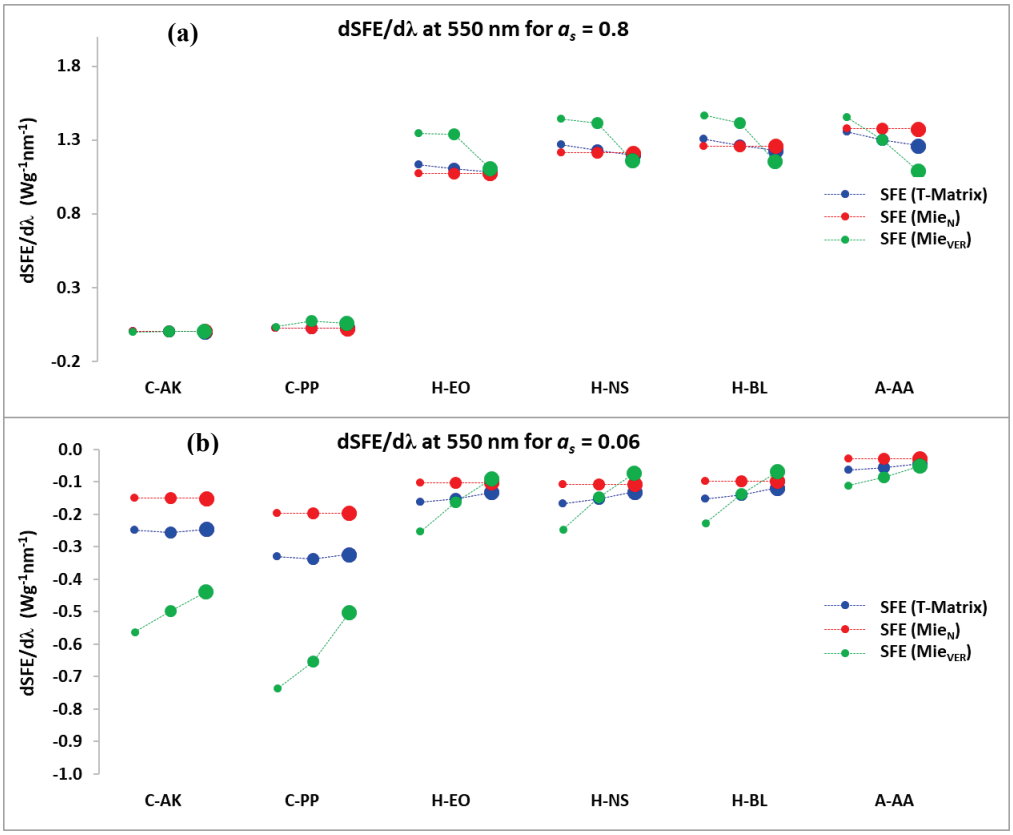

Figure S6. Simple Forcing Efficiency (SFE) at 550 nm. The dashed lines separate the TBs from three different cases

Here, we took the $\frac{dS(\lambda)}{d\lambda}$ value of 1.863 W m^{-2} nm^{-1} at 550 nm from the ASTM G173-03 Reference Spectra and calculated $\frac{dSFE}{d\lambda}$ by using equation (1) in the main document.

References

1. Alexander, D. T., Crozier, P. A., and Anderson, J. R.: Brown carbon spheres in East Asian outflow and their optical properties, Science, 321, 833-836, 2008.

2. Andrews, E., Sheridan, P. J., Fiebig, M., McComiskey, A., Ogren, J. A., Arnott, P., Covert, D., Elleman, R., Gasparini, R., and Collins, D.: Comparison of methods for deriving aerosol asymmetry parameter, Journal of Geophysical Research: Atmospheres, 111, 2006.

3. Chakrabarty, R., Moosmüller, H., Chen, L.-W., Lewis, K., Arnott, W., Mazzoleni, C., Dubey, M., Wold, C., Hao, W., and Kreidenweis, S.: Brown carbon in tar balls from smoldering biomass combustion, Atmospheric Chemistry and Physics, 10, 6363-6370, 2010.

4. Horvath, H., Kasahara, M., Tohno, S., Olmo, F., Lyamani, H., Alados-Arboledas, L., Quirantes, A., and Cachorro, V.: Relationship between fraction of backscattered light and asymmetry parameter, Journal of Aerosol Science, 91, 43-53, 2016.

5. Schwartz, S. E.: The whitehouse effect—Shortwave radiative forcing of climate by anthropogenic aerosols: An overview, Journal of Aerosol Science, 27, 359-382, 1996.

6. Wiscombe, W., and Grams, G.: The backscattered fraction in two-stream approximations, Journal of the Atmospheric Sciences, 33, 2440-2451, 1976.

5 Chapter 5: Research implications and Future Directions

Soot and tar balls are both light absorbing carbonaceous aerosol, the first generated from any combustion process involving carbonaceous material, the second mainly produced during biomass burning. Soot strongly absorbs light and warms our atmosphere, therefore, exerting a positive, but highly uncertain, radiative forcing at the top of the atmosphere. Soot is potentially the second warming agent in the atmosphere after carbon dioxide (Ramanathan and Carmichael, 2008;Jacobson, 2001). The role or light absorbing tar balls is even less understood, also because of large uncertainties in the imaginary part of their index of refraction. However, an additional source of uncertainty that is a common thread for these two types of particles is the complexity in the morphology of soot as well as, TB aggregates, and their mixing with other aerosol and condensable vapors. The morphology and mixing state change over time due to atmospheric processing, and an understanding of their evolution is, therefore, necessary for a full representation in numerical models.

During the last five years of my doctorate studies, I focused my research on the detailed investigation of soot at a single particle level using electron microscopy. Our research can provide radiative transfer modelers with accurate information on the morphology and mixing state of individual particles. Therefore, this information can contribute to reducing the uncertainties in the aerosol radiative forcing.

In one of my research projects, we investigated the morphology of cloud processed soot particles from laboratory and field samples and found that soot particles undergo compaction. Many previous studies speculated that compaction of soot particles was the result of cloud processing (Huang et al., 1994;Mikhailov et al., 2006;China et al., 2015). Our research tested and validated this hypothesis, quantifying the degree of compaction using laboratory as well as ambient data. Compaction of soot directly affects its optical properties. In general, light scattering by soot particles increase upon compaction by large amounts, while absorption can increase or decrease by a few percent (Radney et al., 2014;Liu and Mishchenko, 2005). Soot compaction can also have effects on health. Several

studies have shown that the surface area of inhaled soot plays a key role in determining its toxicity in the lungs (Oberdörster, 2000;Schmid and Stoeger, 2016). Also, compaction affects the particle lung deposition; in fact, fiber-like fresh soot more easily penetrates through the respiratory tract during inhalation compared to compact spherical particles of the same mass (Asbach et al., 2016;Scheckman and McMurry, 2011). A recent study showed that the ability of soot to become ice-nuclei is affected by the availability of pores (mesopores) on its surface (Mahrt et al, 2018). The availability of mesopores is modified upon soot compaction. It has been demonstrated that the molecular roughness of the soot surface directly affects the heterogeneous ice nucleation efficiency (Lupi et al., 2014). Finally, when a lacy soot collapses and become compact, the effective density increases affecting dry deposition rates and the soot atmospheric life time in the atmosphere. All these aspects are interesting topics for future research efforts.

The third chapter of my dissertation explores potential biases introduced by the use of thermodenuders. During atmospheric processing, it is likely that the soot particles are internally mixed with other aerosol or condensable vapors (China et al., 2015). Coating affects how the particle interacts with light, typically enhancing the scattering and absorption cross sections. To calculate the optical enhancements, coatings should be removed and thermodenuders are often used to strip off the coating materials (Cappa et al., 2012;Cross et al., 2010). However, it is assumed that the thermodenuder removes the coating material without disturbing/deforming the backbone structure of the soot core. Our investigation showed that indeed, the structural integrity of soot remains intact after thermodenuding. This finding suggests that the thermodenuding technique itself is not affected by this bias. It should be noted that other biases could affect the enhancement calculation, but those issues were not the focus of our study. During our investigation, we studied the morphology of soot particles that were denuded up to the temperature of 270 0C. We suggest that further investigation at higher temperatures should be carried out in the future. Also, we suggest investigating the thermodenuding effect on core soot structure involving the removal of the high surface tension and low surface tension coating materials to examine whether the surface tension of coating material introduce bias during the

thermodenuding. A future research direction could be that of examining soot morphology changes in the new scanning transmission electron microscope at MTU using an existing temperature controlled heated holder as a “thermodenuder”.

Another important aspect of my research was the study of tar ball aggregates, covered in chapter 4. Fractal aggregates of TBs are present in significant fraction (up to 60% by number) in biomass burning plumes (Chakrabarty et al., 2016;Girotto et al., 2018). We found that TB aggregates exhibit fractal-like morphologies consisting of tens of monomers, similar to that of soot (Girotto et al., 2018). TB aggregation affects the particle optical properties and their direct radiative forcing. To quantitatively study these effects, I used two different numerical methods, T-Matrix and Lorenz-Mie. We found that the correct representation of the TB aggregates morphology is indeed necessary. Future studies should focus on determining the abundance of these aggregates and how the burning conditions and fuel type affect their concentrations. Additionally, their formation mechanisms are currently unknown and should be investigated. Their effects on heating rates and remote sensing retrievals should also be determined. Finally, understanding their aerodynamic properties would be important to understand sampling biases (that arise from their rather large size) and deposition rates.

References

1. Asbach, C., Clavaguera, S., and Todea, A.: Indoor and Outdoor Nanoparticles: Determinants of Release and Exposure Scenarios ed M, Viana (Cham: Springer International Publishing) Measurement Methods for Nanoparticles in Indoor and Outdoor Air, 19-49, 2016.

2. Cappa, C. D., Onasch, T. B., Massoli, P., Worsnop, D. R., Bates, T. S., Cross, E. S., Davidovits, P., Hakala, J., Hayden, K. L., and Jobson, B. T.: Radiative absorption enhancements due to the mixing state of atmospheric black carbon, Science, 337, 1078-1081, 2012.

3. Chakrabarty, R. K., Gyawali, M., Yatavelli, R. L., Pandey, A., Watts, A. C., Knue, J., Chen, L.-W. A., Pattison, R. R., Tsibart, A., and Samburova, V.: Brown carbon aerosols from burning of boreal peatlands: microphysical properties, emission factors, and implications for direct radiative forcing, Atmospheric Chemistry and Physics, 16, 3033-3040, 2016.

4. China, S., Scarnato, B., Owen, R. C., Zhang, B., Ampadu, M. T., Kumar, S., Dzepina, K., Dziobak, M. P., Fialho, P., and Perlinger, J. A.: Morphology and Mixing State of Aged Soot Particles at a Remote Marine Free Troposphere Site: Implications for Optical Properties, Geophysical Research Letters, 2015.

5. Cross, E. S., Onasch, T. B., Ahern, A., Wrobel, W., Slowik, J. G., Olfert, J., Lack, D. A., Massoli, P., Cappa, C. D., and Schwarz, J. P.: Soot particle studies—instrument inter-comparison—project overview, Aerosol Science and Technology, 44, 592-611, 2010.

6. Girotto, G., China, S., Bhandari, J., Gorkowski, K., Scarnato, B. V., Capek, T., Marinoni, A., Veghte, D. P., Kulkarni, G., Aiken, A. C., Dubey, M., and Mazzoleni, C.: Fractal-like Tar Ball Aggregates from Wildfire Smoke, Environmental Science & Technology Letters, 10.1021/acs.estlett.8b00229, 2018.

7. Huang, P.-F., Turpin, B. J., Pipho, M. J., Kittelson, D. B., and McMurry, P. H.: Effects of water condensation and evaporation on diesel chain-agglomerate morphology, Journal of Aerosol Science, 25, 447-459, 1994.

8. Jacobson, M. Z.: Strong radiative heating due to the mixing state of black carbon in atmospheric aerosols, Nature, 409, 695-697, 10.1038/35055518, 2001.

9. Liu, L., and Mishchenko, M. I.: Effects of aggregation on scattering and radiative properties of soot aerosols, Journal of Geophysical Research: Atmospheres, 110, 2005.

10. Lupi, L., Hudait, A., and Molinero, V.: Heterogeneous nucleation of ice on carbon surfaces, Journal of the American Chemical Society, 136, 3156-3164, 2014.

11. Mahrt, F., Marcolli, C., David, R. O., Grönquist, P., Barthazy Meier, E. J., Lohmann, U., and Kanji, Z. A.: Ice nucleation abilities of soot particles determined with the Horizontal Ice Nucleation Chamber, Atmospheric Chemistry and Physics, 18, 13363-13392, 2018.

12. Mikhailov, E., Vlasenko, S., Podgorny, I., Ramanathan, V., and Corrigan, C.: Optical properties of soot–water drop agglomerates: An experimental study, Journal of Geophysical Research: Atmospheres, 111, 2006.

13. Oberdörster, G.: Pulmonary effects of inhaled ultrafine particles, International archives of occupational and environmental health, 74, 1-8, 2000.

14. Radney, J. G., You, R., Ma, X., Conny, J. M., Zachariah, M. R., Hodges, J. T., and Zangmeister, C. D.: Dependence of soot optical properties on particle morphology: measurements and model comparisons, Environmental science & technology, 48, 3169-3176, 2014.

15. Ramanathan, V., and Carmichael, G.: Global and regional climate changes due to black carbon, Nature geoscience, 1, 221-227, 2008.

16. Scheckman, J. H., and McMurry, P. H.: Deposition of silica agglomerates in a cast of human lung airways: Enhancement relative to spheres of equal mobility and aerodynamic diameter, Journal of Aerosol Science, 42, 508-516, 2011.

17. Schmid, O., and Stoeger, T.: Surface area is the biologically most effective dose metric for acute nanoparticle toxicity in the lung, Journal of Aerosol Science, 99, 133-143, 2016.

Appendix


Global Affiliate Network | Search the Commons | Contact |
creative commons
Share your work
Use & remix
What we do
Help us build a vibrant, collaborative global commons
Donate Now

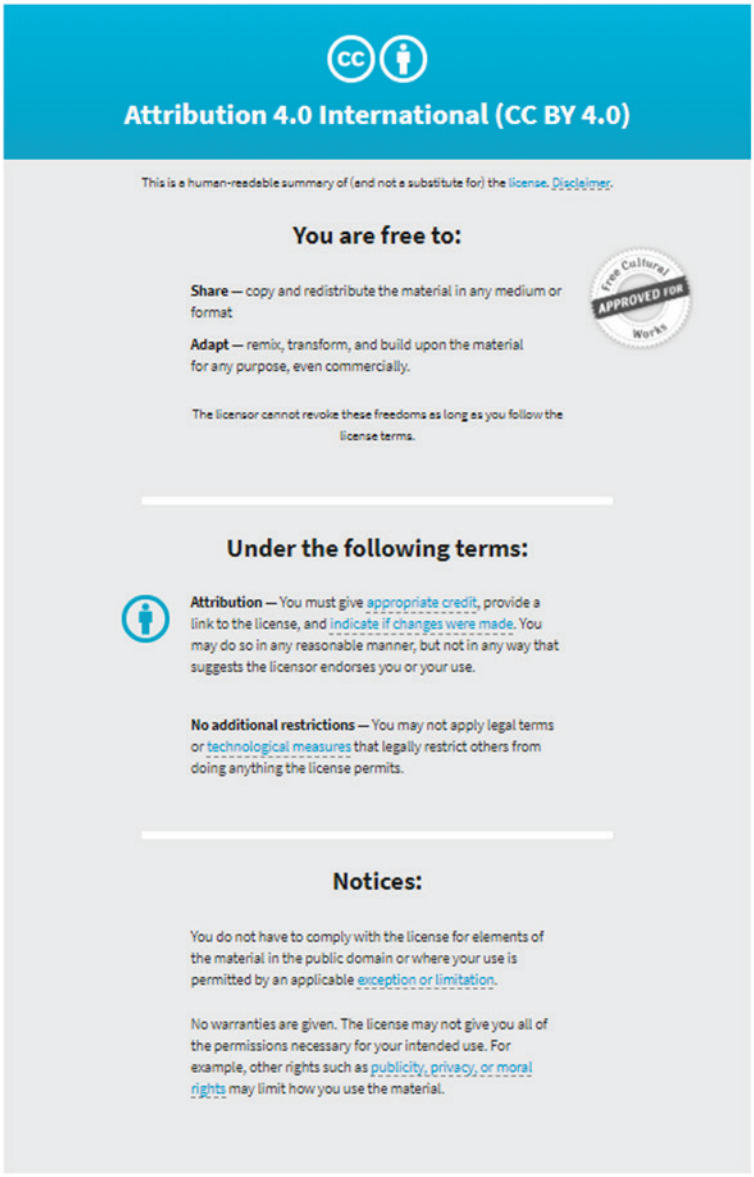
Attribution 4.0 International (CC BY 4.0)
This is a human-readable summary of (and not a substitute for) the license. Disclaimer.
You are free to:
Share — copy and redistribute the material in any medium or format
Adapt — remix, transform, and build upon the material for any purpose, even commercially.
The licensor cannot revoke these freedoms as long as you follow the license terms.
Free Cultural APPROVED FOR Works
Under the following terms:
Attribution — You must give appropriate credit, provide a link to the license, and indicate if changes were made. You may do so in any reasonable manner, but not in any way that suggests the licensor endorses you or your use.
No additional restrictions — You may not apply legal terms or technological measures that legally restrict others from doing anything the license permits.
Notices:
You do not have to comply with the license for elements of the material in the public domain or where your use is permitted by an applicable exception or limitation.
No warranties are given. The license may not give you all of the permissions necessary for your intended use. For example, other rights such as publicity, privacy, or moral rights may limit how you use the material.